INELASTIC AND STIMULATED SCATTERING OF LIGHT

FROM MOBILE CARRIERS IN SEMICONDUCTORS

by

Ying Chi Sunny Auyang

B. S., University of California, Los Angeles
(1967)

SUBMITTED IN PARTIAL FULFILLMENT OF THE

REQUIREMENTS FOR THE DEGREE OF

DOCTOR OF PHILOSOPHY

at the

MASSACHUSETTS INSTITUTE OF TECHNOLOGY

December, 1971 (i.e. Feb, 1972)

Signature of Author _____
        Department of Physics, December 23, 1971

Certified by _____
        Thesis Supervisors

Accepted by _____
        Chairman, Departmental Committee on Graduate Students

INELASTIC AND STIMULATED SCATTERING OF LIGHT

FROM MOBILE CARRIERS IN SEMICONDUCTORS

by

Ying Chi Sunny Auyang

Submitted to the Department of Physics on December 23, 1971, in partial fulfillment of the requirements for the Degree of Doctor of Philosophy.

ABSTRACT

A first principle description of the spontaneous spin-flip scattering lineshape is developed. A general formula for the lineshape is obtained including two important broadening mechanisms, namely the nonparabolicity of the energy bands and the diffusion of electrons. When the scattered light travels perpendicular to the magnetic field, nonparabolicity dominates and a relatively simple expression is obtained for the lineshape in this limit. When the scattered light travels in the direction of magnetic field, electron diffusion along the magnetic field becomes dominant. The lineshape is then a simple Lorentzian. Analytic expressions for the spontaneous linewidth including its dependence on various parameters are obtained. These results are compared with available experimental data with good agreement except for the nonparabolicity dominated lineshape, though its linewidth is also in good agreement with experiments. These linewidths are then used in the Raman laser theory for detailed investigation of the stimulated scattering behaviors.

A detailed theory of traveling wave electronic Raman lasers is constructed, which applies in particular to the spin-flip Raman lasers of Patel and others. Ten equations are set up describing the behavior of the input laser field, the Stokes field, the anti-Stokes field and the electronic system explicitly. Solutions of these equations are obtained in the sinusoidal steady state limit. Depletion of the input laser field is accounted for in an approximated but novel fashion, in the form of photon number conservation. We are able to express the steady state output power in terms of the system parameters and the input boundary excitation alone. Analytic formulas are given for the linear gain, the threshold pump power, the Stokes and the anti-Stokes power output. They describe among other things the saturation and fluorescence behavior of the electronic Raman laser. Various intuitive interpretations are provided for the analytic results. The detailed predictions are in very good agreement with experiments.

A new mechanism for generating tunable high power coherent radiation in the wavelength range $10\,\mu$ - $35\,\mu$ from a single laser system is proposed. The proposed device is based on stimulated light scattering continuously tuned by stress in p-type semiconductors. The conditions and feasibility for such Raman laser operation are discussed in detail.

CO-THESIS SUPERVISORS: Benjamin Lax,
Professor of Physics, Director of National Magnet Laboratory

Peter A. Wolff,
Professor of Physics, Director of Atomic and Solid States Physics Division

<u>ACKNOWLEDGEMENTS</u>

TABLE OF CONTENTS

A NOTE ON NOTATIONS

The four chapters of this thesis are quite independent, each with its own sets of notations, equation numbers and references. Except otherwise specified, notations and symbols are defined within each chapter.

INTRODUCTION

Development of tunable lasers is of great interest in both science and technology. For example, the use of tunable infrared lasers in spectroscopy has led to orders of magnitude improvement in attainable resolution. [1],[2] They also provide the necessary local oscillators in some optical communication systems. Air pollution detection [3] is another example of their technological applications.

A most important tunable infrared laser, the spin-flip Raman laser [4] based on inelastic scattering of light from electronic spin-sublevels in n-type semiconductors, [5] has recently become available. Much work has now been reported on this laser and its applications since the first demonstration of laser action by Patel and Shaw [6] less than two years ago. The spin-flip Raman laser is interesting in many ways. It constitutes the first CW operation of a Raman laser, and provides high power tunable infrared radiations. Its gain of 1×10^{-5} cm^{-1}/W-cm^{-2} is the largest Raman gain known to date in any portion of the spectrum. It can have very high conversion efficiency and very low threshold power. Its tuning range is further extended by observations of anti-Stokes and second-Stokes stimulated scattering.

This spin-flip laser is, qualitatively, rather well-understood. [4] However, the quantitative and detailed behavior has yet to be explained and pre-

dicted. Many features of experimental observations,like the spontaneous and stimulated lineshapes, dependence of threshold on carrier concentration, magnetic field, temperature, experimental geonetry and crystal size, as well as stimulated output power characteristics have yet not received a rigorous and accurate description. It is our purpose in this thesis to establish a general framework and a complete theory to describe such detailed features. Our theory should be able to correlate, explain, and predict the empirical results from first principles, and to suggest optimal and feasibility conditions for laser operations under different environments and parameter values. We have also not restricted ourselves exclusively to spin-flip scattering in n-type semiconductors, so that our theory can be used to exploit other useful electronic Raman processes for possible tunable laser operations. An example of such an application to stress-tuned stimulated inter-valence band scattering in p-type semiconductors will be given.

In the following section I we give a brief literature review of stimulated electronic light scattering from semiconductors. We will then further discuss the nature of our work and give a preview of our four chapters in section II.

I. LITERATURE REVIEW

In 1966, Wolff [7] predicted the possibility of observing Landau Raman scattering in n-InSb from the nonparabolicity of the conduction band. Yafet [8] extended this work by considering a more detailed band model, and further

predicted the spin-flip scattering process. In 1967, Slusher, Patel and Fleury[5] reported the first experimental observation of spin-flip and Landau Raman scattering from conduction electrons in n-InSb. Subsequently, conduction electron spin-flip Raman scattering has been observed in InAs,[9] PbTe,[10] Cds,[11] and ZnSe.[11]

Wolff[12] has also discussed the possibility of a Raman laser tuned by magnetic fields, using stimulated Landau-Raman scattering. On the basis of the experimental results of Slusher, et.at,[5] it appears however that the spin-flip process is a better candidate for observation of stimulated scattering, because of its larger cross section and narrower linewidth. Stimulated spin-flip scattering in n-InSb was observed in early 1970 by Patel and Shaw,[6] and constitutes the first and only observation of stimulated scattering from electronic levels. A greal amount of experimental work on stimulated spin-flip scattering has since been reported, extending this Raman laser in various directions.[13]-[16] Some applications[1],[3] of this laser have already appeared and a lot of further work are in progress.

Concurrently with the development of spin-flip Raman laser, some theoretical work has been reported on the detailed understanding of this device. Markarov[17] and Wherrett and Harper[18] have considered the effects of electron statistics on the spin-flip cross section. Their results are however limited to the lowest Landau level. In Chapter 3 we will present results valid at arbitrary temperature, magnetic field, and carrier concentration. Breuck[19] has given a phenomenological description of the spontaneous spin-flip lineshape, using the transport theory of Davis and Blum.[20] An adjustable parameter is

introduced to fit the experimental data. In Chapter 1 we will make an absolute first principle calculation of the lineshape without adjustable parameters. Description of the spin-flip laser behavior is so far restricted to the application of threshold formula from Shen and Bloembergen, [21] partly because there is no detailed theory of the power behavior in the literature. In chapter 2 we develop a general theory of an electronic Raman laser to describe stimulated spin-flip scattering, among other processes. Our detailed predictions describe the steady state laser behavior completely. All our calculations are in good agreement with experiments.

We have also calculated the cross section for stress-tuned inter-valence band spin-flip scattering. In Chapter 4 we apply our general theory in a detailed consideration for obtaining stimulated inter-valence band scattering. It appears promising that a Raman laser stress-tuned in the wavelength range 10μ - 35μ can be obtained using p-InSb.

II. SUMMARY

The general purpose of our work is to establish from first principle a theoretical framework for detailed investigation of stimulated electronic Raman processes, in particular spin-flip scattering from n-InSb. Some approximations are required, as usual, to obtain concrete results. Thus we have set up ten equations of motion for a homogeneously broadened traveling wave electronic Raman laser to describe the inhomogeneously broadened spin-flip n-InSb laser, through an investigation of the spontaneous lineshape. The detailed justification

of this procedure in the case of n-InSb is given in Chapter 3. except for the more delicate feature of a Lamb dip, our theory provides an accurate description of the spin-flip laser behavior.

Our theory of spontaneous spin-flip lineshape, in contrast to previous work, is a first principle calculation. It provides us with analytic expressions for the spontaneous linewidth including its dependence on various parameters. These linewidths are then used in the laser theory for detailed investigations of the stimulated output. We have also noted two important mechanisms for the spontaneous line broadening. Diffusion of the electrons can be important and dominant in addition to nonparabolicity of the electronic energy bands.

Our investigation of electronic Raman laser behavior is confined to the steady state, where we give a rather complete discussion including anti-Stokes and pump radiations. The steady state power output behavior is theoretically derived for the first time. A proper treatment of pump depletion is also given.

Our theory is applied to the n-InSb case where we compare our absolute calculations with no adjustable parameters to experimental observations. Effects of electron statistics is included to obtain the dependence of the scattering behavior on various parameters. Because of the vast amount of experimental data available, we have not attempted a comprehensive comparison with all the data and restrict ourselves to only a subset of these data. In general all of our calculations are in good agreement with experiments.

Applying our theory to light scattering continuously tuned by stress in p-type semiconductors, we have derived the conditions for tunable Raman laser operations. Feasibility of obtaining a high power laser tunable in the wave-length range 10μ - 35μ is established using p-InSb. We therefore propose a new device based on such an effect. No experimental work has, however, been performed or attempted.

In the following Chapter 1 we develop a first principle description of the spontaneous spin-flip lineshape. A general formula for the lineshape is obtained including both diffusion and nonparabolicity contributions. When the scattered light travels perpendicular to the magnetic field, nonparabolicity dominates and a relatively simple expression is obtained for the lineshape in this limit. When the scattered light travels in the direction of the magnetic field, electron diffusion along the magnetic field becomes dominant. The lineshape is then a simple Lorentzian. These results are compared with available experimental data with good agreement except for the nonparabolicity dominated lineshape, though its linewidth is also in good agreement with experiment.

In Chapter 2 we develop a detailed theory of traveling wave electronic Raman lasers. Ten equations are set up describing the behavior of the input laser field, the Stokes field, the anti-Stokes field, and the electronic system explicitly. Solution of these equations are obtained in the steady state limit. Depletion of the pump field is accounted for in an approximate but novel fashion, in the form of photon number conservation. We are able to express the steady state output power in terms of the system parameters and the boundary excitation alone. Analytic formulas are given for the linear gain,

the threshold pump power, and the Stokes as well as the anti-Stokes power outputs. They describe among other things the saturation and fluorescence behavior of the electronic Raman laser. Our detailed predictions are in very good agreement with experiments, and probably constitutes the first detailed confirmation between Raman laser theory and experimental observations.

In Chapter 3 we apply our theory in the previous chapters to the magnetic field-tuned n-InSb laser. Justification for applying our homogeneously broadened theory to this actually inhomogeneous case is given. Effects of Fermi statistics on the laser behavior are treated in detail, which manifest in its magnetic field, carrier concentration, and temperature dependence. An explicit formula is given for the effective cross section as a function of the system parameters. The effect of crystal size on threshold pump power is investigated. Our calculations are compared with experimental observations with very good agreement.

In Chapter 4 we employ our theory in exploiting the feasibility of obtaining stress-tuned stimulated spin-flip scattering from p-type semiconductors. Cross sections and linewidths are calculated for such a process and the electronic Raman laser theory is used to investigate the stimulated behavior. We conclude that with p-InSb, it may be possible to obtain stimulated light scattering from intervalence band spin-flip transitions. In such a situation we will have a easily tunable high power laser source in the wavelength range 10μ - 35μ . Further extension into the far infrared appears to be limited only by phonon absorption in the crystal.

REFERENCES

(1)   C. K. N. Patel, E. D. Shaw, and R. J. Kerl, Phys. Rev. Letters 25, 8 (1970)

(2)   E. D. Hinkley, Appl. Phys. Letters 16, 351 (1970)

(3)   L. B. Kreuzer and C. K. N. Patel, Science 173, 45 (1971)

(4)   C. K. N. Patel and E. D. Shaw, Phys. Rev. B 3, 1279 (1971)

(5)   R. E. Slusher, C. K. N. Patel and P. A. Fleury, Phys. Rev. Letters, 18, 530 (1967);   see also, C. K. N. Patel in Modern Optics, Vol. XVII, (Polytechnic Press, New York, 1967)

(6)   C. K. N. Patel and E. D. Shaw, Phys. Rev. Letters 24, 451 (1970)

(7)   P. A. Wolff, Phys. Rev. Letters 16, 225 (1966)

(8)   Y. Yafet, Phys. Rev. 152, 858 (1966)

(9)   C. K. N. Patel and R. E. Slusher, Phys. Rev. 167, 413 (1968)

(10)   C. K. N. Patel and R. E. Slusher, Phys. Rev. 177, 1200 (1969)

(11)   P. A. Fleury and J. F. Scott, Phys. Rev. B 3, 1979 (1971)

(12)   P. A. Wolff, J. Quantum Electronics 2, 659 (1966)

(13)   R. L. Allwood, S. D. Devine, R. G. Mellish, S. D. Smith, and R. A. Wood, J. Phys. C, Solid State Physics 3, L186 (1970); R. L. Allwood, R. B. Dennis, S. D. Smith, B. S. Wherrett, and R. A. Wood, J. Phys. C. Solid State Physics 4, L163 (1971); R. L. Allwood, R. B. Dennis, R. G. Mellish, S. D. Smith, B. S. Wherett, and R. A. Wood, J. Phys. C. Solid State Phys. 4, L136 (1971)

(14)   A. Mooradian, S. R. J. Brueck and F. A. Blum, Appl. Phys. Letters 17, 481 (1970); S. R. J. Brueck and A. Mooradian, Appl. Phys. Letters 18, 229 (1971); F. A. Blum and A. Mooradian in Proceedings of Tenth

International Conference on the Physics of Semiconductors, Ed. by S. P. Keller, J. C. Hensel, and F. Stern (U. S. AEC, Tenn, 1970)

(15)   R. L. Aggarwal, B. Lax, C. E. Chase, C. R. Pidgeon, D. Limbert, and F. Brown, Appl. Phys. Letters 18, 383 (1971); R. L. Aggarwal, B. Lax, C. R. Pidgeon, and D. Limbert, Int. Conf. ong Light Scatt. Spectra. of Solids, Paris, 1971.

(16)   C. K. N. Patel in _Proceedings of Tenth Int. Conf. on the Phys. of Semiconductors_, Ed. by S. P. Keller, J. C. Hensel, and F. Stern (U. S. AEC, Tenn., 1970)

(17)   V. P. Makharov, Soviet Phys. JETP 28, 336 (1969)

(18)   B. S. Wherett and P. G. Harper, Phys. Rev. 183, 692 (1969)

(19)   S. R. J. Breuck, Ph.D. thesis, submitted to M.I.T., Cambridge, 1971.

(20)   R. W. Davies and F. A. Blum, Phys. Rev. B 3, 3321 (1971)

(21)   Y. R. Shen and N. Bloembergen, Phys. Rev. 137, A1787 (1965)

CHAPTER 1

THEORY OF SPONTANEOUS SPIN FLIP RAMAN SCATTERING LINESHAPE

I. INTRODUCTION

In a magnetic field the electron energy is quantized into Landau levels with energies

$$ n \hbar \omega_c + \frac{\hbar^2}{2m^*} k_3^2 \tag{I.1} $$

where ω_c is the cyclotron frequency, m^* the effective mass, k_3 the electron momentum along the magnetic field, and n denotes the nth Landau level. The 1/2 term is omitted because we choose to measure all energies from the bottom of the zeroth Landau level. Spin-orbit coupling again splits each Landau level into two sublevels separated by

$$ |\hbar \omega_s| = \mu_B |g| B \tag{I.2} $$

with μ_B the Bohr magneton and g the effective g-value. We will consider the spin flip Raman (SFR) process in which an electron in one spin sublevel is scattered by an incident pump photon with energy ω_p to the other of the same Landau level, leaving a scattered photon with energy

$$ \hbar \omega_f = \hbar \omega_p - \mu_B |g| B . \tag{I.3} $$

In the following, scattering from conduction electrons in InSb will be considered in particular.

The light scattering processes are shown in Figure 1.1. The magnetic field is along the $\hat{z}$ direction. The incident field with wavevector $\vec{k}_p$ and polarization $\hat{\epsilon}_p$ propagates along the $\hat{y}$ direction. The scattered radiation, specified by $(\omega_f, \vec{k}_f, \hat{\epsilon}_f)$, can be collected in several directions: (1) with $\vec{k}_f$ normal to the magnetic field as shown in Figure 1.1a. This we shall refer to as the $\vec{q}\cdot\vec{B}=0$ geometry [1], where $\vec{q} = \vec{k}_p - \vec{k}_f$ is the momentum transfer; or (2) with $\vec{k}_f$ parallel to $\vec{B}$ as in Figure 1.1b. This is the $\vec{q}\cdot\vec{B}\neq0$ geometry. There are, of course, many other possible geometries, for example with the $\vec{k}_f$ making a certain angle with $\vec{B}$. We will however not discuss these other cases here.

The simplest consideration of lineshapes is via a phenomenoligical collision model characterized by a collision time τ. The spectrum is then a Lorentzian with a constant full width $2/\tau$. In the spin flip process we are considering, there are two distinct lifetimes involved. The first is a spin lifetime τ_s which characterizes those processes involving the relaxation of a spin excitation. The second, which we shall call the orbital lifetime τ_p, is caused by collisions within the same spin sublevel. These orbital collision, which do not connect the two spin sublevels, do not contribute to our scattering linewidth since the width of the spectral line is the difference in widths of the two spin sublevels, [2] and the orbital collision rates for the two sublevels are the same. Thus the spectrum will be characterized by τ_s. A phenomenological calculation of the lineshape by using these two collision times is carried out by Brueck. [1]

Yafet[3] has calculated the rate of spin relaxation via acoustic phonons in a magnetic field. For InSb with carrier concentration $N=10^{16}$ cm^{-3}, his expression yields a lifetime $\tau_s \simeq 10^{-8}$ sec. Extrapolations of experimental spin-resonance data in InSb[4] yields a collision time $\tau_s \simeq 10^{-9} - 10^{-10}$ sec. From all evidence, 10^{-10} sec^{-1} seem to be a upper bound for the spin relaxation rate. It can readily be seen that this rate is too small to explain the observed spin-flip Raman scattering linewidth, which is of the order of $1cm^{-1}$.[1][5] Other broadening mechanisms must then be taken into account.

In materials such as InSb, nonparabolicity of the conduction band will make an important contribution to the spontaneous SFR linewidth. In fact in some cases, as in the $\vec{q}.\vec{B}=0$ geometry, the linewidth will be determined primarily by the band nonparabolicity. Since the effective g-value is now a function of energy, the scattered energy will be different for transitions at the band edge and at finite k_3 as shown in Figure 1.2, hence a spread in the resulting spectrum.

Another important contribution is the diffusion of electrons between each collision. This effect is more important in the $\vec{q}.\vec{B}\neq0$ geometry where the electron diffusion along the magnetic field is observed. We will discuss in more details these two broadening mechanisms and their relative importance in this chapter.

In section II a general formulation of the differential cross section is given. The generalized spin correlation function is calculated for the case in

nonparabolicity effect is dominant in section III. Diffusion effects are consi-
dered in section IV and the results compared with experiment in section V.
Section VI discusses the other possible broadening mechanisms that are not
taken into account in the calculation, and their respective contributions to
the lineshape. Discrepencies between theory and experiment are also dealt
upon.

The following calculations are particularly formulated for a system in
the extreme strong magnetic field limit (quantum limit), where in thermal
equilibrium all electrons are in the lowest Landau level. They can however
be readily generalized to cases in which more than one Landau levels are
occupied, as in the spin-flip scattering from n-CdS.[6] In Chapter 4 the
theory developed here will be generalized to situations without the presence
of magnetic field.

II. FORMULATION

Consider a many electron system under a constant magnetic field
with hamiltonian

$$H_T = H_0 + V + \tfrac{1}{2}\mu_B g_{eff}\, \vec{B}\cdot\vec{\sigma} \qquad (II.1)$$

where

$$H_0 = \sum_i \frac{1}{2m}\left\{ \vec{\pi}_i - \frac{e\vec{A}}{c} \right\}^2 + V_c(\vec{r}) \qquad (II.2)$$

is the sum of one-electron hamiltonians, plus the periodic crystal potential $V_c(\vec{r})$, and V accounts for electronic collisions with impurities, optical and acoustic phonons. Here

$$\vec{\pi}_i = \vec{P}_i + \hbar \frac{\vec{\sigma} \times \vec{\nabla} V_c(\vec{r})}{4mc^2} \quad ,$$

and σ's are the Pauli spin operators, $\vec{A}$ is the vector potential associated with $\vec{B}$ and g_{eff} is the effective g-value which can depend on energy. To first order in energy

$$g_{eff} = g_0 (1 + \lambda H_0) \qquad\qquad (II.3)$$

where g_0 is the g-value at the band edge and λ is a parameter measuring the band nonparabolicity. For n-InSb, a two band model [7] calculation gives $\lambda = -2/E_g$, E_g being the energy gap. Note that only H_0 , rather than $(H_0 + V)$, appears in (II.3). Also, we have neglected the Coulomb interactions in (II.1), their consequence will be discussed in section VI.

The interaction of this electron system with an incident electromagnetic wave with vector potential $\vec{A}_\omega$ can be expressed by replacing $\vec{p}$ in (II.1) by $(\vec{p} - e\vec{A}_\omega/c)$. Treating $\vec{A}_\omega$ as a perturbation, the transition probability for the scattering of a photon from state $(\omega_p, \vec{k}_p, \hat{\epsilon}_p)$ to state $(\omega_f, \vec{k}_f, \hat{\epsilon}_f)$ with the accompanying transition of the many electron system from state $|I\rangle$ to $|F\rangle$ is given by the matrix elements of the operators $\vec{A}_\omega^2$ and $\vec{\pi} \cdot \vec{A}_\omega$. The general expression for the differential cross section is then given in the Born Approximation by

$$\frac{d\sigma}{d\omega\, d\Omega} = \left(\frac{e^2}{mc^2}\right)^2 \frac{\omega_f}{\omega_p} \left\langle \sum_F |M_{FI}|^2 \, \delta(E_F - E_I - \hbar\omega) \right\rangle_s$$

(II.4)

where $\langle \cdots \rangle_s$ denotes the average over initial states and $\omega = \omega_p - \omega_f$. The matrix element M_{FI} is given by [8]

$$M_{FI} = \hat{\epsilon}_I \cdot \hat{\epsilon}_F \sum_{\alpha\alpha'} \langle F|a_\alpha^\dagger a_{\alpha'}|I\rangle \langle\alpha| e^{i\vec{q}\cdot\vec{r}} |\alpha'\rangle$$

(II.5)

$$+ \frac{1}{m} \sum_N \sum_{\substack{\alpha\alpha' \\ \beta\beta'}} \langle\alpha|\vec{j}_p|\alpha'\rangle\langle\beta|\vec{j}_f|\beta'\rangle$$

$$\times \left\{ \frac{\langle F|a_\alpha^\dagger a_{\alpha'}|N\rangle\langle N|a_\beta^\dagger a_{\beta'}|I\rangle}{E_I - E_N + \hbar\omega_p} + \frac{\langle F|a_\beta^\dagger a_{\beta'}|N\rangle\langle N|a_\alpha^\dagger a_{\alpha'}|I\rangle}{E_I - E_N - \hbar\omega_f} \right\},$$

$$\vec{j}_{\substack{p \\ f}} = \hat{\epsilon}_{\substack{p \\ f}} \cdot \left(\vec{\pi} - \frac{e\vec{A}}{c}\right) e^{i\binom{\vec{k}_p}{-\vec{k}_f}\cdot\vec{r}}$$

(II.6)

In deriving (II.5), $\vec{j}_p$, $\vec{j}_f$ are second quantized in eigenstates of $(H_T - V)$, $|\alpha\rangle$, $|\beta\rangle$ with creation operators $a_\alpha^\dagger$, $a_\beta^\dagger$ respectively. Here we use the index α to denote the set of quantum numbers (n, k_y, k_z, s) , s being the spin index. The first term in (II.5) comes from the term A^2 treated to first order, while the second part is derived from the $\vec{\pi}\cdot\vec{A}\omega$ term to second order.

Neglecting the interaction between electrons, we can assume that the intermediate many electron state $|N\rangle$ differs from the initial and final states only by a single electron excitation. Under this approximation, the spectrum (II.4) can be expressed as the Fourier transform of a generalized spin correlation function [8],[9]

$$\frac{d^2\sigma}{d\omega \, d\Omega} = \left(\frac{e^2}{mc^2}\right)^2 \frac{\omega_f}{\omega_p} \int_{-\infty}^{\infty} \frac{dt}{2} \, e^{i\omega t} \langle \underline{N}^+(t) \, \underline{N}(0) \rangle$$

(II.7)

where

$$\underline{N}^+(t) = e^{iH_T t/\hbar} \, \underline{N}^+ \, e^{-iH_T t/\hbar}$$

(II.8)

$$\underline{N}^+ = \sum_{\alpha\beta} \gamma_{\alpha\beta} \, a_\alpha^+ a_\beta$$

(II.9)

and

$$\gamma_{\alpha\beta} = \langle \alpha | e^{i\vec{q}\cdot\vec{r}} | \beta \rangle \, \hat{\epsilon}_p \cdot \hat{\epsilon}_f$$

$$+ \frac{1}{m} \sum_{\beta'} \left\{ \frac{\langle \alpha | \vec{j}_f | \beta' \rangle \langle \beta' | \vec{j}_p | \beta \rangle}{E_\beta - E_{\beta'} + \hbar\omega_p} + \frac{\langle \alpha | \vec{j}_p | \beta' \rangle \langle \beta' | \vec{j}_f | \beta \rangle}{E_\alpha - E_{\beta'} - \hbar\omega_f} \right\} .$$

(II.10)

From now on we will concentrate our attention on InSb which has a negative effective g-value, so that (II.1) becomes

$$H_T = H - \frac{\omega_s}{2} \hbar \, \sigma_z \, (1 - |\lambda| \, H_0)$$

(II.11)

$$H = H_0 + V .$$

Consider now an electron with momentum k_z in the spin up state of the nth Landau level is scattered to the spin down state of the same Landau level with a momentum shift $\vec{q}$. Writing the quantum numbers explicitly, (II.9)

becomes

$$\underline{N} = \sum_{n k_y k_z} \gamma_{\downarrow\uparrow} (n, k_z, q)\, a^{\dagger}_{n k_y + q_y, k_z + q_z} a_{n k_y k_z \uparrow} \,. \tag{II.12}$$

Note that in (II.12) the $a's$ are the Fermi-Dirac operators acting on many electron states. $\underline{N}$ can be expressed as the sum of single particle operators

$$\underline{N} = \sum_{i} N_i \,. \tag{II.13}$$

With (II.13), equation (II.7) can then be reduced from a many electron expression to a one-electron expression in which the operators of second quantization disappear [10]

$$\frac{d^2\sigma}{d\omega d\Omega} = \left(\frac{e^2}{mc^2}\right)^2 \frac{\omega_f}{\omega_p} \frac{1}{2} \int_{-\infty}^{\infty} dt\, e^{i\omega t}\, \text{tr}\left\{ f(H_T) N^{\dagger}(t)\left[1 - f(H_T)\right] N(0) \right\} \tag{II.14}$$

where $f(H_T)$ is the Fermi-Dirac distribution function, and the $N's$ are just the $N_i's$ in (II.13) with subscript i supressed. The reduction from (II.7) to (II.14) is carried out in detail in Appendix 1B.

Now we shall assume that $\gamma_o \triangleq \gamma_{\downarrow\uparrow} (n k_z q)$ is a constant independent of the quantum numbers. This approximation holds only if $\hbar\omega_p$ is not close to E_q [11], as in case of a CO_2 laser scattering from InSb. In cases where the resonance enhancement [12] is strong, as InSb is scattered by a CO laser, [1] $\gamma_{\downarrow\uparrow} (n k_z q)$ will be a strong function of k_z. With γ_o a constant, $\underline{N}$ can be expressed as the product of a spin operator and a density fluctuation,

$$\underline{N} = \gamma_o \sum_{nk_y k_3} a^+_{nk_y+q_y, k_3+q_3 \downarrow} a_{nk_y k_3 \uparrow} \triangleq \gamma_o \sigma_- \rho_{-\vec{q}}$$

$$\underline{N}^+ = \gamma_o^* \sum_{nk_y k_3} a^+_{nk_y k_3 \uparrow} a_{nk_y+q_y, k_3+q_3 \downarrow} \triangleq \gamma_o^* \sigma_+ \rho_{\vec{q}}$$

(II.15)

where σ_+ , σ_- are Pauli spin operators [13]

$$\sigma_z = 2\sigma_+ \sigma_- - 1$$

with commutators

$$[\sigma_+, \sigma_-] = \sigma_z$$

$$[\sigma_\pm, \sigma_z] = \mp 2\sigma_\pm$$

(II.16)

$$[\sigma_+, \sigma_+] = [\sigma_-, \sigma_-] = 0 .$$

The ρ 's in (II.15) are the electron density fluctuations

$$\rho_{\vec{q}} = \sum a^+_{nk_y k_3} a_{nk_y+q_y, k_3+q_3}$$

$$= \int d\vec{r} \, e^{-i\vec{q}\cdot\vec{r}} \rho(\vec{r})$$

$$= \sum_i e^{-i\vec{q}\cdot\vec{r}_i}$$

$$\triangleq \sum_i \tilde{\rho}_{\vec{q}} ,$$

(II.17)

$$\rho_{-\vec{q}} = \rho_{\vec{q}}^+ .$$

(II.18)

$\tilde{\rho}_{\vec{q}}$ evolves in time as

$$\tilde{\rho}_{\vec{q}}(t) = e^{iHt/\hbar} \tilde{\rho}_{\vec{q}}(0) e^{-iHt/\hbar} .$$

(II.19)

In analogous to N discussed before, $\tilde{\rho}_{\vec{q}}$ stands for the single particle density fluctuation.

Substituting (II.15) and (II.7) into (II.14) yields

$$\frac{d^2\sigma}{d\omega\,d\Omega} = \left(\frac{e^2}{mc^2}\right)^2 \frac{\omega_f}{\omega_p} \frac{|\gamma_0|^2}{2} \int_{-\infty}^{\infty} dt \, e^{i\omega t} \, \mathrm{tr}\left\{ f\left[H - \frac{\hbar\omega_s}{2}(1-\lambda H_0)\sigma_z\right]\right.$$

$$\times \, e^{i\left[H - \frac{\hbar\omega_s}{2}\sigma_z(1-\lambda H_0)\right]t/\hbar} \; \sigma_+ \tilde{\rho}_{\vec{q}} \; e^{-i\left[H-\frac{\hbar\omega_s}{2}\sigma_z(1-\lambda H_0)\right]t/\hbar} \tag{II.20}$$

$$\times \left. \left[1 - f\left(H - \frac{\hbar\omega_s}{2}\sigma_z(1-\lambda H_0)\right)\right] \sigma_- \tilde{\rho}_{\vec{q}} \right\} .$$

For simplicity, we shall only consider here those scattering potentials V that do not flip spin, i.e.,

$$[V, \sigma_{\pm}] = [V, \sigma_z] = 0. \tag{II.21}$$

The effects of this, and those potentials that do flip spin are discussed in section I, from where we saw that (II.21) is a reasonable approximation since the spin collision time , τ_s , is long compared to the orbital collision time, $\tau_s \cong 10^{-8}$ seconds. Making use of the operator relation [13]

$$f(\sigma_+\sigma_-) = f(0) + [f(1) - f(0)]\,\sigma_+\sigma_- , \tag{II.22}$$

together with (II.16), we can extract all spin operators from (II.20) to give

$$\frac{d^2\sigma}{d\omega\,d\Omega} = \left(\frac{e^2}{mc^2}\right)^2 \frac{\omega_f}{\omega_p} \frac{|\gamma_0|^2}{2} \int_{-\infty}^{\infty} dt \, e^{i\omega t} \, \mathrm{tr}\left\{ f\left[H - \frac{\hbar\omega_s}{2}(1-\lambda(H-V))\right]\right.$$

$$\times \, e^{i\{H - \frac{\hbar\omega_s}{2}[1-\lambda(H-V)]\}t/\hbar} \; \tilde{\rho}_{\vec{q}} \; e^{i\{H + \frac{\hbar\omega_s}{2}[1-\lambda(H-V)]\}t/\hbar} \tag{II.23}$$

$$\times \left. \left[1 - f\left(H + \frac{\hbar\omega_s}{2}(1-\lambda(H-V))\right)\right] \tilde{\rho}_{\vec{q}} \; \sigma_+\sigma_- \right\} .$$

We see that in (II.23), both $\lambda\omega_s$ and V are small compared to H_o. We will make the approximation of neglecting in (II.23) the terms $\lambda\omega_s V$ which is to second order in smallness. In Appendix 1C a treatment without making this approximation is given. Thus, with (II.19), equation (II.23) can be written as

$$\frac{d^3\sigma}{d\omega d\Omega} = \left(\frac{e^2}{mc^2}\right)^2 \frac{\omega_f}{\omega_p} \frac{|Y_o|^2}{2} \int_{-\infty}^{\infty} dt\, e^{i\omega t}\, \mathrm{tr}\left\{ f[H- \tfrac{\hbar\omega_s}{2}(1-\lambda H)] e^{-i\hbar\omega_s(1-\lambda H)t/2\hbar} \right.$$

$$\times e^{-i\vec{q}\cdot\vec{r}(t)} e^{i\hbar\omega_s(1-\lambda H)t/2\hbar} [1-f(H+ \tfrac{\hbar\omega_s}{2}(1-\lambda H))] e^{i\vec{q}\cdot\vec{r}(0)} \sigma_+\sigma_- \left. \right\}. \qquad (II.24)$$

Now we examine the commutation relations of $\tilde{\rho}_{\vec{q}}$. It can be shown easily that

$$[V, \tilde{\rho}_{-\vec{q}}] = [V, \tilde{\rho}_{\vec{q}}] = 0, \qquad (II.25)$$

which is a consequence of the approximation of setting Y_o as a constant. As will be shown later, the electron diffusion rate across the magnetic field is much slower than the electron diffusion rate along $\vec{B}$, so that we can say that

$$q_x \delta x(t) + q_y \delta y(t) \ll 1, \qquad (II.26)$$

where

$$\vec{r}(t) = \vec{r}(0) + \delta\vec{r}(t).$$

In view of (II.26), and with equation (II.25), we then have

$$[H, \tilde{\rho}_{-\vec{q}}(t)] \cong \tilde{\rho}_{-\vec{q}} F(H_o)$$

$$[H, \tilde{\rho}_{\vec{q}}(t)] \cong - F(H_o) \tilde{\rho}_{\vec{q}}, \qquad (II.27)$$

where

$$F(H_0) = \frac{\hbar^2}{2m^*}\left\{ q_\delta^2 + 2q_\delta\sqrt{\frac{2m^* H_0}{\hbar^2}} \right\}. \tag{II.27a}$$

$F(H_0)$ is just the difference in energy due to momentum shift $\vec{q}_\delta$ as shown in Figure 1.2b. With (II.25) and (II.27) it can readily be proved by expanding the exponential in an infinite sum series that

$$\tilde{\rho}_{\vec{q}}(t)\, e^{i(H_0 + V)} = e^{i[H_0 + V + F(H_0)]}\, \tilde{\rho}_{\vec{q}}(t). \tag{II.28a}$$

Further, for any smooth function f, by writting f as a Fourier integral in terms of resolution of exponentials, we can obtain by using (II.28a)

$$\tilde{\rho}_{\vec{q}}(t)\, f(H_0 + V) = f[H_0 + V + F(H_0)]\, \tilde{\rho}_{\vec{q}}(t). \tag{II.28b}$$

We will make another approximation by replacing $F(H_0)$ in (II.27) by $F(H)$ which is in effect neglecting a term

$$F(H_0 + V) - F(H) \simeq \frac{1}{2} V \sqrt{\frac{\hbar^2 q_\delta^2}{2m^*}}\, \frac{1}{\sqrt{H_0}}. \tag{II.29}$$

Since $\hbar^2 q_\delta^2 / 2m^*$ is also small compared with H_0, this step is consistent with the approximation made before. Under these approximations with equations (II.25) (II.27) and (II.28), equation (II.24) becomes

$$\frac{d^2\sigma}{d\omega d\Omega} = \left(\frac{e^2}{mc^2}\right)^2 \frac{\omega_f}{\omega_p} \frac{|\gamma_0|^2}{2} \int_{-\infty}^{\infty} dt\, e^{i\omega t}\, \mathrm{tr}\left\{ f[H - \frac{\hbar\omega_s}{2}(1-\lambda H)] \right.$$
$$\times\, e^{-i\omega_s[1-\lambda H - \lambda F(H)]/\hbar\, t}\left[1 - f(H + \frac{\hbar\omega_s}{2}(1-\lambda H) + (1 - \frac{\lambda\omega_s}{2})F(H)) \right]$$
$$\times\, \tilde{\rho}_{\vec{q}}(t)\, \tilde{\rho}_{-\vec{q}}(0)\, \sigma_+ \sigma_- \left. \right\}, \tag{II.30}$$

which, by using the spatial invariance property of the particle density $\tilde{\rho}(\vec{r}, t)$, can be reduced to

$$\frac{d\sigma}{d\omega d\Omega} = \left(\frac{e^2}{mc^2}\right)^2 \frac{\omega_f}{\omega_p^2} \frac{|\gamma_0|^2}{2} \int_0^\infty d\varepsilon \, f\left[\varepsilon - \frac{\hbar\omega_s}{2}(1-\lambda\varepsilon)\right]$$

$$\times \left\{ 1 - f\left[\varepsilon + \frac{\hbar\omega_s}{2}(1-\lambda\varepsilon) + (1-\frac{1}{2}\lambda\hbar\omega_s)F(\varepsilon)\right]\right\}$$

$$\times \int_{-\infty}^\infty dt \, e^{i\omega t} \, e^{i[\omega-\omega_s(1-\lambda\varepsilon)-\frac{\lambda\omega_s}{2}F(\varepsilon)]t} \, \text{tr}\left\{\delta(\varepsilon-H) \int_{-\infty}^\infty e^{-i\vec{q}\cdot\vec{r}} d\vec{r} \, \tilde{\rho}(\vec{r},t)\tilde{\rho}(0,0)\right\}, \quad \text{(II.31)}$$

where the $\sigma_+\sigma_-$ in (II.30) has been traced away.

The quantity under trace in (II.31) can be written as

$$\text{tr}\left\{\delta(\varepsilon-H)\int_{-\infty}^\infty e^{-i\vec{q}\cdot\vec{r}} d\vec{r} \int_{-\infty}^\infty d\vec{r}' G(\vec{r},t|\vec{r}',0)\tilde{\rho}(\vec{r}',0)\tilde{\rho}(0,0) \, d\vec{r}'\right\} \quad \text{(II.32)}$$

where $G(\vec{r},t|\vec{r}',0)$ is the Green's function [14] and $\tilde{\rho}(\vec{r}',0)\tilde{\rho}(0,0)$ is the one-time density correlation function. In our approximation of neglecting the interaction between electrons [15]

$$\tilde{\rho}(\vec{r}',0)\,\tilde{\rho}(0,0) = \delta(\vec{r}'), \quad \text{(II.33)}$$

which says that the electron correlates only with itself. Here we are mainly concerned with electronic diffusion in a magnetic field. It is well known that the diffusion rate along the magnetic field is much greater than the diffusion rate across the field, which is approximately the former reduced by a factor $\left(1/\omega_c\tau\right)^2$. In our case this factor is at most 10^{-3} so that we will only consider the diffusion along z-direction. $G(z,t|z',0)$ can be obtained from the diffusion equation [14]

$$G(z,t|z',0) = \frac{1}{\sqrt{4\pi Dt}} \, e^{-(z-z')^2/4Dt}, \quad \text{(II.34)}$$

where D is the diffusion constant along the magnetic field.

Substituting (II.33) and (II.34) into (II.32) and integrating over ζ and ζ' , (II.32) becomes

$$e^{-q_z^2 D|t|} \; \text{Tr} \left\{ \delta(\mathcal{E}-H) \right\} . \tag{II.35}$$

The trace in (II.35) can be recognized at once to be the spin independent density of state including collision $\rho(\mathcal{E})$. Putting (II.35) into (II.31) and integrating over t yields our final result

$$\frac{d^2\sigma}{d\omega d\Omega} = \left(\frac{e^2}{mc^2}\right)^2 \frac{|\gamma_0|^2}{2} \frac{\omega_f}{\omega_p} \int_0^\infty d\mathcal{E} \; \rho(\mathcal{E}) \, f\left[\mathcal{E} - \frac{\hbar\omega_s}{2}(1-\lambda\mathcal{E})\right]$$

$$\times \left\{ 1 - f\left[\mathcal{E} + \frac{\hbar\omega_s}{2}(1-\lambda\mathcal{E}) + (1 - \frac{\lambda\hbar\omega_s}{2}) F(\mathcal{E})\right] \right\} \frac{2q_z^2 D}{\left[\omega_s(1-\lambda\mathcal{E}) - \omega - \frac{\omega_s}{2} F(\mathcal{E})\right]^2 + (q_z^2 D)^2} . \tag{II.36}$$

The spectrum in (II.36) reflects the collision broadened density of states, $\rho(\mathcal{E})$, convolved with a Lorentzian with full width $2q_z^2 D$ which is caused by diffusion of the electrons. The two Fermi functions takes care of statistics and temperature effects. In the following sections we shall make further approximations to obtain simple expressions for the lineshape for the two geometries discussed in section I.

III. NONPARABOLOCITY DOMINATED LINESHAPE

We now consider the limit in which diffusion effect is negligible. (II.36) can then be reduced to

$$\frac{d^2\sigma}{d\omega d\Omega} = \left(\frac{e^2}{mc^2}\right)^2 |\gamma_0|^2 \frac{\omega_f}{\omega_p^2} \pi \int_0^\infty \rho(\varepsilon) d\varepsilon \; f\left[\varepsilon - \frac{\hbar\omega_s}{2}(1-\lambda\varepsilon)\right]$$

$$\times \left\{ 1 - f\left[\varepsilon + \frac{\hbar\omega_s}{2}(1-\lambda\varepsilon) + (1-\frac{\hbar\lambda\omega_s}{2})F(\varepsilon)\right]\right\} \delta\left\{\omega - \omega_s(1-\lambda\varepsilon) - \frac{\omega_s}{2}F(\varepsilon)\right\}$$.

(III.1)

Equation (III.1) shows that the spectrum is just the density of state evaluated at the difference of energy between electronic initial and final states. This is no other than the "joint density of state" commonly used in magneto-optics.[16] The Fermi factors gives the statistic effects and must be included to give right dependences of the lineshape on magnetic field, carrier concentration, and temperature.

We now proceed to calculate the density of state

$$\rho(\varepsilon) = \; \mathrm{Tr}\, \delta(\varepsilon - H).$$

(III.2)

Without any collision effects, the density of states in a magnetic field is[10]

$$\rho(\varepsilon) = \left(\frac{2m^*}{\hbar^2}\right)^{1/2} \frac{1}{(2\pi l)^2} \sum_{n=0}^{n_{max}} \frac{1}{\sqrt{\varepsilon - n\hbar\omega_c}},$$

(III.3)

where $l = (\hbar c/eB)^{1/2}$ is the classical radius of the lowest Landau orbit. In the quantum limit we are considering, only one Landau level is occupied so that $n_{max} = 0$. This free magnetic density of states shows a

singularity at $\varepsilon = 0$, hence a zero linewidth. Collisions, however, will round off this singularity to give a finite linewidth. We will now calculate the collision broadened density of state (III.2), using the methods of Kubo.[10]

Introducing the resolvent operator for the hamiltonian $H \triangleq H_0 + V$

$$R(s) = \frac{1}{H - s} \qquad \text{(III.4)}$$

where s is a complex variable, the delta function can be expressed as[9],[10]

$$\delta(\varepsilon - H) = Im \lim_{\eta \to 0} \frac{1}{\pi} R(\varepsilon + i\eta). \qquad \text{(III.5)}$$

By making a damping theoretic expansion of the resolvent $R(s)$ and keeping only the diagonal parts, (III.4) becomes

$$R(s) \simeq \frac{1}{H_0 + G(s) - s} \qquad \text{(III.6)}$$

so that the density of states is

$$\rho(\varepsilon) = Im \lim_{\eta \to 0} \frac{1}{\pi} tr \left\{ \frac{1}{H_0 + G(\varepsilon + i\eta) - (\varepsilon + i\eta)} \right\} \qquad \text{(III.7)}$$

$$= Im \frac{1}{\pi} \frac{(V_0 \ell)}{(2\pi \ell)^2} \left(\frac{2m^*}{\hbar^2} \right)^{1/2} \frac{1}{\sqrt{G(\varepsilon) - \varepsilon}}$$

where the self energy, $G(s)$, is given approximately by

$$G(s) = -V \frac{1}{H_0 + G(s) - s} V \quad , \qquad \text{(III.8)}$$

and V_{ol} is the volume of the crystal. By taking matrix elements of (III.8) between states $|n k_y k_3\rangle$,

$$\langle G_{n k_y k_3}(S)\rangle_s \cong - \sum_{n' k_y' k_3'} \frac{\langle |\langle n k_y k_3|V|n' k_y' k_3'\rangle|^2\rangle_s}{n'\hbar\omega_c + \hbar^2 k_3'^2/2m^* + \langle G_{n' k_y' k_3'}(S)\rangle_s - S}$$
(III.9)

where $\langle \cdots \rangle_s$ denotes the average over scatterers. Note that (III.9) is derived in the effective mass approximation, which is in effect neglecting the nonparabolicity of the energy bands.

In Appendix 1D $\langle G_{n k_y k_3}(S)\rangle_s$ is calculated for elastic scattering of electrons by N_s impurity centers each with charge Ze via a screened Coulomb potential

$$V(\vec{r}) = \sum_{j=1}^{N_s} \sigma(\vec{r} - \vec{R}_j)$$

$$\sigma(\vec{r}) = \frac{Ze^2}{\epsilon}\frac{e^{-q_s r}}{r} ,$$
(III.10)

$\vec{R}_j$ being the coordinate of the j-th impurity, ϵ the dielectric constant, and q_s the screening length. The result is

$$\langle G_0(\varepsilon)\rangle_s = \sqrt{\frac{1}{\sqrt{\langle G_0(\varepsilon)\rangle_s} - \varepsilon}}$$
(III.11)

where

$$\zeta = \frac{1}{\pi} \frac{(V_{cl})}{(2\pi l)^2} \left(\frac{2m^*}{\hbar^2}\right)^{\frac{1}{2}} W$$

$$(\text{III}.12)$$

$$W = -\frac{N_s}{8V^2} l^4 \left(\frac{4\pi Z e^2}{\epsilon}\right)^2 \log\left(\frac{1}{2} l^2 q_s^2\right) .$$

That (III.11) is independent of k_3 follows from the fact that the coupling between energy bands are neglected.

Comparison between (III.11) and (III.7) at once yield the expression for the density of states

$$\rho(\varepsilon) = \frac{1}{W} \, \text{Im.} \, \left\langle G_o(\varepsilon) \right\rangle_s$$

$$(\text{III}.13)$$

where $\left\langle G_o(\varepsilon) \right\rangle_s$ can be solved from (III.11). Thus

$$\rho(\varepsilon) = \frac{1}{W}\frac{\sqrt{3}}{2}\left\{\left[\frac{\zeta^2}{2}+\frac{\varepsilon^3}{27} + \zeta\sqrt{\left(\frac{\zeta}{2}\right)^2+\left(\frac{\varepsilon}{3}\right)^3}\right]^{\frac{1}{3}} - \left[\frac{\zeta^2}{2}+\frac{\varepsilon^3}{27} - \zeta\sqrt{\left(\frac{\zeta}{2}\right)^2+\left(\frac{\varepsilon}{3}\right)^3}\right]^{\frac{1}{3}}\right\} \quad (\text{III}.14)$$

Other scattering potentials, for example acoustic phonons, will also give the same form of density of states. Only ζ will be different in (III.12). Although the calculation carried out here applie only to the extreme strong field limit, generalizations can readily be made to extend these results to include lower magnetic field cases. Substituting (III.14) into (III.1) and integrating over ε will yield the final expression for the spectrum. We will examine its shape more closely.

First let us look at $\rho(\varepsilon)$. Figure 1.3 shows the behavior of $\rho(\varepsilon)$ as a function of ε. It can be seen that the density of state has a peak at $\varepsilon = o$ as expected. The peak height is obtained by setting in (III.14)

$$\rho(0) = \frac{1}{W} \frac{\sqrt{3}}{2} \zeta^{2/3} \qquad . \qquad (\text{III.15})$$

At the high energy side, $\rho(\varepsilon)$ behaves like the unperturbed density of state having $1/\sqrt{\varepsilon}$ dependence

$$\rho(\varepsilon) \simeq \frac{\zeta}{W} \frac{1}{\sqrt{\varepsilon}} \quad , \qquad \varepsilon \gg \zeta^{2/3} \qquad . \qquad (\text{III.16})$$

This result is not surprising since at high energy, the collision potential is very small compared to H_o. Examining the low energy side shows that $\rho(\varepsilon)$ has a rather sharp cutoff at

$$\varepsilon_o = -3 \left(\frac{\zeta}{2} \right)^{2/3} \qquad . \qquad (\text{III.17})$$

There is no state allowed for $\varepsilon < \varepsilon_o$. This sharp cutoff is a consequence of neglecting the impurity band tail which we shall discuss in section VI. Expanding (III.14) around ε_o, we get

$$\rho(\varepsilon) \simeq \frac{(4\zeta)^{1/3}}{\sqrt{3}\,W} \sqrt{\varepsilon - \varepsilon_o} \quad , \qquad \varepsilon \ll \zeta^{2/3} \qquad . \qquad (\text{III.18})$$

The full width at half height of $\rho(\varepsilon)$ can now be easily solved. From (III.18) the half height is obtained, and equating it with (III.15) and (III.16) and solving for ε respectively, we get the half-peak-points on the high and low energy sides, the difference of these two gives us the full

width, which is

$$\Delta \mathcal{E} \cong 7.1 \; \zeta^{2/3} \qquad .$$

(III.19)

From (III.12) it can be seen that the width (III.19) increases linearly with N_s which is expected for more impurities means more collision, which rounds off the singularity peak. Also, $\Delta\mathcal{E}$ decreases with magnetic field as $B^{-2/3}$ which is just reasonable for higher magnetic field reduces the collision rate, hence sharpens the peak.

Having known the density of states, the lineshape follows immediately from (III.1). First consider the $\vec{q}.\vec{B}=0$ geometry discussed in section I. In this geometry $q_{\parallel}=0$ so that we do not have to worry about diffusions at all as can be seen from (II.26). Also, (II.25) shows that $F(\mathcal{E}) = 0$, thus the spectrum becomes

$$\frac{d^2\sigma}{d\omega d\Omega} = \left(\frac{e^2}{mc^2}\right)^2 \frac{\omega_f}{\omega_p^2} |\gamma|^2 \frac{\pi\hbar}{\lambda\omega_s} \; \rho\left(\frac{\omega_s-\omega}{\lambda\omega_s}\right)$$

$$\times \; \left\{ \left[\frac{\omega_s-\omega}{\lambda\omega_s} - \frac{\omega}{2}\right] \left\{ 1-f\left[\frac{\omega_s-\omega}{\lambda\omega_s} + \frac{\omega}{2}\right]\right\}\right\} \; .$$

(III.20)

The lineshape will look just like the density of states, with a peak at $\omega = \omega_s$ and a cutoff at both the high and low frequency sides by the Fermi factors.

Figure 1.4a shows schematically the lineshape in the "quantum limit", that is, when all electrons are in the spin up level of the zeroth Landau level. In this case the $\left[1 - f(\mathcal{E})\right]$ factor contributes little at low temperature, and the spectrum is only cutoff at the low frequency side by the Fermi energy. $\mathcal{E}_F$.

Under the extreme stron-g field limit, and when the carrier concentration is sufficiently high so that the Fermi energy $\mathcal{E}_F$ is much larger than the width of the density of states, the width of the spectrum is solely determined by the density of states, especially at low temperature. Thus we have

$$T_N \cong \lambda \omega_s \Delta \mathcal{E} = 7.1 \lambda \omega_s \zeta^{2/3} \quad , \qquad \mathcal{E}_F < \hbar \omega_s . \tag{III.21}$$

T_N is the nonparabolicity full spectral width at half power point. Since ω_s increases linearly with B , T_N can be seen to increase as $B^{1/3}$. This result will not be so surprising if we recall that the non-parabolicity of the Landau levels, specified by

$$\mu_B g_0 B \lambda \mathcal{E}$$

is an increasing function of B .

With the increase of carrier concentration or decrease of magnetic field, the Fermi level increases until $\mathcal{E}_F \simeq \hbar \omega_s$. At this point, electrons start to occupy the spin down level as well. This fact is reflected in the lineshape in figure 1.4b, where the $[1 - f(\mathcal{E})]$ factor now sets in and cuts off the sharp peak of the density of states. At zero temperature, the linewidth will be given by

$$T_N \simeq \lambda \omega_s (\hbar \omega_s) \quad , \qquad \hbar \omega_c > \mathcal{E}_F > \hbar \omega_s \tag{III.22}$$

which will be considerably greater than that given by (III.21). Further decrease in B will bring in the peak of the second Landau level, resulting in a narrow linewidth. Thus we will have an linewidth as an oscillatory

function of the magnetic field. We will however not consider these and only concentrate on the extremely strong field limit.

Now we turn to the $\vec{q}.\vec{B} \neq 0$ geometry. Figure 1.5 shows that the spectrum has a sharp peak just as in the $\vec{q}.\vec{B}=0$ case, but the peak is shifted by

$$ -\left(1 - \tfrac{1}{2}\lambda\omega_s\right)\frac{\hbar^2 q_z^2}{2m^*} \quad . \tag{III.23} $$

This peak seats on a low broad bump. The shifted peak determines the width which is approximately equal to (III.21).

It should be noted here that for a fixed B and N , no matter what the spectral shape may be, the area under the spectrum must be a constant. This can be seen from (II.36), as an integration over ω just gives the integrated cross section for the N electrons, independent of the lineshape.

IV   DIFFUSION DOMINATED LINESHAPE

Now we turn our attention to cases where $q_\perp^2 D$ is much larger than the width of the density of states calculated in the last section. Under this situation the structures exhibited by $\rho(\varepsilon)$ is buried in the broad Lorentzian-like line caused by the diffusion of electrons so that we may neglect nonparabolicity effects by setting $\lambda = 0$. As mentioned in section III,

this limit of large diffusion does not apply to the $\vec{q}.\vec{B}=0$ geometry in which q_{δ} is zero. Thus we will only consider the $\vec{q}.\vec{B} \neq 0$ case.

With $\lambda = 0$, (II.36) reduces at once to

$$\frac{d^2\sigma}{d\omega d\Omega} = \left(\frac{e^2}{mc^2}\right)^2 \frac{|\gamma|^2}{2} \frac{\omega_f}{\omega_i} \frac{2q_\delta^2 D}{[\omega_s - \omega]^2 + (q_\delta^2 D)^2}$$

$$\times \int_0^\infty d\varepsilon\, f(\varepsilon) \left\{ \left[\varepsilon - \frac{\hbar\omega_s}{2}\right] \right\} \left\{ 1 - f\left[\varepsilon + \frac{\hbar\omega_s}{2} + F(\varepsilon)\right] \right\} .$$

(IV.1)

The integral in (VI.1) just gives the effective number of electrons that can be scattered N_{eff} , so that the spectrum is simply a Lorentzian with full width Γ_D

$$\frac{d^2\sigma}{d\omega d\Omega} = \left(\frac{e^2}{mc^2}\right)^2 |\gamma|^2 \frac{\omega_f}{\omega_i} N_{eff} \frac{\Gamma_D/2}{(\omega_s - \omega)^2 + (\Gamma_D/2)^2}$$

(IV.2)

$$\Gamma_D = 2 q_\delta^2 D .$$

(IV.3)

In contrast to the nonparabolicity lineshape for this geometry, whose peak is shifted, this diffusion spectrum is centered at $\omega = \omega_s$.

For a system of nondegenerate electrons with a Maxwellian velocity distribution, the diffusion coefficient along the magnetic field D in (IV.3) is given by

$$D = \frac{k_B T}{m^*} \tau .$$

(IV.4)

An extension of the Einstein relation (IV.4) to degenerate electrons yields [17]

$$D = s^2 \tau \qquad \text{(IV.5)}$$

where the velocity of sound s for non-interacting electrons is given by

$$s^2 = \frac{2\,\mathcal{E}_F}{3m^{*2}} \; . \qquad \text{(IV.6)}$$

In Appendix 1F τ is calculated for elastic collisions with impurities via (III.10), and the result is quoted here

$$\frac{1}{\tau} = \frac{4}{\hbar} \frac{1}{\sqrt{\overline{\mathcal{E}_\delta}}} \; \zeta \qquad \text{(IV.7)}$$

where $\overline{\mathcal{E}_\delta}$ is the averaged electronic kinetic energy and ζ is defined in (III.12). In low temperature, $k_B T \ll \mathcal{E}_F$, an expansion of the Fermi distribution gives (see Appendix 3B),

$$\frac{1}{\tau} \simeq \frac{8}{\hbar} \frac{\zeta}{\sqrt{\mathcal{E}_F}} \left\{ 1 - 24 \left(\frac{\pi k_B T}{\mathcal{E}_F}\right)^2 - \frac{7}{384} \left(\frac{\pi k_B T}{\mathcal{E}_F}\right)^4 \right\}, \qquad k_B T \ll \mathcal{E}_F . \quad \text{(IV.8)}$$

For high temperature $k_B T \gg \mathcal{E}_F$,

$$\frac{1}{\tau} \simeq \frac{4}{\hbar} \zeta \sqrt{\frac{\pi}{k_B T}} , \qquad k_B T \gg \mathcal{E}_F . \qquad \text{(IV.9)}$$

Substitution of (IV.5),(IV.6) and (IV.8) or (IV.9) into (IV.3) gives the full width of the diffusion lineshape Γ_D . At low temperatures

$$\Gamma_D \simeq \frac{1}{3}\left(\frac{\hbar^2 q^2}{2m^*}\right)\mathcal{E}_F^{3/2} \frac{1}{\zeta}\left\{1 - \frac{1}{24}\left(\frac{\pi k_B T}{\mathcal{E}_F}\right)^2 - \cdots \right\} , \qquad k_B T \ll \mathcal{E}_F . \quad \text{(IV.10)}$$

For electrons in the extremely strong field limit,

$$\mathcal{E}_F = \left(\frac{N}{2}\right)^2 (2\pi \ell)^4 \frac{\hbar^2}{2m^*}$$

(IV.11)

so that Γ_D is proportional to N^2/B^2 . The factor $\ell^2 q_s^2$ is, of course, dependent on N and B , but their effects will be small for only their lagrithmic values contribute . At high temperature,

$$\Gamma_D \simeq \frac{1}{3} q^2 \frac{\hbar^2}{m^{*2}} \frac{\mathcal{E}_F}{3} \sqrt{\frac{k_B T}{\pi}} \qquad\qquad k_B T \gg \mathcal{E}_F$$

(IV.12)

which is proportional to $\sqrt{T} N /B$. Thus we see that the spectral width increases both with carrier concentration and temperature, while it decreases with magnetic field. This result is reasonable, for although high T and N and lower B will shorten the collision time, they will however increase the average velocity of the electron, hence increase the diffusion coefficient.

Note that the calculation in section III and IV is valid only for temperatures low enough so that the collisions with phonons are not important. For InSb, mobility measurements [18] show that phonon effects will not come in for T<100°K. For temperatures higher than that $\mathcal{J}$ in (III.12) has to be modified to include the phonon effects. Also, (IV.11) is only true if all the electrons are in the lowest Landau level. For higher N or lower B the Fermi energy is more complicated. Morover, (IV.11) gives the Fermi energy at zero temperature, the change of $\mathcal{E}_F$ in finite temperatures must be taken into account to give the correct linewidth at T = 0. The behavior of $\mathcal{E}_F$ as a function of B , N and T is discussed in Appendix 3B .

Finally the calculation in this section holds only if T_D is large compared to T_N obtained in the last section. If T_D and T_N are comparable, we cannot use any of the approximations developed in sections III and IV, and must go back to (II.36) for the spectral shape. Since T_D decreases with B and T_N increases with B, at some large field value (II.36) seemed unavoidable.

V. COMPARISON WITH EXPERIMENT

In this section we will mainly compare our results with InSb scattering datas provided by Brueck.[1] In his experiemnts, InSb is scattered with a CO laser, with energy very close to the energy gap. In such cases, γ_0 can depend quite heavily on energy as the resonance enhancement decreases with finite k_δ. This effect can be taken into account by letting in (II.26)

$$\gamma_0 = \bar{\gamma}_0 \frac{(E_g + \hbar\omega_c/2)^2 - \hbar\omega_p^2}{(E_g + \hbar\omega_c/2 + \varepsilon)^2 - \hbar\omega_p^2} \qquad (V.1)$$

where $\bar{\gamma}_0$ is the matrix element at $k_\delta = 0$. Also, the experimental measurements have been done in low temperature $T \lesssim 50°K$ so that phonon contributions will not be important. In Appendix 1G the formulation will be extended to include the situations in which many Landau levels are occupied as well as effects of higher temperatures. The results obtained will be compared with data of light scattering from CdS there.

First consider the $\vec{q}.\vec{B}=0$ geometry. As pointed out in section IV, diffusion effects does not contribute to the lineshape in this particular case, so that the results of section III for a nonparabolicity dominated lineshape will be used. The screening length q_s is calculated in Appendix 1E and we assume here that the semiconductor is not compensated, so that $ZN_s = N$.

In Figure 1.6 is plotted the lineshape given by (III.21) as a function of magnetic field for $N = 10^{16}$ cm^{-3} and T=2°K. Note that (III.21) is valid only if the electrons are in the quantum limit, which, in the given carrier concentration, should occur at about $B \cong 25$ KG. When the magnetic field falls below that, there will be an increase of the linewidth as the sharp peak is cut off. Experimentally, this effect can be seen in Figure 1.6 by the larger than usual linewidth at 20 KG. The calculated linewidth is about 1 cm^{-1}, and is in general two times larger than the experimental measurements, which is about 0.5 cm^{-1}. This discrepency is especially large at high fields, because our width tends to increase with field. This is most probably due to an over estimation of the impurity collision rate when calculating τ . However, if taking the fact that ours is a first principle calculation with no fitting parameters at all, this can be considered as an acceptable agreement.

Equation (III.21) provides the linewidth only at extremely low temperatures such that the Fermi distributions are essentially step functions. At high temperatures, there is no simple analytic solutions for Γ_N , we have to plot the spectrum (III.20) and measure the width. Figure 1.7 shows the spectrum

for $N = 10^{16}$ cm^{-3} and B = 49KG at $2°$K and $50°$K. The peak height is reduced as temperature increases because of the thermal distribution of electrons. The linewidth is however little affected by temperature for $T \leq 70°$K.

In Figure 1.8 the linewidths for $N = 10^{16}$ cm^{-3} and $T = 50°$K is given as a function of B. The widths are again bigger than experimental results. The sudden drop at $B \simeq 25$ KG indicates that the electrons pass into the quantum limit, as discussed earlier. The effects of a partially occupied spin down level as the system leaves the quantum limit can best be seen from Figure 1.9, which shows the spectrum at $T = 2°$K and B = 49 KG for several carrier concentrations. For $N = 8 \times 10^{15}$ cm^{-3}, the system is strictly in the quantum limit, so that the spectrum shows a sharp peak at $\omega = \omega_s$. As the carrier concentration is increased to 2×10^{16} cm^{-3}, the Fermi energy just touches the bottom of the spin down sublevel, resulting in a reduction of the spectral peak. A further increase of carrier concentration to 3×10^{16} cm^{-3} will completely wipe out any peaking structure as the spin down sublevel is well occupied. .

The spectral shape, however, does not check with experiment as favorably. Figures 1.7, 1.10 and 1.11 shows the lineshape for $N = 10^{16}$ cm^{-3} at various magnetic field values and temperatures. Reproduced experimental traces accompanying each figure are for purpose of comparison. As can be seen, the theoretical curves are generally asymtrical showing a tail at the low frequency side and a much faster drop at the high frequency side. This tailing just reflect that each electron has a different effective g-value. That

the tail is at the low frequency side is a direct consequence of a negative λ

which means that the separation of the two spin sublevels is largest at $k_{\bar{3}} = 0$.

Should λ change sign, the mirror image of the spectrum shown will

result. This low frequency tail, if present, is however not prominent

in the experimental results. Instead, some traces show a distinct tailing

at the high frequency side in contrast to the sharp drop predicted by theory.

This disagreement in spectral shape is probably a result of neglecting effects

such as Coulomb interactions between electrons, deep impurity potential wells,

as well as the anisotropy of the energy bands in our calculation.

Now we turn to the $\vec{q}.\vec{B} \neq 0$ geometry. In this case the diffusion width

will in general be of order of several wave numbers, larger than the nonpara-

bolicity width. Thus we will use the results of section IV. The spectrum

will be Lorentzian centering at $\omega = \omega_0$. Thus,the peak will not be shifted

with the change of experimental geometry as long as the electron system is

in the quantum limit. Once the spin down level is occupied, the $\vec{q}.\vec{B}=0$

peak will be shifted to the low frequency side by an amount

$$\Delta \omega = \lambda \omega_s (\varepsilon_F / \hbar - \omega_s)$$
(V.2)

as can be seen from figures 1.4b and 1.9. The peak separations of the two

geometries are given in Figure 1.12, and agrees very well with experiment.

The line widths as given by (IV.10) is ploted for 2° K in Figure 1.6.

In low magnetic field, the width predicted is too big, but in high fields,

droping as B^{-2} , is quite close to the experimental measurements. A

better agreement is obtained for $T = 50°K$ by using (IV.10) as given in Figure 1.8. In general the agreement between theory and experiment is not bad.

The spectral shape will be a simple Lorentzian if γ_o is taken to be a constant. If we take into account the resonance enhancement by using γ_o as given in (V.1), the spectrum becomes slightly assymmetric. Figure 1.13 and Figure 1.14 gives the lineshapes for different fields and temperatures for both constant γ_o and (V.1). The spectrum agrees quite well with experimental observations as can be seen by comparing with the accompanying traces.

In general, we may say that our theory are in rather good confirmation with experimental observations, except for the detailed spectral shape in certain cases. The discrepancies will be discussed in the next section.

VI. DISCUSSIONS

From the above section we may say that the diffusion dominated lineshape checks quite well with experiment. The slightly larger than observed linewidth may due to the rather crude methods used in calculating the diffusion constant. Other collision mechanisms such as elastic collisions with phonons may help to narrow the width. In high magnetic fields, when the width is comparable to Γ_N' as shown in Figure 1.6, the result should be modified

to take into account nonparabolicity. An integration of (II.36) should be carried out to yield the correct width in these high hield limits. This however is not done in this thesis.

Besides the approximations made to arrive at our results, there are several realistic features and broadening mechanisms of the semiconductor neglected in this calculation. This must be born in mind when comparing with experiment. First of all, the energy band is assumed to be isotropic, for we used a single effective g-value for all directions. For anisotropic band structures, different g-value should be used for each direction, and it may well turn out that along some specific direction g_{eff} will have a positive λ , so that there will also be a tail on the high frequency side. This effect is not important for InSb, whose conduction bands are quite isotropic.

Another feature not considered here is the impurity band tail of the density of states. In our consideration of randomly distributed impurity centers, we have not taken into account those impurities forming a cluster, thus creating a deep potential well. This effect is also small because although the electrons trapped in these potential wells have very low potential energy, they also have high kinetic energies.[19]

Finally, we have neglected Coulomb interaction between electrons. When this is included, the following electron-electron collision processes may occur. Figure 1.15a shows the collision between two electrons with different spins.

The collision changes the energies and momentums of the electrons but leaves the spin state unchanged. These collisions do not contribute to the linewidth since they do not connect spin as discussed in section I. However, it provides a calculation of the electronic collision rate within the same spin-sublevel. An estimation shows that this rate is about $\sim 5 \times 10^{10} \sec^{-1}$.

Another possible broadening mechanism when electronic Coulomb interaction is included is the "Auger effect" of Figure 1.15b. Here, the effective frequency shift may be bigger than ω_s as the broken line in Figure 1.15b shows. This may account for the tailing of the spectrum at the high frequency side in experimental observations. A detailed calculation of this effect is complicated and we hope to carry it out in the future.

APPENDIX 1A. CALCULATION OF EFFECTIVE g-VALUE

The Lax two-band model [7] gives the energy of the nth Landau level

$$E_n = \frac{1}{2}\left\{\sqrt{E_g^2 + 4E_g\left[(n+\tfrac{1}{2})\hbar\omega_c + \frac{\hbar^2 k_z^2}{2m^*}\right] \pm \tfrac{1}{2}\mu_B g_0 B} - E_g\right\} \tag{1A.1}$$

where E_g is the band gap and g_0 the effective g-value at

$$E \triangleq (n+\tfrac{1}{2})\hbar\omega_c + \frac{\hbar^2 k_z^2}{2m^*} = 0 \quad . \tag{1A.2}$$

The $\pm$ signs refer to the spin up and down sublevels respectively. Since the spin-orbit splitting is small compared to other energies, expansion of the square root in (1A.1) gives

$$E_n \simeq \frac{1}{2}\left\{\sqrt{E_g^2 + 4E_g E} - E_g \pm \frac{E_g}{\sqrt{E_g^2 + 4E_g E}}\,\mu_B g_0 B\right\} \quad . \tag{1A.3}$$

The last term in (1A.3) is just $\mu_B g_{eff} B$. For $E \ll E_g$, we finally get, to first order in E ,

$$g_{eff} \simeq g_0\left(1 - 2E/E_g\right) \quad . \tag{1A.4}$$

APPENDIX 1B   FERMI-DIRAC OPERATOR TO SINGLE PARTICLE OPERATOR REDUCTION

Let H be the sum of one-particle hamiltonians,

$$H = \sum_i H_i$$

and $\underline{A}(t)$ and $\underline{B}(t)$

$$\underline{A}(t) = e^{iHt/\hbar} \underline{A}(0) e^{-iHt/\hbar}$$

$$\underline{B}(t) = e^{iHt/\hbar} \underline{B}(0) e^{-iHt/\hbar} \tag{1B.1}$$

be any two second quantized operators acting on many electron states

$$\underline{A}(t) = \sum_{\alpha\beta} \langle \alpha | A(t) | \beta \rangle a^{\dagger}_{\alpha} a_{\beta} \triangleq \sum_{\alpha\beta} A_{\alpha\beta}(t) a^{\dagger}_{\alpha} a_{\beta}$$

$$\underline{B}(t) = \sum_{\alpha\beta} \langle \alpha | B(t) | \beta \rangle a^{\dagger}_{\alpha} a_{\beta} \triangleq \sum_{\alpha\beta} B_{\alpha\beta}(t) a^{\dagger}_{\alpha} a_{\beta} \tag{1B.2}$$

where the a 's are Fermi Dirac operators [25]

$$a_i | \cdots n_i \cdots \rangle = \sqrt{n_i}\, (-1)^{\sum_{j<i} n_j} | \cdots n_i - 1 \cdots \rangle \tag{1B.3}$$

and $A(t)$, $B(t)$ are single electron operators operating on one-electron states. In this appendix we will try to show that

$$\langle A(t)\, \underline{B}(0) \rangle = tr \left\{ f(H) A(t) [1 - f(H)]\, B(0) \right\} \tag{1B.4}$$

where $f(H)$ is the Fermi-Dirac distribution.

With equation (1B.2), we get

$$\langle \underline{A}(t)\, \underline{B}(0) \rangle = \sum_{\alpha\beta\mu\nu} A_{\alpha\beta}(t)\, B_{\mu\nu}(0) \langle a^{\dagger}_{\alpha} a_{\beta} a^{\dagger}_{\mu} a_{\nu} \rangle$$

$$= \sum_{\alpha\beta\mu\nu} A_{\alpha\beta}(t) B_{\mu\nu}(0)\, tr \left\{ a^{\dagger}_{\alpha} a_{\beta} a^{\dagger}_{\mu} a_{\nu} \frac{e^{-(H-\mu N)/k_B T}}{tr\left(e^{-(H-\mu N)/k_B T}\right)} \right\} \tag{1B.5}$$

where we have averaged over a canonical distribution. After some operator algebras, (1B.5) reduces to [20]

$$\langle \underline{A}(t)\underline{B}(0)\rangle = \sum_{\alpha\beta\mu\nu} A_{\alpha\beta}(t) B_{\mu\nu} \left\{ f_\alpha(1-f_\mu) \delta_{\alpha\nu}\delta_{\beta\mu} + f_\alpha f_\mu \delta_{\alpha\beta}\delta_{\mu\nu} \right\} \tag{1B.6}$$

with

$$f_\alpha = \langle \alpha | f(H) | \alpha \rangle . \tag{1B.7}$$

Suming over indices μ and ν , (1B.6) becomes

$$\langle \underline{A}(t)\,\underline{B}(0)\rangle = \sum_{\alpha\beta} f_\alpha (1-f_\beta)\, A_{\alpha\beta}(t)\, B_{\beta\alpha}(0)$$

$$= \mathrm{tr} \left\{ f(H)\, A(t)\, [1-f(H)]\, B(0) \right\} . \tag{1B.8}$$

APPENDIX 1C   A DIFFERENT FORMULATION FOR THE NONPARABOLICITY DOMINATED LINESHAPE

A formulation of the nonparabolicity dominated lineshape slightly different from that developed in section II is given here. In this formulation we will relax the approximation of neglecting the $\lambda \omega_s V$ term in (II.23). For simplicity, diffusion contributions will be ignored here. Also only the $\vec{q}.\vec{B}=0$ case is considered, although it is straight forward to generalize the results to account for the $\vec{q}.\vec{B} \neq 0$ geometry.

We will start with equation (II.14), with the N 's given by equation (II.15), where γ_0 is approximated to be a constant. This, together with the model for calculating g_{eff} , and that the scattering potential does not flip spins (II.21), are all the approximations necessary in the present formulation. With γ_0 a constant, it can easily be shown that

$$[H_0, N] = 0$$

$$[V, N] = 0 \quad .$$

(1C.1)

That the commutator between V and N vanishes follows from the fact that V does not connect states of different spins. Using (1C.1) and (II.16), (II.14) can be written as

$$\frac{d^2\sigma}{d\omega d\Omega} = \left(\frac{e^2}{mc^2}\right)^2 \frac{\omega_f}{\omega_p} \frac{1}{2} \int_{-\infty}^{\infty} dt\, e^{i\omega t}\, \text{tr}\left\{ \int [H - \frac{\hbar\omega_s}{2}(1-\lambda H_0)] \right.$$

$$\times\, e^{i[H - \frac{\hbar\omega_s}{2}(1-\lambda H_0)]t/\hbar}\, e^{-i[H + \frac{\hbar\omega_s}{2}(1-\lambda H_0)]t/\hbar}$$

(1C.2)

$$\times \left[1 - \int\left(H + \frac{\hbar\omega_s}{2}(1-\lambda H_0)\right)\right] N^+ N \left. \right\} \quad .$$

Now we introduce the hamiltonian for the spin up electrons

$$\mathcal{H} \triangleq H - \frac{\hbar\omega_s}{2}(1-\lambda H_0) \quad ,$$

(1C.3)

The hamiltonian for spin down electrons can be written in terms of $\mathcal{H}$

$$H + \frac{\hbar\omega_s}{2}(1-\lambda H_0) = \alpha\,\mathcal{H} + \tilde{\omega}_s + \lambda\tilde{\omega}_s V$$

(1C.4)

where

$$\alpha \overset{\Delta}{=} \frac{1 - \frac{1}{2}\lambda\hbar\omega_s}{1 + \lambda\hbar\omega_s/2}$$

$$\tilde{\omega}_s \overset{\Delta}{=} \frac{\omega_s}{1 + \lambda\hbar\omega_s/2} \quad . \tag{1C.5}$$

Putting (1C.3) - (1C.5) into (1C.2) we get

$$\frac{d^3\sigma}{d\omega d\Omega} = \left(\frac{e^2}{mc^2}\right)^2 \frac{1}{2} \frac{\omega_f}{\omega_p} \int_{-\infty}^{\infty} dt \, e^{i\omega t} \int_0^{\infty} d\varepsilon \, f(\varepsilon) \, \text{tr} \left\{ \delta(\varepsilon - \mathcal{H}) \, e^{i\varepsilon t/\hbar} \right.$$

$$\left. \times \, e^{i[\alpha\mathcal{H} + \tilde{\omega}_s(1+\lambda V)]t/\hbar} \left[1 - f(\alpha\mathcal{H} + \tilde{\omega}_s(1+\lambda V)) \right] N^+ N \right\} \quad . \tag{1C.6}$$

Integrating over time, and tracing with the eigenstates of H_o , (1C.6) becomes

$$\frac{d^2\sigma}{d\omega d\Omega} = \left(\frac{e^2}{mc^2}\right)^2 \frac{1}{2} \frac{\omega_f}{\omega_p} \int_0^{\infty} d\varepsilon \, f(\varepsilon) \left[1 - f(\varepsilon + \hbar\omega) \right]$$

$$\times \, \text{tr} \left\{ \delta(\varepsilon - \mathcal{H}) \, \delta[\varepsilon + \hbar\omega - \alpha\mathcal{H} - \tilde{\omega}_s(1+\lambda V)] \right\} \quad . \tag{1C.7}$$

Carrying out the trace with eigenstates of the spin up electrons $|\varphi\rangle$

$$\mathcal{H} |\varphi\rangle = \mathcal{E}_\varphi |\varphi\rangle \quad , \tag{1C.8}$$

(1C.7) becomes

$$\frac{d^2\sigma}{d\omega d\Omega} = \left(\frac{e^2}{mc^2}\right)^2 \frac{1}{2} \frac{\omega_f}{\omega_p} \int_0^{\infty} d\varepsilon \, f(\varepsilon) \left[1 - f(\varepsilon + \hbar\omega) \right]$$

$$\times \, \sum_\varphi \delta(\varepsilon - \mathcal{E}_\varphi) \langle\varphi| \, \delta[\varepsilon + \hbar\omega - \alpha\mathcal{H} - \tilde{\omega}_s(1+\lambda V)] |\varphi\rangle \tag{1C.9}$$

which, if the term $\lambda\tilde{\omega}_s V$ is neglected, gives (III.1).

Since only the diagonal elements of the delta function $\delta[\varepsilon + \hbar\omega - \alpha\mathcal{H} - \tilde{\omega}_s(1+\lambda V)]$ is involved in (1C.9), we can replace it by the resolvent operator [10]

$$S(\varepsilon') = \frac{\Gamma(\varepsilon')/\pi}{(\alpha\mathcal{H} + \Delta(\varepsilon') - \varepsilon')^2 + \Gamma^2(\varepsilon')} \qquad (1C.10)$$

$$\varepsilon' \triangleq \varepsilon + \hbar\omega - \tilde{\omega}_s \ . \qquad (1C.11)$$

The $\Gamma(\varepsilon')$ and $\Delta(\varepsilon')$ in (1C.10), defined by

$$\lim_{\eta \to 0} G(\varepsilon \pm i\eta) = \Delta(\varepsilon) \mp i\Gamma(\varepsilon) \qquad (1C.12)$$

are just the linewidth and the energy shift of the eigenstates $|\varphi\rangle$ respectively. The Green's function $G(S)$ is given by

$$G(S) = \lambda\tilde{\omega}_s\{V\}_d - \left\{V \frac{1}{\alpha\mathcal{H} + G(S) - S}V\right\}_d (\lambda\tilde{\omega}_s)^2 \qquad (1C.13)$$

where the first term, which is a constant, can be removed by renormalization. $\{\cdots\}_d$ denotes the diagonal parts involved. Note that the second term in (1C.13) is small because it involves the square of $\lambda\tilde{\omega}_s$, hence may be neglected. This approximation is essentially neglecting the $\Gamma(\varepsilon')$ in (1C.10) and only keeping the energy shift. Thus (1C.9) becomes, after substituting in (1C.10),

$$\frac{d^2\sigma}{d\omega d\Omega} = \left(\frac{e^2}{mc^2}\right)^2 \frac{\omega_f}{\omega_p} \frac{1}{2} \int_0^\infty d\varepsilon \, f(\varepsilon) \left[1 - f(\varepsilon + \hbar\omega)\right] \qquad (1C.14)$$

$$\times \sum_\varphi \delta(\varepsilon - \varepsilon_\varphi) \, \delta\left[(1-\alpha)\varepsilon + \tilde{\omega}_s\left(\frac{\omega}{\omega_s} - 1\right) - \lambda\tilde{\omega}_s V_\varphi\right]$$

where

$$V_\varphi \; \triangleq \; \langle \varphi \,|\, V \,|\, \varphi \rangle \quad . \qquad\qquad (1C.15)$$

In principle, (1C.14) can be solved if we know the wavefunctions $|\varphi\rangle$. If we approximate $|\varphi\rangle$ by $V_\alpha \triangleq \langle \alpha \,|\, V \,|\, \alpha \rangle$ where $|\alpha\rangle$ is the eigenstates of H_0, then (1C.14) at once reduce to (III.1) except the entire spectrum is shifted to the high frequency side by $\lambda \tilde{\omega}_s V_\alpha$.

APPENDIX 1D   GREEN'S FUNCTION FOR IMPURITY SCATTERINGS

In this Appendix we shall calculate the self energy [10] (III.9) for electronic scatterings with N_s randomly distributed impurity centers via an attractive screened Coulomb potential (III.10). Using the Fourier transform of the scattering potential

$$V(\bar{q}) \; = \; \frac{1}{V_{ol}} \sum_{N=1}^{N_s} e^{-i\bar{q}\cdot R_j} \, \upsilon(\bar{q})$$

$$\upsilon(\bar{q}) \; = \; \left(\frac{4\pi Z e^2}{\epsilon}\right)^2 \frac{1}{q^2 + q_s^2} \qquad\qquad (1D.1)$$

the matrix element in (III.9) becomes

$$\left\langle \left| \langle n k_y k_j | V(\bar{r}) | n' k_y' k_j' \rangle \right|^2 \right\rangle_s \; = \; \sum_{\bar{q}} \sum_{\bar{q}'} \left\langle V(\bar{q}) \, V^*(\bar{q}') \right\rangle_s \left| J_{nn'}^*(k_y, q_x, k_y') \right|$$

$$\qquad\qquad (1D.2)$$

$$\times \; \left| J_{nn'}(k_y, q_x', k_y') \right| \, \delta_{k_y', k_y + q_y} \, \delta_{k_j', k_j + q_j} \, \delta_{k_y, k_y + q_y'} \, \delta_{k_j, k_j' + q_j'}$$

where [16]

$$J_{nn'}(k_y, q_x, k_y') = \int dx\, \varphi_n(x - \ell^2 k_y)\, e^{iq_x X}\, \varphi_{n'}^*(x - \ell^2 k_y') . \tag{1D.3}$$

The φ_n's in (1D.3) is the wave function for the state $|nk_y k_z\rangle$. If we neglect the nonparabolicity effect of the energy band structure, $\varphi_n(x - \ell^2 k_y)$ will just be proportional to the nth order harmonic oscillator wavefunction ψ_n [21]

$$\varphi_n(x - \ell^2 k_y) = e^{i(k_y y + k_z z)}\, \psi_n(x - \ell^2 k_y) . \tag{1D.4}$$

Averaging over the random scatterers, [22] we get

$$\langle V(\vec{q})\, V^*(\vec{q}') \rangle_s = \frac{N_s}{V_o^2}\, |v(\vec{q})|^2\, \delta_{qq'} , \tag{1D.5}$$

where V_o is the volume of the crystal. (1D.2) then becomes

$$G(s) = -\sum_{n'k_y'k_z'}\sum_{\vec{q}} \frac{N_s}{V_o^2} \frac{|v(\vec{q})|^2\, |J_{nn'}(k_y, q_x, k_y')|^2}{n'\hbar\omega_c + \hbar^2 k_z'^2/2m^* + G(s) - s}\, \delta_{k_y', k_y + q_y}\, \delta_{k_z', k_z + q_z} . \tag{1D.6}$$

If only elastic collisions are considered for an electronic system in the quantum limit,

$$k_z = k_z'$$
$$n = n' = 0 . \tag{1D.7}$$

With (1D.7), by converting the summation to an integral, (1D.6) can be reduced to

$$G(s) = -\frac{N_s}{V_o}\left(\frac{4\pi Z e^2}{\epsilon}\right)^2 \left(\frac{\ell}{2\pi}\right)^2 \frac{1}{8\pi}\left(\frac{2m^*}{\hbar^2}\right)^{\frac{1}{2}} e^{\frac{1}{2}\ell^2 q_s^2} \frac{1}{\sqrt{G(s) - s}} \tag{1D.8}$$

$$\times \left\{ 0.577 + \log(\ell^2 q_s^2/2) - \ell^2 q_s^2/2 + \cdots \right\} .$$

where the screening length q_s is calculated in the next appendix. In general, $\ell^2 q_s^2$ is very small, so that we may neglect the first and third terms in the parentheses of (1D.7) in comparison with $\log(\ell^2 q_s^2/2)$. Also, $e^{\ell^2 q_s^2/2} \simeq 1$ so that we get finally

$$G(s) = -\frac{N_s}{V_{ol}}\left(\frac{4\pi Z e^2}{\epsilon}\right)^2 \left(\frac{\ell}{2\pi}\right)^2 \frac{1}{8\pi}\left(\frac{2m^*}{\hbar^2}\right)^{1/2} \log(\ell^2 q_s^2/2) \frac{1}{\sqrt{G(s)-s}}$$

$$\overset{\Delta}{=} 7 \frac{1}{\sqrt{G(s)-s}}$$

(1D.8)

APPENDIX 1E   SCREENING LENGTH IN A MAGNETIC FIELD

Celli and Mermin [24] developed a detailed calculation of the Coulomb screening length for an electronic plasma in a magnetic field. We will use their results here,

$$q_s^2 = 4\pi e^2 \left| L^0(k_\perp, k_z) \right|$$

(1E.1)

where

$$L_0 = \frac{m^* \omega_c}{\hbar^2} \int \frac{d\not{p}}{(2\pi)^2} \sum_{nn'} \frac{f[\mathcal{E}_{n\downarrow}(\not{p}-\frac{1}{2}k_z)] - f[\mathcal{E}_{n'\uparrow}(\not{p}+\frac{1}{2}k_z)]}{\mathcal{E}_{n\uparrow}(\not{p}-\frac{1}{2}k_z) - \mathcal{E}_{n\downarrow}(\not{p}-\frac{1}{2}k_z)} \left| \langle n | e^{\frac{i k_\perp^2}{2m^* \omega_c}} | n' \rangle \right|^2$$

(1E.2)

First of all, we observe that

$$f[\mathcal{E}_{n\delta}(p)] \simeq 0 \quad , \qquad n \neq 0, \quad \delta = \uparrow, \downarrow$$

(1E.3)

$$f[\mathcal{E}_{0\uparrow}(p + \tfrac{1}{2}k_3)] \simeq 0 \; ,$$

since we are only interested in the quantum limit in which all electrons are in the spin up sublevel of the zeroth Landau level. Also, we may approximate

$$\mathcal{E}_{0\downarrow}(p - \tfrac{1}{2}k_3) - \mathcal{E}_{0\uparrow}(p + \tfrac{1}{2}k_3) \simeq \hbar\omega_s + \tfrac{1}{4}\tfrac{\hbar^2}{2m^*}(k_3^2 - 4pk_3) \; .$$

(1E.4)

Finally, as pointed out earlier, $k_\perp \ll k_3$, so that (1E.2) becomes

$$L_0 = \frac{m^*}{\hbar} \frac{\omega_c}{(2\pi)^2} \int_0^\infty dp \; \frac{f[\mathcal{E}(p - k_3/2)]}{\hbar\omega_s + \hbar^2/8m^* (k_3^2 + 2k_3 p)}$$

(1E.5)

For $\hbar^2 k_3^2/8m^* \ll \hbar\omega_s$, the integration in (1E.5) can be carried out to give

$$q_s^2 \simeq \frac{1}{2\pi} e^2 \left(\frac{2m^*}{\hbar^2}\right)^{3/2} \frac{\omega_c}{\omega_s} \sqrt{\mathcal{E}_F} \; .$$

(1E.6)

APPENDIX 1F   EFFECTIVE COLLISION TIME

Here we calculate the effective collision time τ which will be used in the diffusion linewidth calculation. Consider the scattering potential (III.10), for scatterings in the quantum limit, transition rates due to elastic collisions

is given by the Golden rule

$$\frac{1}{\tau} = \frac{2\pi}{\hbar} \sum_{k_y''k_3'} \left\langle \left| \langle 0 k_y k_3 | V(r) | 0 k_y' k_3' \rangle \right|^2 \right\rangle_s \delta\left[\frac{\hbar^2 k_3^2}{2m^*} - \frac{\hbar^2 k_3'^2}{2m^*} \right]$$ (1F.1)

Carrying out the same kind of analysis as leading to equation (1D.8), we get

$$\frac{1}{\tau} = \frac{4}{\hbar} \left(\frac{2m^*}{\hbar^2 k_3^2} \right)^{\frac{1}{2}} \bar{\varepsilon}$$ (1F.2)

where the averaged energy is given by

$$\sqrt{\bar{\varepsilon}_3} \triangleq \left(\frac{2m^*}{\hbar^2 \Gamma^2} \right)^{\frac{1}{2}} = \frac{\int_0^\infty \rho(\varepsilon) f(\varepsilon) \sqrt{\varepsilon}\, d\varepsilon}{\int_0^\infty \rho(\varepsilon) f(\varepsilon)\, d\varepsilon}$$ (1F.3)

APPENDIX 1G   SPIN FLIP SCATTERING FROM n-CdS

Here we will give a brief discussion of the spin flip scattering lineshape of CdS. We will only consider the $\vec{q}.\vec{B}=0$ geometry. In CdS, besides impurity scatterings, we must also consider the acoustic phonons, since the electron-phonon interaction in CdS is much stronger that in InSb. Electron interacts with acoustic phonons with potential [22]

$$V(\vec{r}) = \sum_{\vec{q}} \left\{ \left(\frac{2\pi\alpha\hbar e^2 s}{\varepsilon V_{ol}} \right)^{\frac{1}{2}} \frac{1}{\sqrt{q}} + C_1 \left(\frac{\hbar^2}{2 V_{ol}\rho_d \omega_q} \right)^{\frac{1}{2}} |q| \right\}$$ (1G.1)

$$\times \left\{ b_{\vec{q}}\, e^{i\vec{q}\cdot\vec{r}} + b_{\vec{q}}^\dagger\, e^{-i\vec{q}\cdot\vec{r}} \right\} \quad ,$$

where the first term is due to piezoelectric interaction and the second is via a deformation potential interaction. α in (1G.1) is the coupling constant, C_1 the deformation potential constant, ρ_d the density of the crystal and $\omega_q = \hbar s q$. $b_q^\dagger$ is the creation operator of the phonons.

A calculation similar to Appendix 1D gives the Green's function which has the same form as (1D.8), but with

$$\zeta = \frac{1}{\pi} \frac{V_d}{(2\pi l)^2} \left(\frac{2m^*}{\hbar^2}\right)^{1/2} W$$

$$W = C_1^2 \frac{\pi}{\rho_d V_0} \frac{k_B T}{s^2} + 0.36 \frac{\pi}{V_0} \frac{\alpha e^2}{\epsilon} (k_B T) l^2 .$$

(1G.2)

The above calculation is carried out for electrons in the quantum limit. The linewidth, given by (III.21)

$$\Gamma \simeq 7.1 \lambda \omega_s \zeta^{2/3}$$

is seen to be proportional to $T^{2/3}$.

However, for CdS, with its large effective mass, this limit is seldom satisfied. In general, several Landau levels are always occupied. Also, a rough esitmation of the collision rate in CdS by using (1G.2) shows that the rate is about four orders of magnitude larger than the collision rate in InSb. Thus the singularity peaks of the density of states are very well rounded off. Under these situations, we may approximate $\rho(\varepsilon)$ by the

free density of states in the absence of a magnetic field

$$\rho(\varepsilon) \ = \ \frac{V_{ol}}{(2\pi)^2} \left(\frac{2m^*}{\hbar^2}\right)^{3/2} \sqrt{\varepsilon} \qquad\qquad (1G.3)$$

The spectrum will be given by equation (III.20) with $\rho^{(\varepsilon)}$ given by (1G.3).

At low temperatures, the lineshape will be primarily determined by the two

Fermi factors. As temperature increases, the shape broadens until it is

finally limited by the density of states, which is zero for $\omega > \omega_s$.

Figure 1.16 gives the spectrum calculated at several temperatures, and their

linewidths are plotted in Figure 1.17. The width increases linearly with

temperature at low T, and less than linear for T goes higher. This depart

from linear dependence is caused by the density of states limitation.

Figure 1.17 shows that the theory does not compare favorably with

experiment,[26] especially at high temperatures. Also, experiment observed

lineshapes are Lorentzians centered at $\omega'=\omega_s$, while theoretical curves

show a shift given by

$$\lambda\omega_s \left(\varepsilon_F/\hbar - \omega_s\right) \ .$$

These discrepancies between experiments and theory need further investiga-

tion.

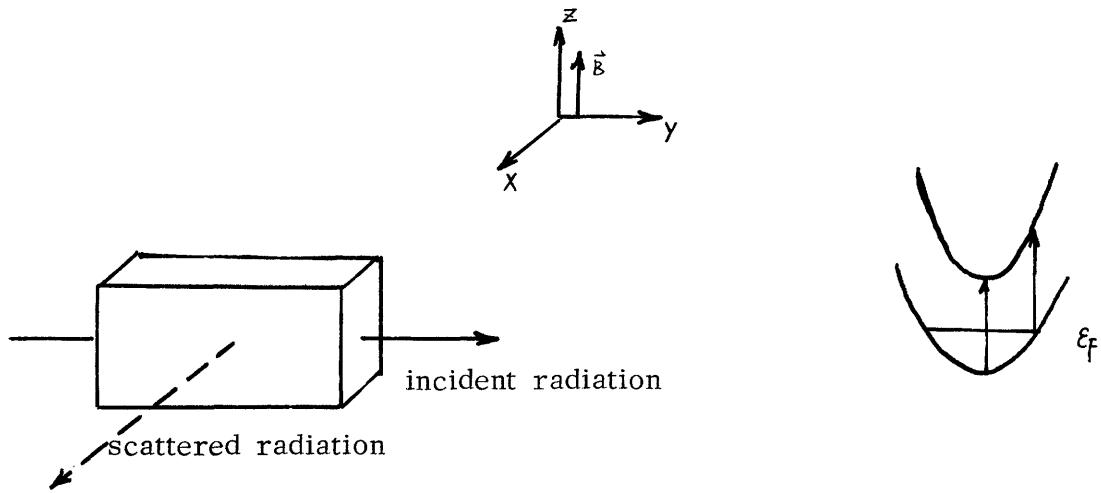Figure 1.1a $\vec{q}.\vec{B}=0$ geometry. Both the incident and scattered radiations propagate perpendicular to the magnetic field.
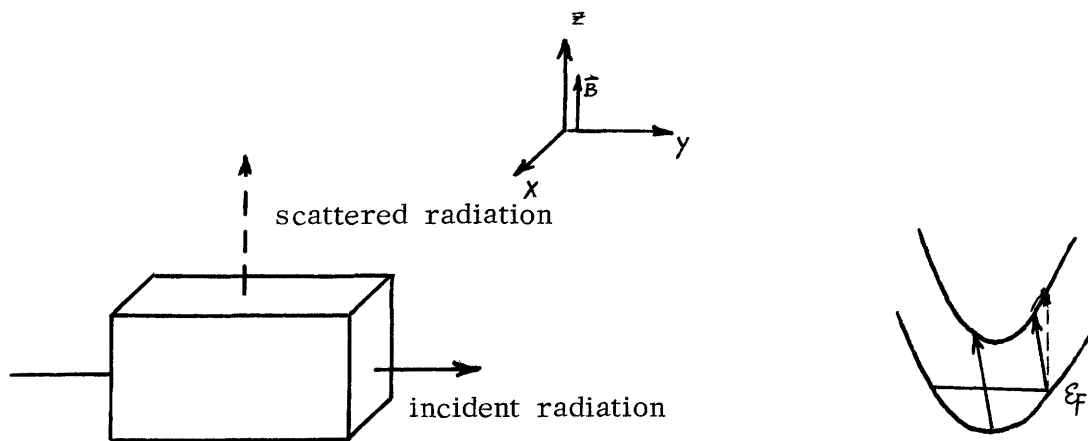

Figure 1.1b $\vec{q}.\vec{B}\neq 0$ geometry. The scattered radiation propagates parallel to the magetic field
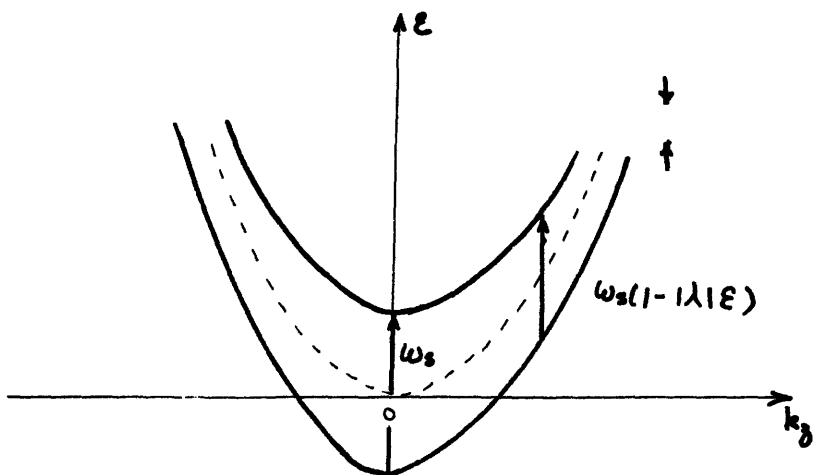
Figure 1.2a   InSb band model used in lineshape calculation. $\vec{q}.\vec{B} = 0$
geometry.

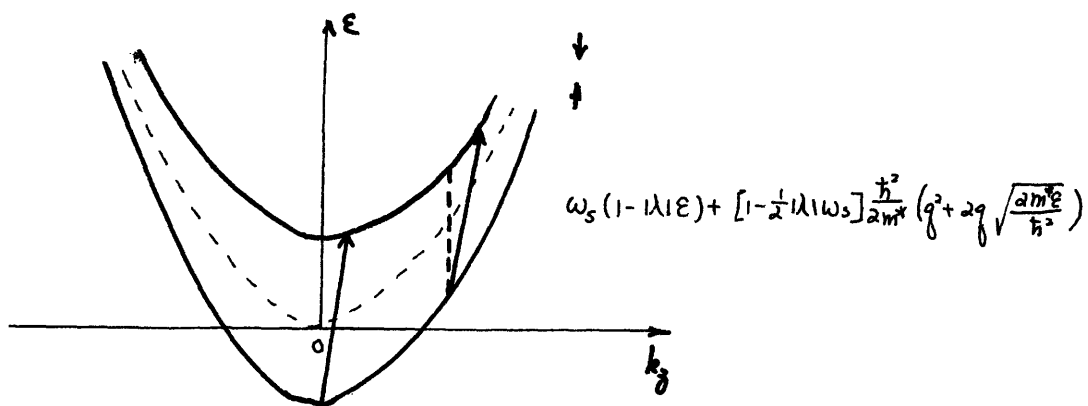
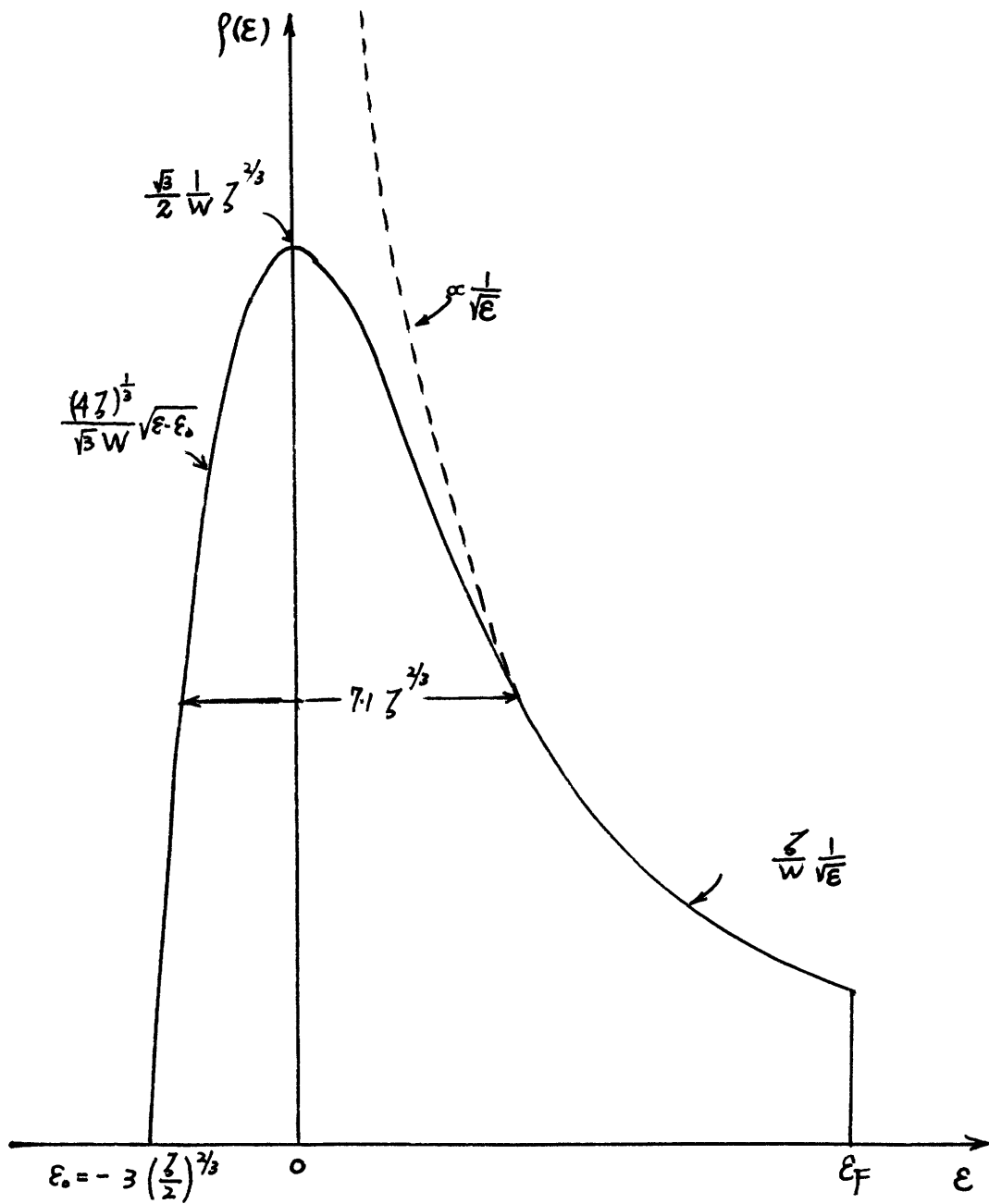Figure 1.2b   InSb band model used in lineshape calculation. $\vec{q}.\vec{B} \neq 0$
geometry

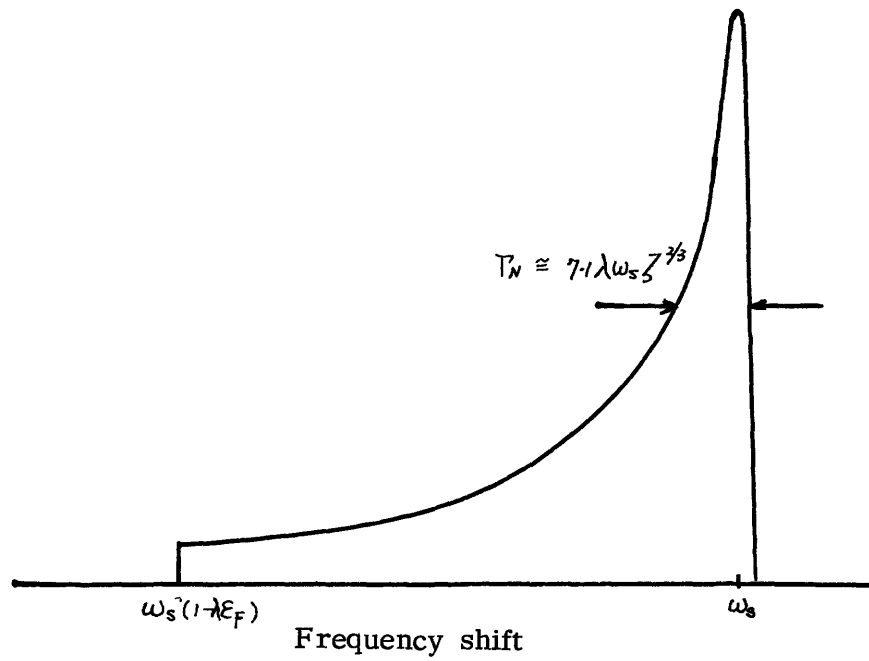Figure 1.3   Collision broadened magnetic density of state .

$$T_N \cong 7.1 \lambda \omega_s \zeta^{2/3}$$

$\omega_s'(1-\lambda \mathcal{E}_F)$ ω_s

Frequency shift

Figure 1.4a Nonparabolicity dominated lineshape in the extremely strong field limit. $\mathcal{E}_F < \hbar \omega_s$.   T=0. $\vec{q}.\vec{B}$=0 geometry

$$T_N \cong \lambda \omega_s \hbar \omega_s$$

$\omega_s(1-\lambda \mathcal{E}_F)$ $\omega_s \left\{ 1 - \lambda (\mathcal{E}_F - \hbar \omega_s) \right\}$ ω_s

Frequency shift

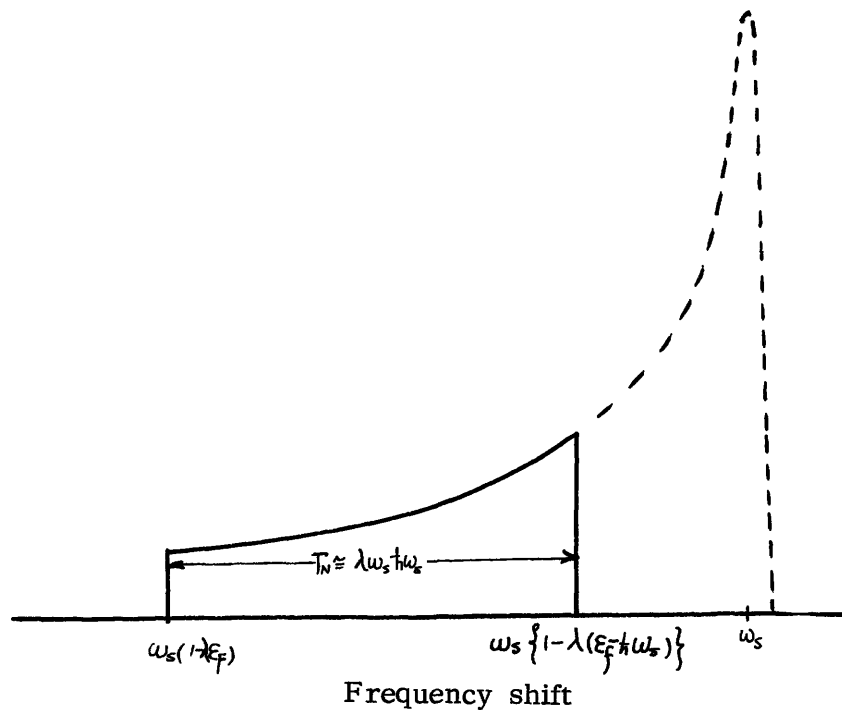Figure 1.4b Nonparabolicity dominated lineshape for $\hbar \omega_c > \mathcal{E}_F > \hbar \omega_s$. $T = 0\,°K$.
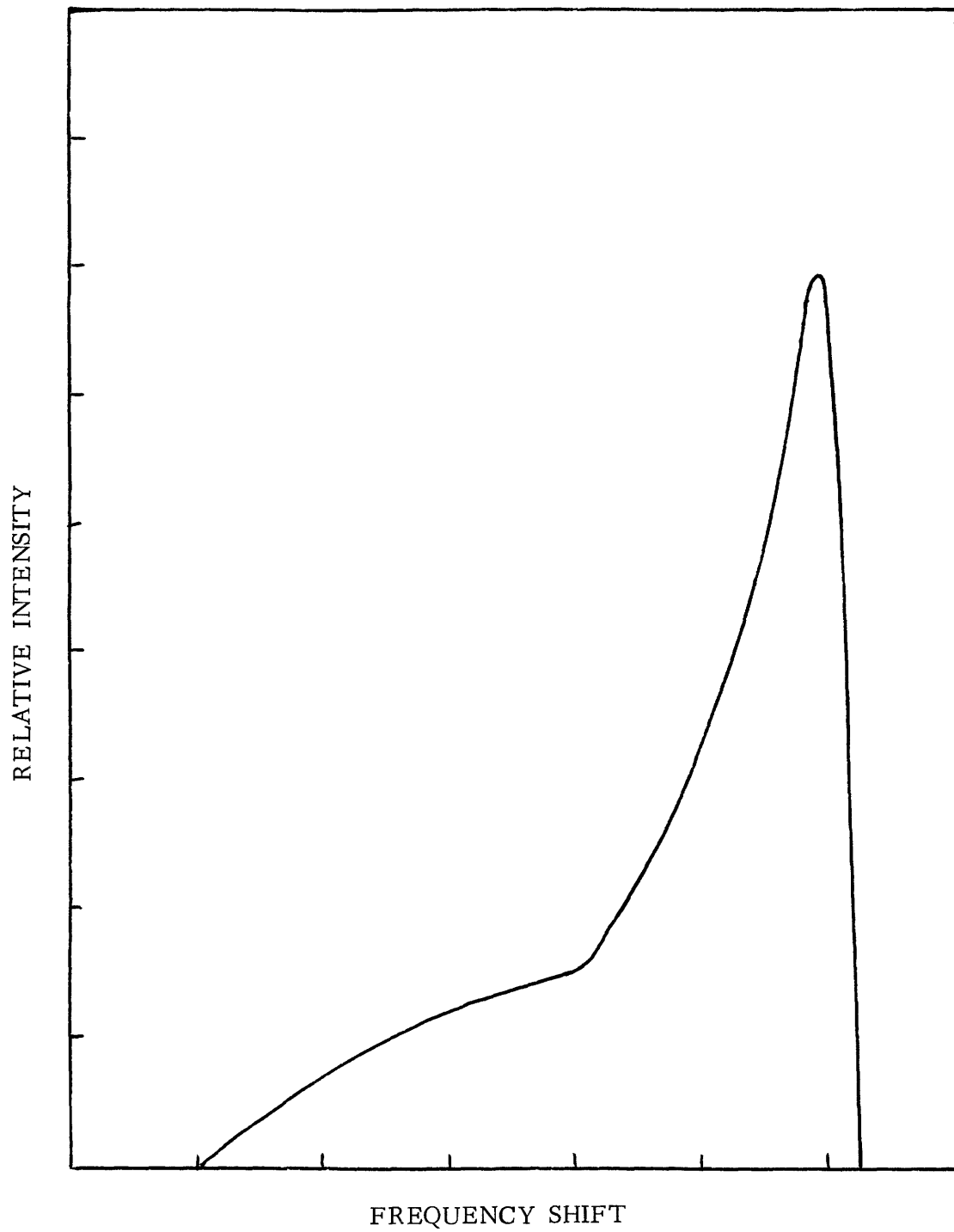
Figure 1.5   Nonparabolicity dominated lineshape for $\vec{q} \cdot \vec{B} \neq 0$ geometry .
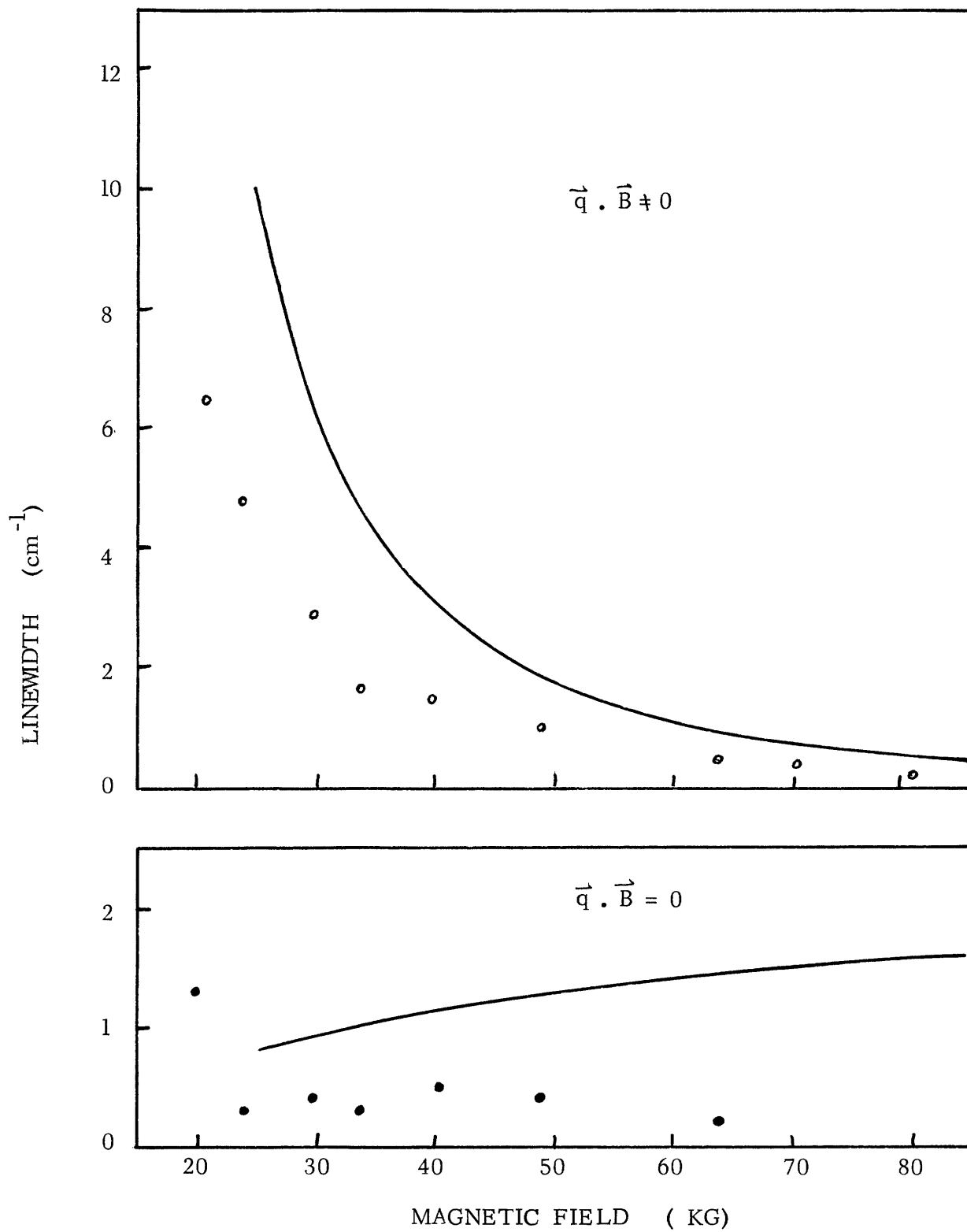
Figure 1.6   Comparison of the calculated linewidths with experiment.
N=1.0x10^{16} cm^{-3}.   T=2°K.
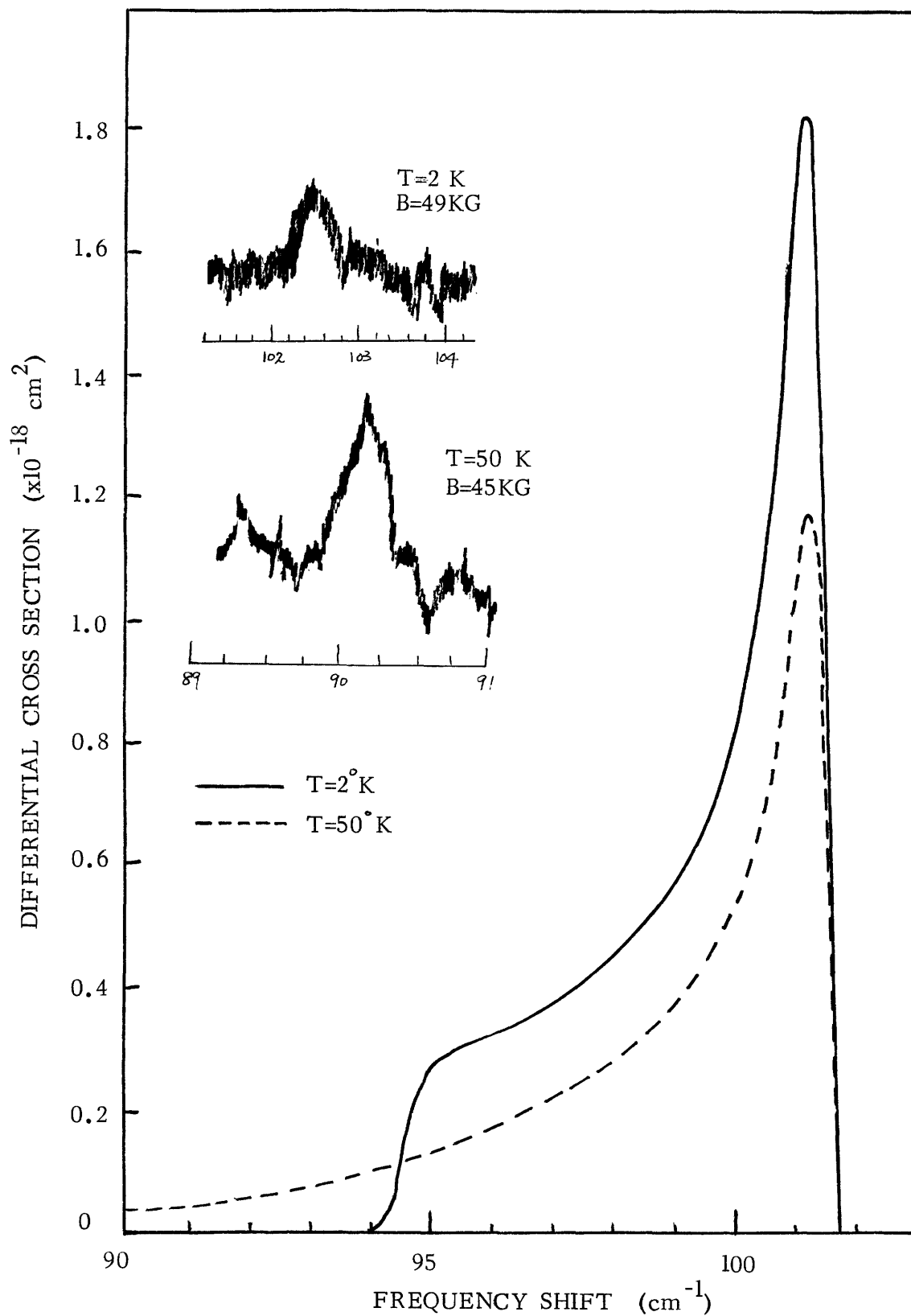
Figure 1.7 Comparison of theoretically predicted spectrum with experiment. $\vec{q}.\vec{B}=0$ geometry. N=1.0x10^{16} cm^{-3} . B=49KG.
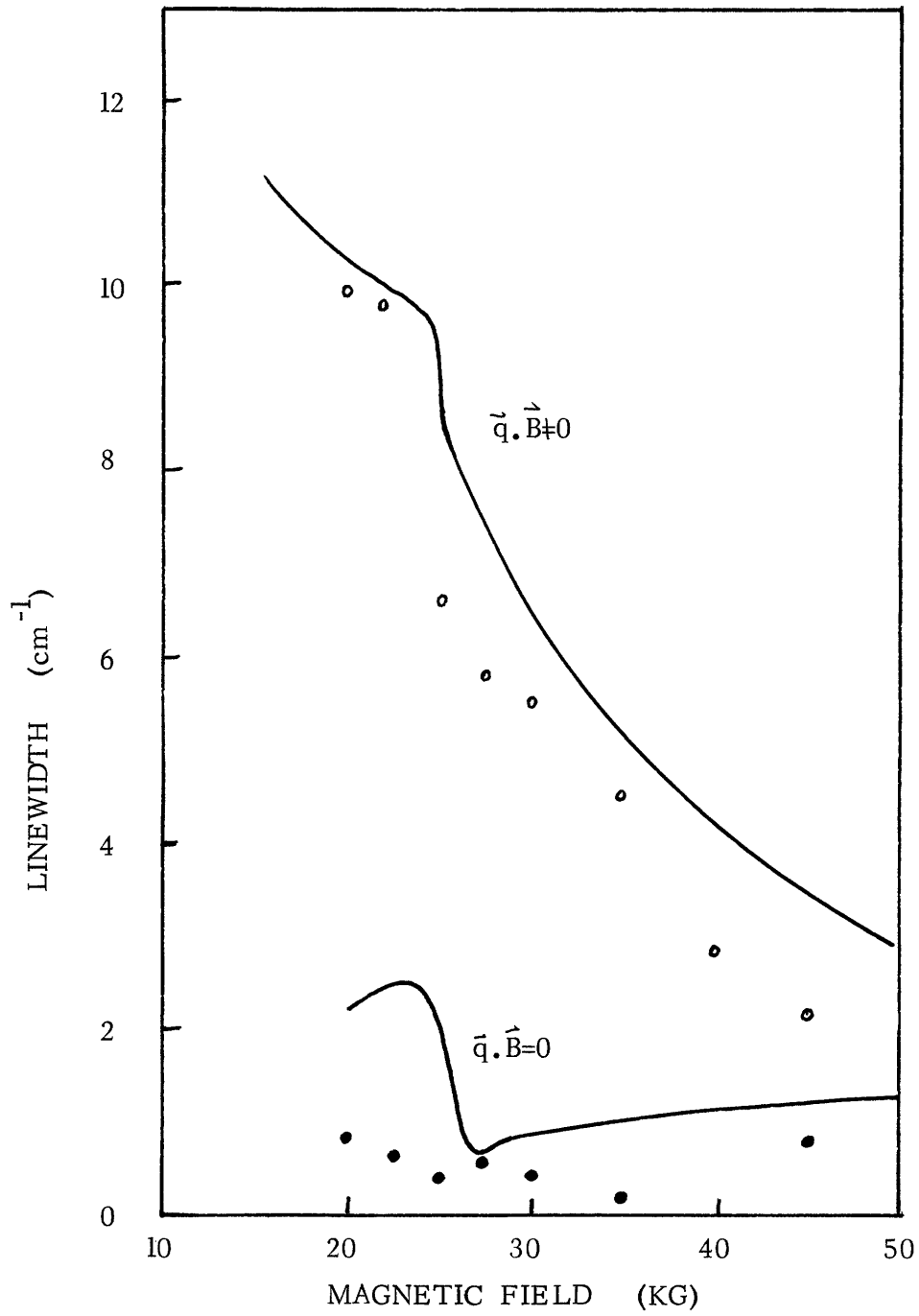
Figure 1.8 Comparison of calculated linewidths with experiment.
N=1.0x10^{16} cm^{-3}.   T=50°K.
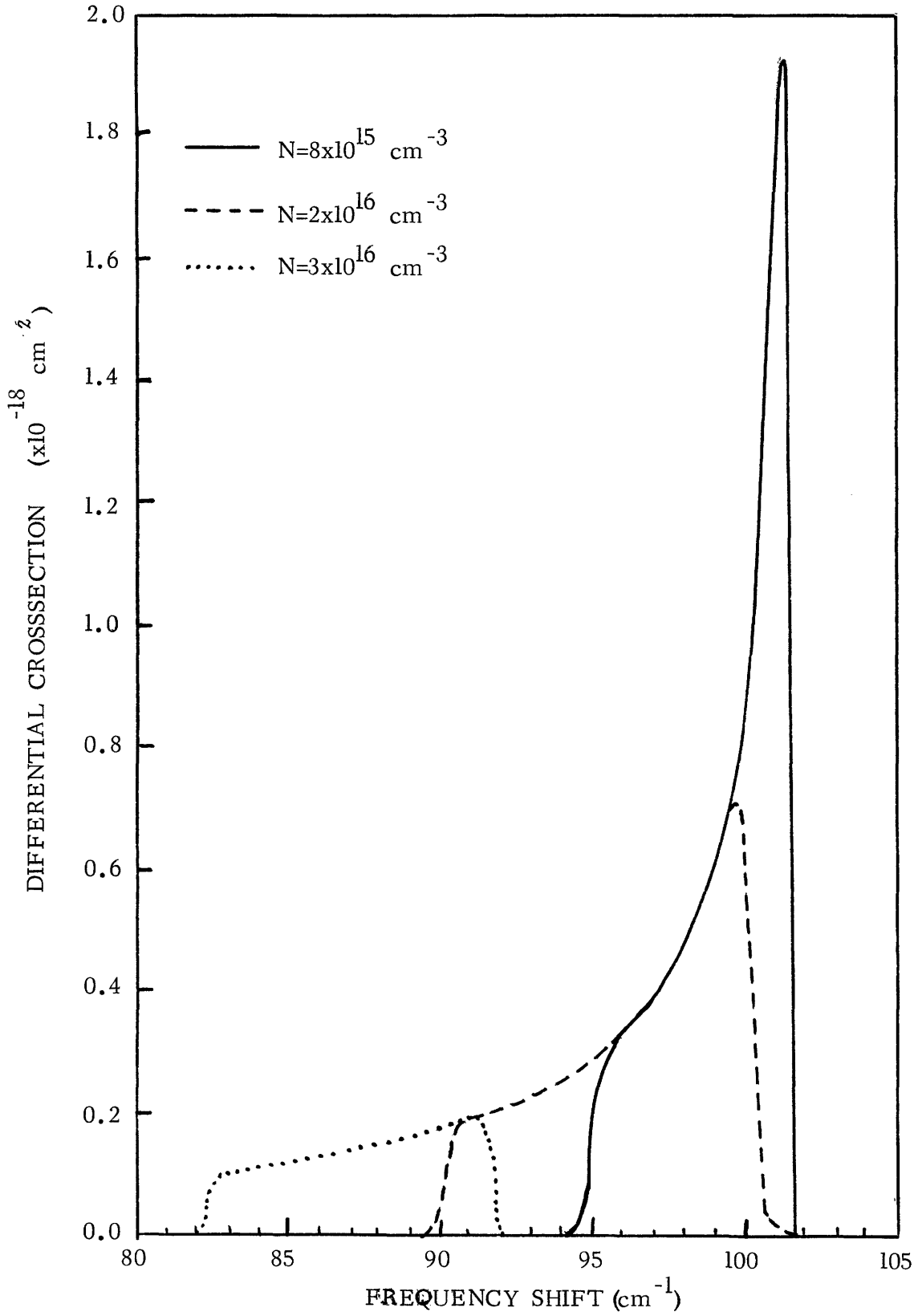
Figure 1.9 NOnparabolicity Dominated lineshape for several carrier concentrations. T=2°K. B=49 KG.
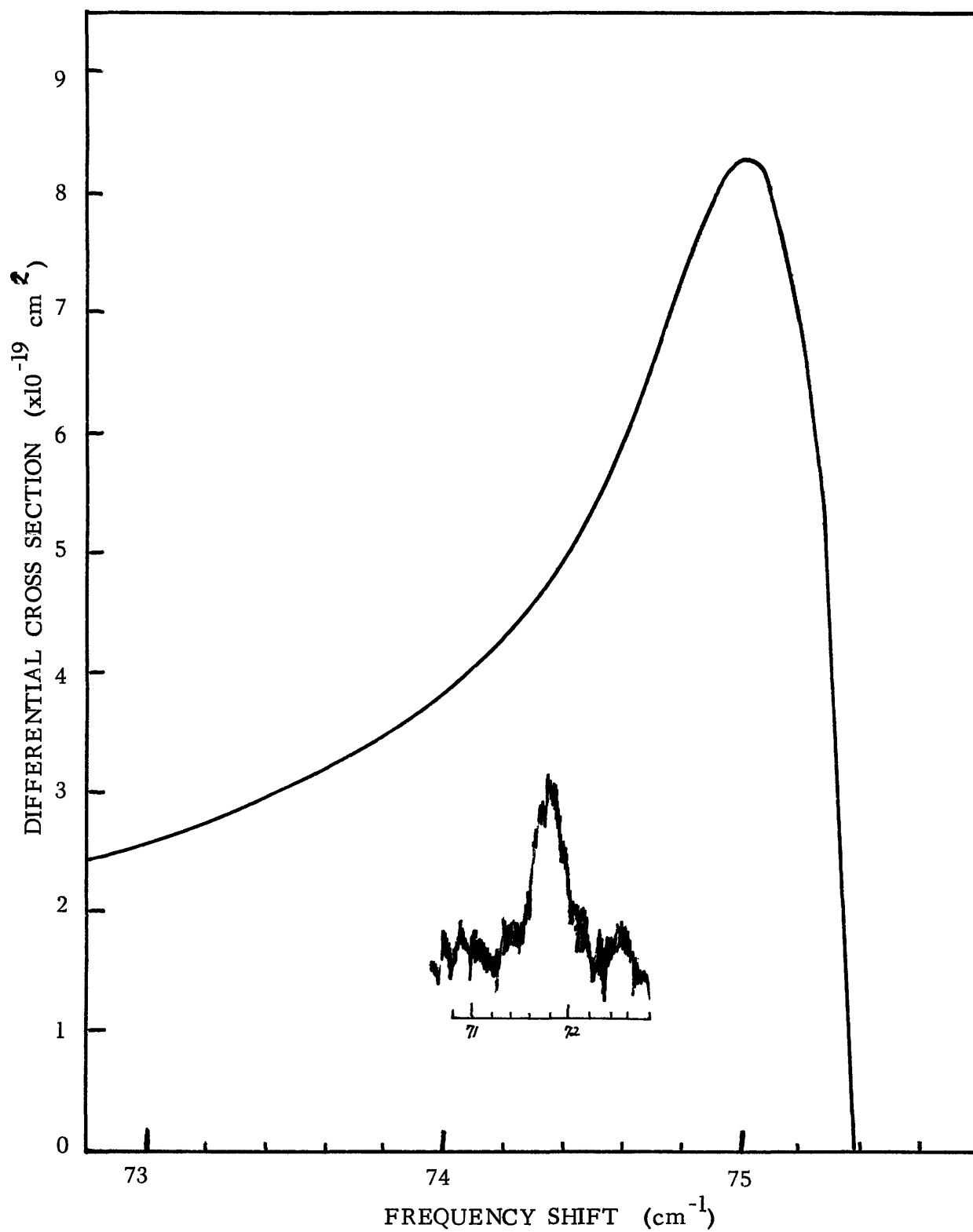
Figure 1.10   Comparison of calculated spectrum with experiment for $\vec{q}.\vec{B}=0$ geometry. $N=10^{16}$ cm^{-3}.   T=50°K.   B=35 KG.
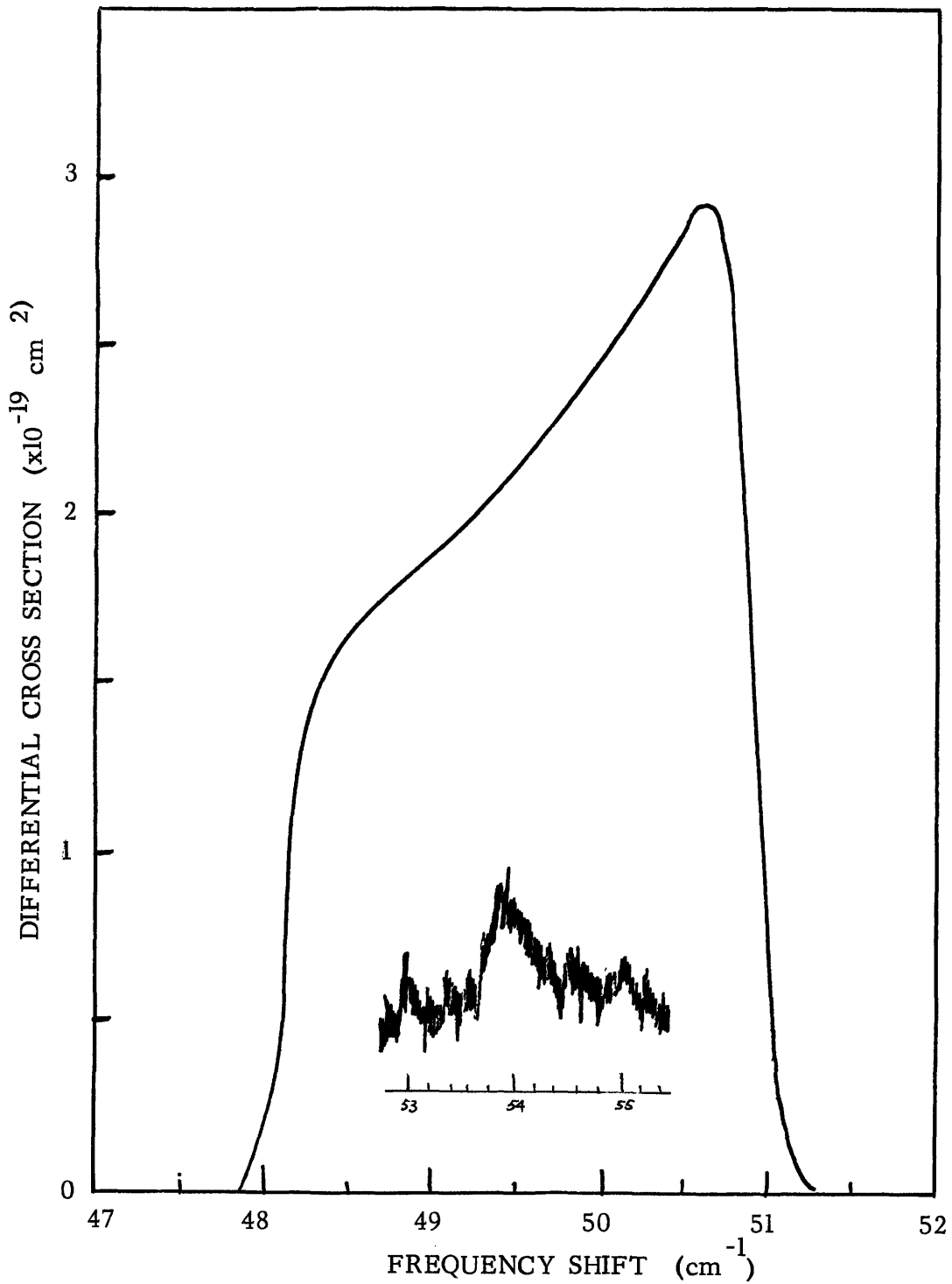
Figure 1.11 Comparison of calculated spectrum with experiment for $\vec{q}.\vec{B}=0$ geometry. $N=10^{16}$ cm^{-3}. T=$2°$ K. B=24 KG.
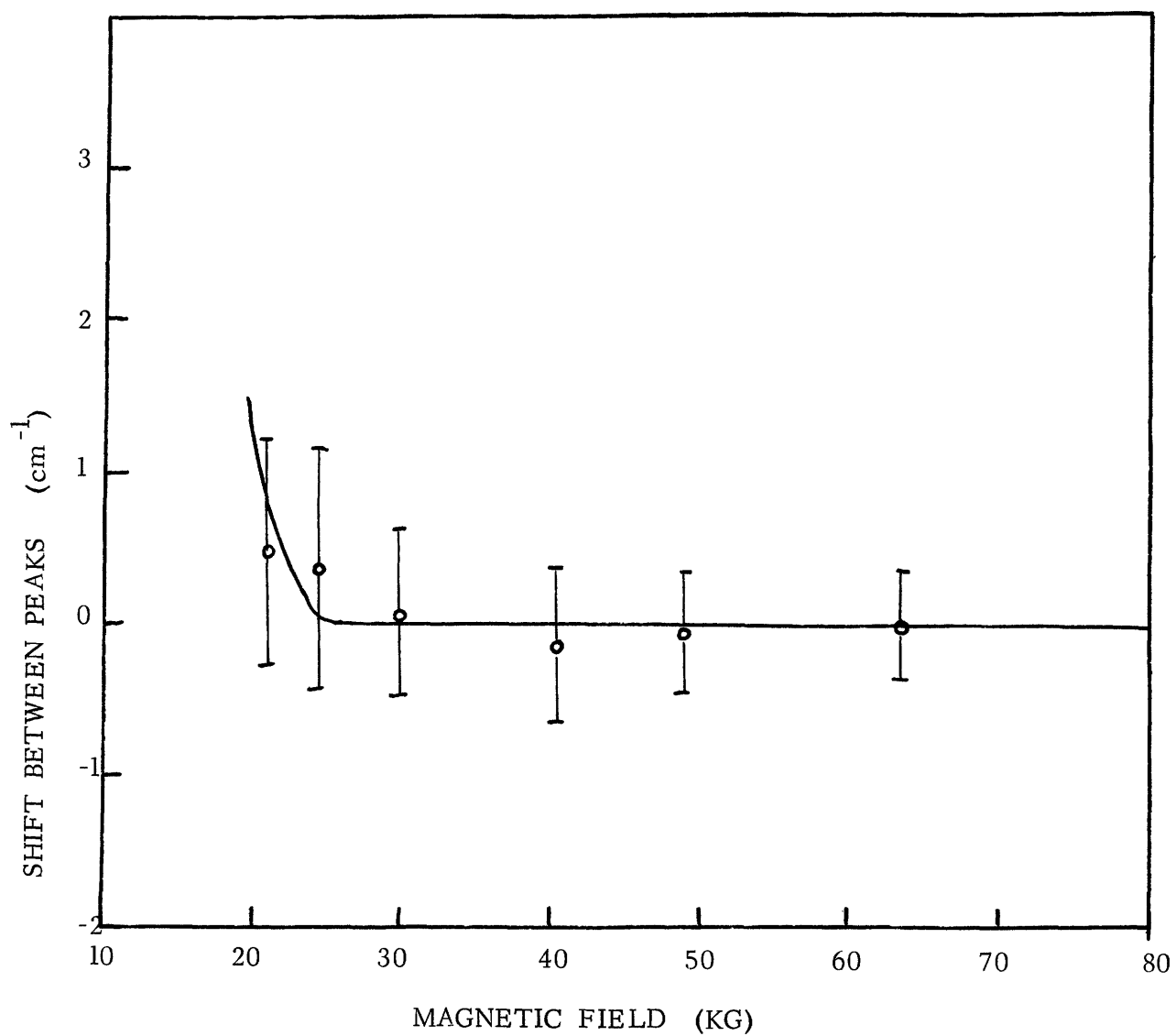
Figure 1.12   Comparison between theory and experiment for the peak separation of the lineshapes in the two geometries. $N=10^{16}$ cm^{-3}. $T=2°K$.
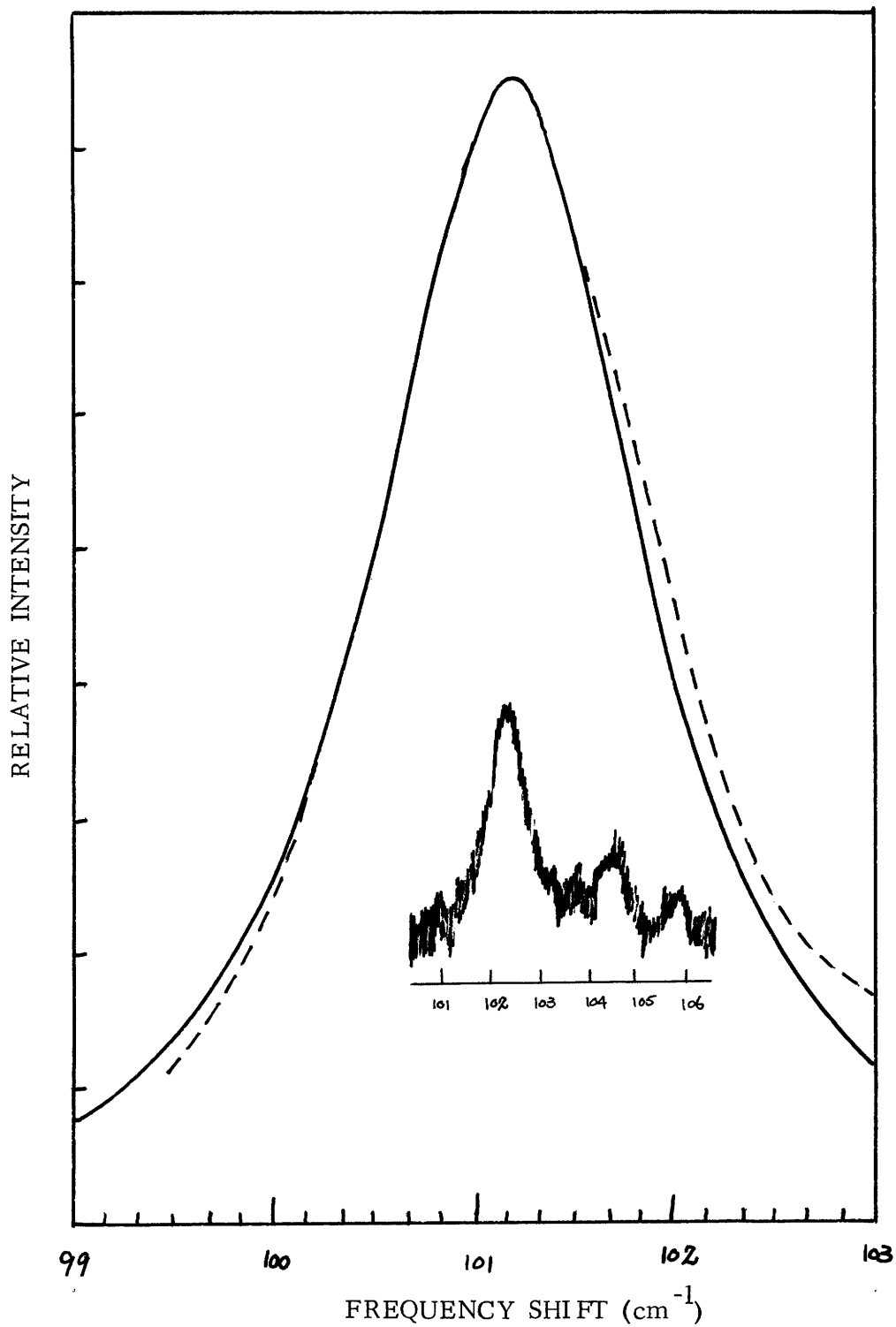
Figure 1.13 Comparison of the calculated lineshape with experiment for q.B ≠ 0 geometry. $N=10^{16}$ cm^{-3}. B=49 KG. $T=2°K$. The solid line is calculated with a constant γ_0 , and the broken line with equation (V.1).
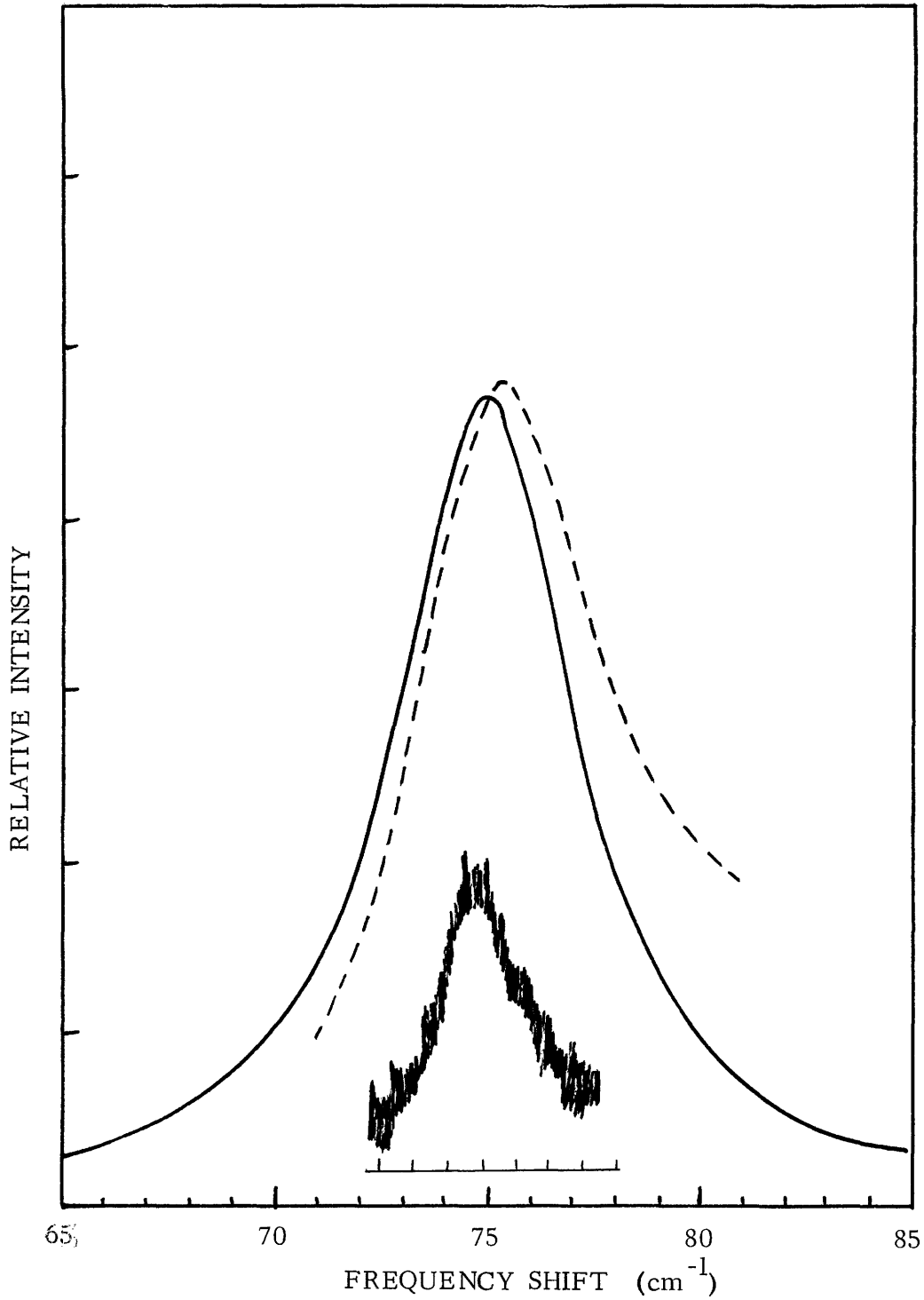
Figure 1.14   Comparison of the calculated spectrum with experiment for q.B ≠ 0 geometry. $N=10^{16}$ cm^{-3}.   B=35 KG.   T=50°K.   The solid line is calculated with a constant γ_o , and the broken line with equation (V.1).
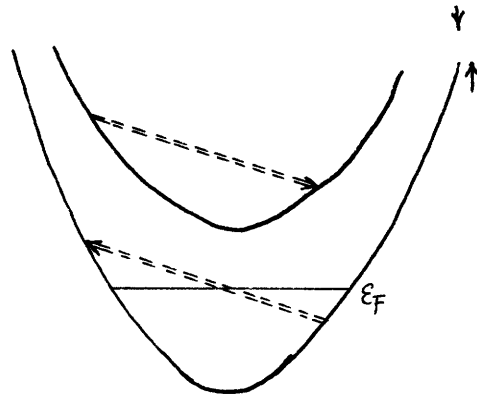
Figure 1.15a   Electron-electron collisions.
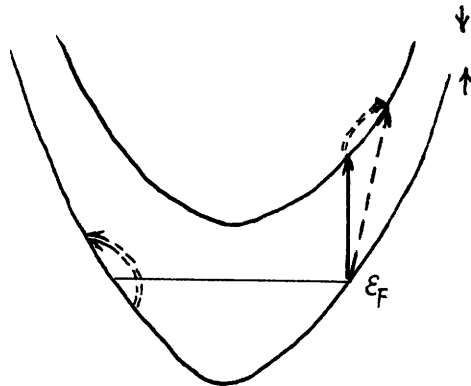
Figure 1.15b   "Auger effects."
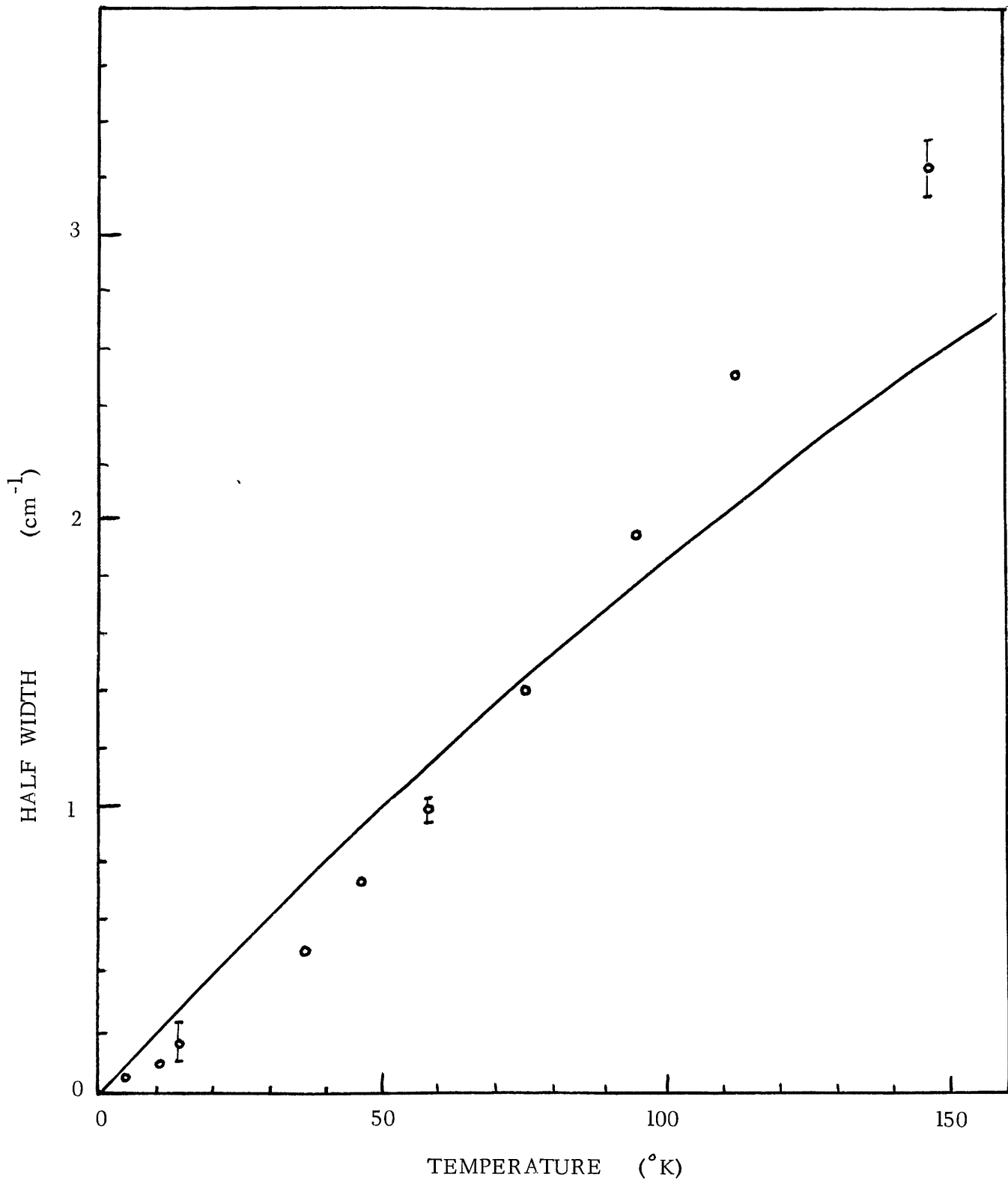
Figure 1.16   Comparison of the calculated linewidths with experiment for
scattering from n-CdS. $N=5\times10^{17}$ cm^{-3}.   B=57 KG.
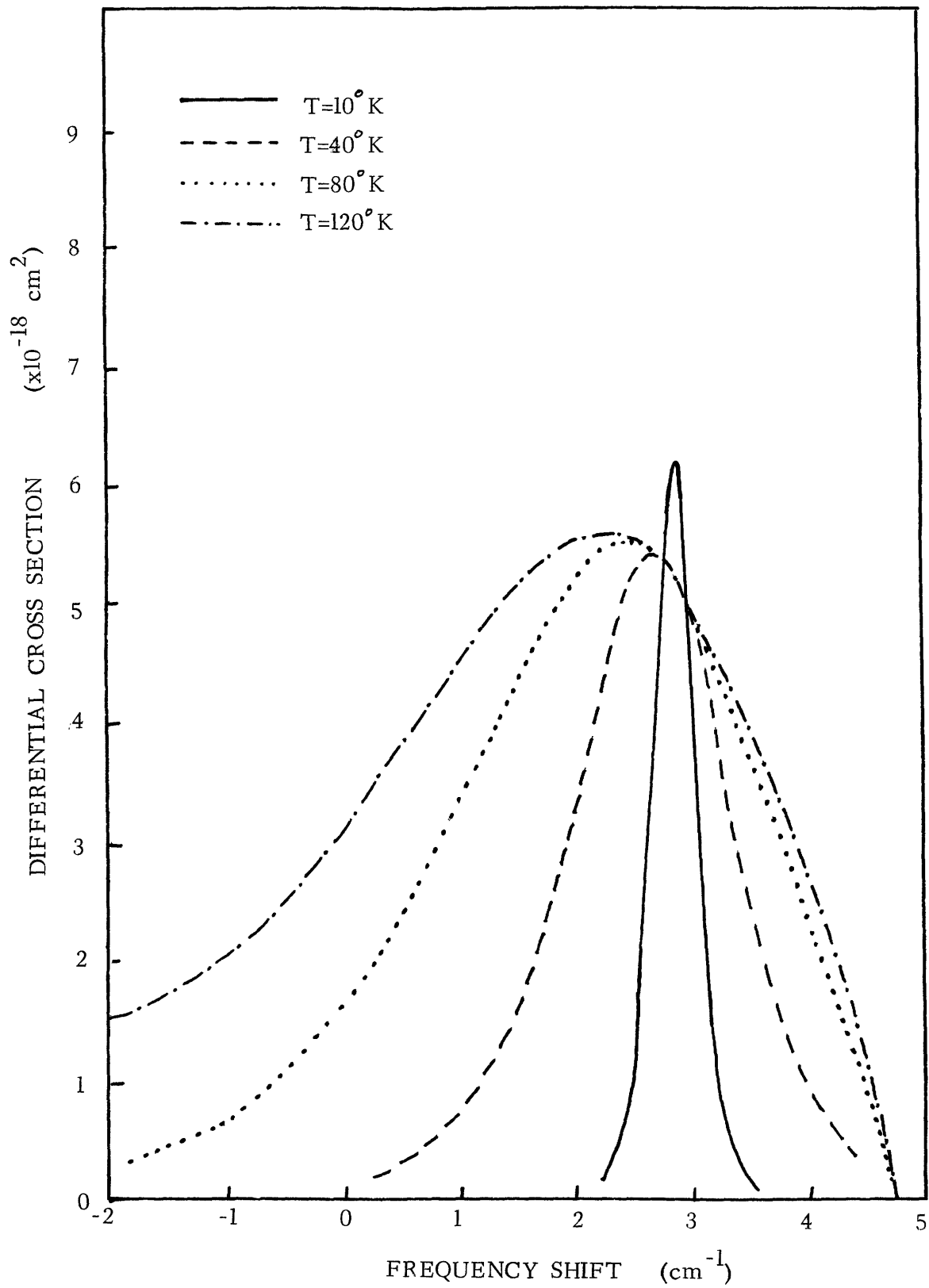
Figure 1.17 Theoretical calculated lineshapes for scattering from n-CdS. $N=5\times10^{17}$ cm^{-3}. B=50 KG.

REFERENCES

(1)   S.R.J. Brueck, Ph.D. thesis submitted to the Department of Electrical
        Engineering, M.I.T., Cambridge, Mass., August, 1971

(2)   R. Brout, Phys. Rev. 107, 664 (1957)

(3)   Y. Yafet, in Solid State Physics, Vol. 14, Ed. by F. Seitz and D. Turnball,
        Academic Press, New York, 1963

(4)   G. Bemski, Phys. Rev. Lett. 4, 62 (1960); R.A. Issacson, Phys. Rev. 169,
        312 (1968); J. Konopka, Phys. Rev. Lett. 24, 666, (1970); B.D. McCombe
        and R.J. Wagner, Phys. Rev. B4, 1285 (1971)

(5)   R.E. Slusher, C.K.N. Patel and P.A. Fleury, Phys. Rev. Lett. 18,
        530 (1967); C.K.N. Patel and E.D. Shaw, Phys. Rev. B3, 1297, (1971)

(6)   P.A. Fleury and J.F. Scott, Phys. Rev. B3, 1979 (1971)

(7)   B. Lax and J.G. Mavroides, in Solid State Physics, Vol. II, ed. by
        F. Seitz and D. Turnbull, Academic Press, 1960

(8)   F.A. Blum, Phys. Rev. B1, 1125, (1970); D.C. Hamilton and A.L.
        McWhorter, in Light Scattering Spectra of Solids, ed. by G.B. Wright,
        Springer-Verlag, New York, 1969

(9)   L. van Hove, Physica, 21, 901 (1953)

(10)   R. Kubo, S.J. Miyake and N. Hashitsume, in Solid State Physics, Vol. 17,
        ed. by F. Seitz and D. Turnbull, Academic Press, New York, 1965

(11)   Y. Yafet, Phys. Rev., 152, 858 (1966)

(12)   P.A. Wolff, Phys. Rev. Lett., 16, 225 (1966)

(13)   See, for example, W. Louisell, Radiation and Noise in Quantum Electronics,
        McGraw-Hill Co., New York, 1964

(14) R.M. Morse and H. Feshback, <u>Methods of Theoretical Physics,</u> Vol. 1

McGraw-Hill Co., New York, 1953

(15) D. Pines, <u>Elementary Excitation in Solids,</u> Benjamin Inc., New York, 1964

(16) See, for example, G. Dresselhause and M.S. Dresselhause, in <u>The</u>

<u>Optical Properties of Solids,</u> ed. by J. Tauc, Academic Press, 1966

(17) D. Pines and P. Nozieres, <u>The Theory of Quantum Liquids,</u> Benjamin

Inc., New York, 1966

(18) H.J. Hrostowski, et al. Phys. Rev. <u>100,</u> 1672 (1955)

(19) H. Halpern and M. Lax (private communication)

(20) P. Argyres, Phys. Rev. <u>132,</u> 1527 (1963)

(22) See, for example, C. Kittel, <u>Quantum Theory of Solids,</u> John Wiley and

Son Co., New York, 1963

(23) W. Kohn and J.M. Luttinger, Phys. Rev. <u>108,</u> 590 (1958)

(24) Celli and Mermin, Phys. Rev. <u>140,</u> A839 (1965)

(25) S.S. Schweber, <u>An Introduction to Relativistic Quantum Field Theory,</u>

Harper and Row, New York, 1961

(26) P.A. Fleury (private communication)

CHAPTER 2

THEORY OF TRAVELING WAVE ELECTRONIC

RAMAN LASERS.   STEADY STATE BEHAVIOR

I. INTRODUCTION

A great deal of experiment and theoretical effort has been

recently devoted to the phenomenon of stimulated Raman scattering

(SRS), partly because it is a potent mechanism for obtaining coherent

optical radiation in many frequency ranges. In particular, the theory

of SRS has been discussed by many authors from various points of view.

Nonlinear effects important in a proper description of SRS in many systems

have also received extensive attention.[1] It can be fairly asserted that the

phenomenon of SRS is qualitatively well understood.

No detailed explanation or quantitative understanding, however,

have been given to many features of the experimental observations. For

example, the saturation of the steady state (sinusoidal steady state,

stationary state) Stokes output power at high pump power level has not

received a quantitative description. Also no formula has been given for

the steady state output power as a function of the system parameters.

This information will be useful to those interested in adjusting or maximizing

their power output. More important is the problem of a proper treatment

of the laser pump power depletion effect. This effect is important when the

conversion efficiency of SRS is high, and can lead to unphysical results when

neglected. Although SRS theory has been considered for both scattering from

collective and single particle excitations, the usual detailed theory [2]-[3]

is restricted to the description of scattering from collective modes[#]. One needs

more variables than the collective case in a detailed explicit description of

scattering from multi-level single particle excitations.

With the development of the tunable spin-flip Raman (SFR) [4]

laser based on scattering from electronic spin-sublevels in semi-conductors,

single-particle SRS processes have acquired new importance. Much work has

now been reported on the SFR laser and its applications.[5]-[7] The SFR laser

is interesting in many ways. It constitutes the first cw operation of a Raman

laser, and provides high power tunable infrared radiation. Its gain of

1×10^{-5} cm^{-1} /W-cm^{-2} is the largest Raman gain known to date in any portion

of the spectrum, and should be compared with the gain for Raman scattering in

CS_2 at 5000 $\overset{o}{A}$. It can have very high conversion efficiency and very low

threshold power. The electronic Raman laser is also interesting in other

regards. It can be considered as a generalization of ordinary multi-level

lasers with a different pumping mechanism. Since nonlinear effects like self-

focusing are expected to be unimportant in semiconductors, it also provides a

good testing ground for the general theory of Raman lasers. It appears at

---

The nonlinear susceptibility is however frequently calculated through a multi-
level molecular system.

present that a detailed theory of electronic Raman laser is worth considering, which takes special account of the multi-level nature of the scattering excitations.

In this paper we construct a relatively complete description of the electronic Raman laser. A hamiltonian is developed to describe the scattering processes and the laser system. Together with added loss terms, ten coupled equations of motion are then derived describing the average behavior of the pump laser radiation, the Stokes radiation, and anti-Stokes (AS) radiation, and the two-level electronic system. Steady-state solutions of these ten equations are obtained. Among the results obtained we have analytic expressions for the Stokes and anti-Stokes output powers, including their saturation behavior at large pump power. Interesting insight and useful conclusions on the laser behavior can be drawn from these formulas.

We have also given a novel treatment of the pump depletion effect. When pump depletion is neglected one may run into answers for which the Stokes power is larger than the pump power. Proper account for the pump depletion is also important in obtaining steady state power expressions for Raman lasers operating by scattering from collective modes. We will not discuss the collective case in this paper. A detailed comparis.on of output power behavior for the collective and single-particle Raman cases as well as other lasing mechanisms will be reported elsewhere.

In section II we discuss the development of quantum mechanical hamiltonian densities that describe our single particle scattering processes. Its relation to

the usual treatment by nonlinear susceptibility is indicated. The equations of motion for the averaged fields and the electron densities are derived in section III. The equations are solved in the steady state in section IV, where we also give a detailed description of the phase matching behavior. In section V we develop a proper treatment of pump depletion. This treatment allows us to solve the problem of boundary condition excitation in a simple manner. In section VI we discuss the detailed steady state behavior of our system in a specific case, and interprete our results physically. The limiting cases of no AS radiation is discussed in section VII, where we also indicate the difference of our system from an ordinary laser and other Raman lasers. A brief comparison with experiments is given in section VIII. Some discussions of the nature of our results are given in section IX and a few concluding remarks in section X.

Because the other optical nonlinearities are not important in the SFR laser,[10] our results are in excellent agreement with experiments. This probably constitutes the first detailed confirmation between Raman laser theory and experimental observations.

II. FORMULATION

Consider a collection of identical multi-level subsystems, each subsystem can be a molecule, an atom or an electron. For definiteness we regard the subsystem to be an electron, with levels 1 and 2 among others as indicated in Figure 2.1a. The collection of electrons is supposed to span a volume V which

we refer to as the crystal. The energy difference between levels 1 and 2 of an electron is denoted by

$$\hbar\omega_e = \hbar\omega_2 - \hbar\omega_1 \tag{II.1}$$

A Raman process involving the two levels may occur in the following way. A photon of energy $\hbar\omega_p$ is incident on the electronic system, and is scattered by one of the electrons with initial state 1 and final state 2. The scattered photon has energy

$$\hbar\omega_s = \hbar\omega_p - \hbar\omega_e \tag{II.2}$$

This process is depicted in Figure 2.1b. Other Raman processes involving virtual transitions between the electron states can, however, also occur. As indicated in Figure 2.1c an electron can be scattered from level 1 to 2 via an intermediate state, although the scattered energy is still given by (II.2). Similar process of higher order with the same scattered energy can clearly happen, corresponding to transitions described by an n-th order perturbation theory expression.

A first principle description of the entire system will, therefore, have to consider all relevent levels of the electrons explicitly. Such a procedure is always unduly complicated, and the common strategy is to retain only the initial and final states, in our case 1 and 2, and eliminate the other intermediate states through an effective parameter. Thus in this case we introduce a phenomeno-logical effective hamiltonian

$$H_I \sim \mu_s' \left(b_s^\dagger b_p \, a_1 \, a_2^\dagger + b_s \, b_p^\dagger \, a_1^\dagger a_2 \right)$$ (II.3)

to describe the scattering, regardless of the virtual transitions the electrons may go through. In (II.3) we use b_s and b_p to denote the photon annihilation operator of the Stokes and pump field, a_1 and a_2 to denote the annihilation operators for electronic levels 1 and 2 respectively. The effective parameter μ_s' can be determined from transition probability consideration. Thus we have replaced an n-th order process by an effective first order one.

The presence of anti-Stokes (AS) radiation, when the electrons are more populated in the lower level 1, is due to the coherent interaction of two pump photons with the electronic system as shown in Figure 2.2. The interaction hamiltonian can be written in this case

$$H_I \sim \mu_s' (b_s^\dagger b_p a_1 \, a_2^\dagger + b_s b_p^\dagger a_1^\dagger a_2)$$ (II.4)

$$+ \mu_a' (b_a^\dagger b_p a_1^\dagger a_2 + b_a b_p^\dagger a_1 a_2^\dagger) \quad .$$

It is important to note that stimulated AS radiation does not occur as a Raman process similar to Stokes generation, despite the appearance of the second term in (II.4) similar to (II.3). This is because without a population inversion, such stimulated process cannot occur. The production of AS waves is a four-photon parametric process, so that generation of an AS photon is always accompanied by a Stokes photon. On the contrary, Stokes photons can be generated alone in the Raman process of Figure 2.1. Thus we see that the Stokes output power is always greater than the anti-Stokes one. When a population inversion

exists in the electronic system, stimulated AS radiation can then occur as an ordinary Raman process, whereas stimulated Raman scattering is likewise impossible at the Stokes frequency. Coherent two-photon conversion can, of course, again occur.

We will formulate our problem quantum mechanically before we obtain the classical equations for the quantum average quantities. The reason for doing this is due to the non-classical nature of the multi-level systems, which lend themselves more naturally to a quantum description. Moreover, our quantum formulation will be used in subsequent papers.

Consider the hamiltonian for each electron

$$H_i = \hbar\omega_2 a_{2i}^\dagger a_{2i} + \hbar\omega_1 a_{1i}^\dagger a_{1i} \tag{II.5}$$

for a total number of N electrons per unit volume. We define

$$M \triangleq \sum_i a_{1i}^\dagger a_{2i}$$

$$M^+ \triangleq \sum_i a_{1i} a_{2i}^\dagger \tag{II.6}$$

$$N_1 \triangleq \sum_i a_{1i}^\dagger a_{1i}$$

$$N_2 \triangleq \sum_i a_{2i}^\dagger a_{2i} \tag{II.7}$$

$$N_1 - N_2 \triangleq D$$

$$N_1 + N_2 \triangleq S .$$

<div align="right">(II.8)</div>

Note that the different electrons are independent. The statistics of electrons are taken into account in the spontaneous linewidth Γ , which is calculated in Chapter 1. The operator M describes the polarization of the electron system. A detailed discussion of the operator algebra and commutation rules of the electronic operators can be found elsewhere.[11] We just note here the following commutators:

$$[M, M^\dagger] = D$$

$$[N_1, M] = M$$

$$[N_2, M] = -M$$

<div align="right">(II.9)</div>

$$[N_1, N_2] = 0 .$$

The electronic and radiation variables are, of course, always commutative.

We introduce the following spatially dependent electron density variables

$$O(t) = \int O(\vec{r}, t) \, d\vec{r}$$

$$O(\vec{r}, t) = \sum_{i=1}^{N} O_i \, \delta(\vec{r} - \vec{r_i}) ,$$

<div align="right">(II.10)</div>

where $\mathcal{O} = M, M^{\dagger}, N_1, N_2$. From (II.9) these variables obey the commutation rules

$$\left[\mathcal{M}(\vec{r},t), \ \mathcal{M}^{\dagger}(\vec{r}',t) \right] = \mathcal{D}(\vec{r},t) \, \delta(\vec{r}-\vec{r}')$$

$$\left[\mathcal{N}_1(\vec{r},t), \ \mathcal{M}(\vec{r}',t) \right] = \mathcal{M}(\vec{r},t) \, \delta(\vec{r}-\vec{r}')$$

$$\left[\mathcal{N}_2(\vec{r},t), \ \mathcal{M}(\vec{r}',t) \right] = - \mathcal{M}(\vec{r},t) \, \delta(\vec{r}-\vec{r}')$$

(II.11)

$$\left[\mathcal{N}_1(\vec{r},t), \ \mathcal{N}_2(\vec{r}',t) \right] = 0 \quad .$$

The electronic hamiltonian is given by

$$H_e = \hbar\omega_1 \, N_1 + \hbar\omega_2 \, N_2$$

$$= \int \mathcal{H}_e (\vec{r},t) \, d\vec{r}$$

(II.12)

$$= \int \left[\hbar\omega_1 \, \mathcal{N}_1(\vec{r},t) + \hbar\omega_2 \, \mathcal{N}_2(\vec{r},t) \right] d\vec{r} \quad .$$

We next consider the electromagnetic fields interacting with the electronic system. Their electric field vectors are denoted by $\vec{E}_p(\vec{r},t)$, $\vec{E}_s(\vec{r},t)$ and $\vec{E}_a(\vec{r},t)$, which are quantum operators corresponding to the pump, the Stokes and the AS radiation. For simplicity we have neglected in this paper coupling to higher order Stokes and AS modes. [2]-[3] Backward waves [12] are also neglected. However, the fields may have arbitrary polarizations $\hat{l}_i$ and directions of propagations $\hat{k}_i$. We decouple each field operator into its

positive and negative frequency parts

$$\vec{E}_i(\vec{r},t) = \left\{ \mathbb{E}_i^{(+)}(\vec{r},t) + \mathbb{E}_i^{(-)}(\vec{r},t) \right\} \hat{l}_i \ , \qquad i = p, s, a \ , \qquad \text{(II.13)}$$

$$\left\{ \mathbb{E}_i^{(+)}(\vec{r},t) \right\}^{\dagger} = \mathbb{E}_i^{(-)}(\vec{r},t) \ , \qquad \text{(II.14)}$$

where $\mathbb{E}_i^{(-)}$ corresponds to a photon creation operator. We assume that the fields are essentially single mode so that

$$\mathbb{E}_i^{(+)}(\vec{r},t) \overset{\triangle}{=} \sqrt{\frac{\hbar \omega_i}{2 n_i^2}} \ \mathcal{E}_i(\vec{r},t) \qquad \text{(II.15)}$$

$$- \left| \vec{\nabla} \mathcal{E}_i(\vec{r},t) \right| = i |\vec{k}_i| \ \mathcal{E}_i(\vec{r},t) \qquad \text{(II.16)}$$

with the cannonical commutation rule

$$\left[\mathcal{E}_i(\vec{r},t), \ \mathcal{E}_j^{\dagger}(\vec{r}',t) \right] = \delta_{ij} \, \delta(\vec{r}-\vec{r}') \ . \qquad \text{(II.17)}$$

We use ω_s and ω_a to denote the uncoupled Stokes and AS frequencies which are given by $\omega_p - \omega_e$ and $\omega_p + \omega_e$ respectively. The wavenumbers $|\vec{k}_i|$ are related to ω_i by

$$\omega_i = \frac{c}{n_i} |\vec{k}_i| \ , \qquad i = p, s, a \ , \qquad \text{(II.18)}$$

with n_i the refractive index of the crystal at the i-th frequency. The free-field hamiltonian is, as usual,

$$H_F = \int \sum_i \hbar \omega_i \ \mathcal{E}_i^{\dagger}(\vec{r},t) \ \mathcal{E}_i(\vec{r},t) d\vec{r} \ . \qquad \text{(II.19)}$$

The radiation electron coupling is described by a hamiltonian density

$$\mathcal{H}_I = \hbar \left\{ m(\vec{r},t) + m^\dagger(\vec{r},t) \right\} \underset{\sim}{\mu} \vec{E} \vec{E} \tag{II.20}$$

for a coupling tensor $\underset{\sim}{\mu}$. For a specific set of polarization and propagation directions of the fields, we extract the Raman coupling of interest from (II.20)

$$\mathcal{H}_I = \hbar \left(m + m^\dagger \right)\left(\mu_s' \mathcal{E}_s \mathcal{E}_p + \mu_a' \mathcal{E}_a \mathcal{E}_p \right) . \tag{II.21}$$

The terms of importance from (II.21) in describing the Raman and four-photon processes are given by

$$\mathcal{H}_I = \hbar \mu_s' \left\{ \mathcal{E}_p^{(+)} \mathcal{E}_s^{(-)} m + \mathcal{E}_p^{(-)} \mathcal{E}_s^{(+)} m^\dagger \right\}$$
$$+ \hbar \mu_a' \left\{ \mathcal{E}_p^{(+)} \mathcal{E}_s^{(-)} m^\dagger + \mathcal{E}_p^{(-)} \mathcal{E}_a^{(+)} m \right\} . \tag{II.22}$$

The remaining anti-resonant terms in (II.21) are neglected in the rotating-wave approximation.[11][14]

We now relate the parameters μ_s' and μ_a' in (II.22) to the Stokes and AS scattering cross-sections $(d\sigma/d\Omega)_s$ and $(d\sigma/d\Omega)_a$, which can be obtained either by perturbation calculations or by experimental measurements. From the golden rule and (II.21), the Stokes transition rate is

$$W_s = \frac{2\pi}{\hbar} \left(\hbar \mu_s' \right)^2 \frac{\omega_s^2 n_s^2}{\hbar (2\pi c)^3}$$

$$= \left(\frac{d\sigma}{d\Omega} \right)_s \times \text{(photon flux)} \tag{II.23}$$

$$W_s = \left(\frac{d\sigma}{d\Omega}\right)_s \times \frac{\gamma_q L_1}{V} \ .$$

Here γ_q is the photon generation rate, V the volume of the crystal, and L_1 the crystal length to be explained fully in section V. Thus we have

$$\mu_s^2 \triangleq \frac{\mu_s'^2}{\gamma_q} = \frac{4\pi^2 c^3 L_1}{n_s^3 \omega_s^2} \left(\frac{d\sigma}{d\Omega}\right)_s \ . \tag{II.24}$$

Similarly for the AS waves

$$\mu_a^2 \triangleq \frac{\mu_a'^2}{\gamma_q} = \frac{4\pi^2 c^3 L_1}{n_s^3 \omega_s^2} \left(\frac{d\sigma}{d\Omega}\right)_a \ . \tag{II.25}$$

We have introduced different $\mu's$ which are more convenient to use in the following.

We have set up a complete quantum mechanical description of a nonlinear optical process involving quantum wave fields. The total hamiltonian is now specified by (II.12), (II.19) and (II.22)

$$H = H_I + H_e + H_F$$

$$= \int \left\{ \hbar\mu_s' \left[\mathcal{E}_p^{(+)}(\vec{r},t) \mathcal{E}_s^{(-)}(\vec{r},t) \, \mathcal{M}(\vec{r},t) + \mathcal{E}_p^{(-)}(\vec{r},t) \mathcal{E}_s^{(+)}(\vec{r},t) \, \mathcal{M}^\dagger(\vec{r},t) \right] \right.$$

$$\left. + \hbar\mu_a' \left[\mathcal{E}_p^{(+)}(\vec{r},t) \mathcal{E}_a^{(-)}(\vec{r},t) \, \mathcal{M}^\dagger(\vec{r},t) + \mathcal{E}_p^{(-)}(\vec{r},t) \mathcal{E}_a^{(+)}(\vec{r},t) \, \mathcal{M}(\vec{r},t) \right] \right.$$

$$+ \quad \hbar\omega_1 \, \mathcal{N}_1 (\vec{r}, t) + \hbar\omega_2 \, \mathcal{N}_2 (\vec{r}, t)$$

$$+ \quad \sum_i \hbar\omega_i \, \mathcal{E}_i^\dagger (\vec{r}, t) \, \mathcal{E}_i (\vec{r}, t) \Big\} \, d\vec{r} .$$

(II.26)

The hamiltonian density (II.20) can be compared to a classical one

$$\mathcal{H}_x^c \quad = \quad \underset{\sim}{\chi} \, \vec{E} \vec{E}$$

(II.27)

described by a second order nonlinear susceptibility $^{(3)}$ $\underset{\sim}{\chi}$

$$\underset{\sim}{\chi} \quad = \quad \hbar \underset{\sim}{\mu} \, (\mathcal{M} + \mathcal{M}^\dagger)$$

(II.28)

with $(\mathcal{M} + \mathcal{M}^\dagger)$ considered as a classical or averaged polarization density. Except for the electronic part, the hamiltonian (II.26) therefore has a definite classical correspondent.

In ordinary descriptions of Raman scattering from collective excitations, say SRS from phonons, the radiation and phonons interact through the electrons which are eliminated via the description of a susceptibility. In our case no collective excitations are present. Instead two of the electronic levels are involved explicitly in the scattering process, and we eliminated the rest of the electronic levels by an effective hamiltonian. The close analogy between our description of nonlinear optics and the usual approach should be evident.

III. EQUATIONS OF MOTION

The variables of our problem are now the radiation fields $\mathcal{E}_i(\bar{r},t)$, $\mathcal{E}_i^\dagger(\bar{r},t)$ the electron polarization density $\mathcal{M}(\bar{r},t)$, $\mathcal{M}^\dagger(\bar{r},t)$, and population densities $\mathcal{N}_1(\bar{r},t)$, $\mathcal{N}_2(\bar{r},t)$. We have a total number of ten field operators. Equations of motion for these variables can be obtained rom the hamiltonian (II.20), using the cannonical equation

$$\dot{O} = \frac{i}{\hbar} [H, O] \tag{III.1}$$

With the cannonical commutation rules (II.11) and (II.17), we obtain easily

$$\frac{c}{\eta_p} |\bar{\nabla} \mathcal{E}_p| + \frac{\partial \mathcal{E}_p}{\partial t} = - i \sqrt{\delta_q} \left(\mu_s \mathcal{E}_s \mathcal{M} + \mu_a \mathcal{E}_a \mathcal{M}^\dagger \right) \tag{III.2}$$

$$\frac{c}{\eta_s} |\bar{\nabla} \mathcal{E}_s| + \frac{\partial \mathcal{E}_s}{\partial t} = i \sqrt{\delta_q} \, \mu_s \, \mathcal{E}_p^\dagger \mathcal{M} \tag{III.3}$$

$$\frac{c}{\eta_a} |\bar{\nabla} \mathcal{E}_a| + \frac{\partial \mathcal{E}_a}{\partial t} = - i \sqrt{\delta_q} \, \mu_a \, \mathcal{E}_p \mathcal{M} \tag{III.4}$$

$$\frac{\partial \mathcal{M}}{\partial t} = -i \omega_e \mathcal{M} - i \sqrt{\delta_q} \, \mathcal{D} \left(\mu_s \mathcal{E}_p \mathcal{E}_s^\dagger + \mu_a \mathcal{E}_p^\dagger \mathcal{E}_a \right) \tag{III.5}$$

$$\frac{\partial \mathcal{N}_1}{\partial t} = - \mathcal{B} \tag{III.6}$$

$$\frac{\partial \mathcal{N}_2}{\partial t} = \mathcal{B} \quad . \tag{III.7}$$

Here

$$\mathcal{B} = i \sqrt{\delta_q} \, \mu_s \left(\mathcal{E}_p^\dagger \mathcal{E}_s \mathcal{M} - \mathcal{E}_p \mathcal{E}_s^\dagger \mathcal{M}^\dagger \right) \tag{III.8}$$

$$+ i \sqrt{\delta_q} \, \mu_a \left(\mathcal{E}_p \mathcal{E}_a^\dagger \mathcal{M} - \mathcal{E}_p^\dagger \mathcal{E}_a \mathcal{M}^\dagger \right)$$

can be interpreted as the difference of Stokes and AS radiative transition rate between levels 1 and 2. We have used (II.16) in obtaining (III.2)-(III.4). The adjoint equations of (III.2)-(III.5) can be written down directly, so that we have ten equations with ten unknowns.

Equations (III.2) - (III.7) are fully quantum mechanical equations for the operator variables. In this paper we will only be interested in the average or mean behavior of these variables. We therefore proceed to replace the operators by their expectation values. The linear terms pose no problem in such a procedure, but approximations are involved in, for example, the replacement of $\langle \mathcal{E}_p \mathcal{M} \rangle$ by $\langle \mathcal{E}_p \rangle \langle \mathcal{M} \rangle$. This amounts to neglecting some quantum fluctuation contribution to the mean equations, similar to the case of the well-known Ehrenfest's theorem. [15] Denoting the averages $\langle \mathcal{M} \rangle$ by unscripted case M , etc, we have equations for the variables $E_i(\vec{r}, t)$, $H(\vec{r}, t)$, $N_1(\vec{r}, t)$, $N_2(\vec{r}, t)$ identical to those of (III.2)-(III.7).

We next introduce loss terms into our equations. There is a great deal of literature [16] on first principle description of dissipation for both quantum and classical systems, which we will not discuss here. We just expand our equations (III.2) - (III.4) to read

$$\frac{c}{n_p} |\vec{\nabla} \mathcal{E}_p| + \frac{\partial \mathcal{E}_p}{\partial t} = - \frac{\gamma_p}{2} \mathcal{E}_p - i\sqrt{\gamma_q} \left(\mu_s E_s M + \mu_a E_a H^* \right) \tag{III.9}$$

$$\frac{c}{n_s} |\vec{\nabla} E_s| + \frac{\partial E_s}{\partial t} = - \frac{\gamma_s}{2} E_s - i\sqrt{\gamma_q} \, \mu_s \mathcal{E}_p H^* \tag{III.10}$$

$$\frac{c}{\eta_a} |\bar{\nabla} E_a| + \frac{\partial E_a}{\partial t} = - \frac{\gamma_a}{2} E_a - i \sqrt{\delta_g} \mu_a E_a M.$$ (III.11)

Here the variables $1/\gamma_i$ are the photon lifetimes for the i-th field in the crystal cavity. Since the loss term in the $E_i(\bar{r},t)$ equation would be of the form

$$- \gamma_i E_i(\bar{r},t)$$

according to the meaning of our γ_i, we have made the rotating wave-approximation in keeping the

$$- \frac{\gamma_i}{2} E_i$$

terms in (III.9) - (III.11) and throwing away the anti-resonant terms

$$- \frac{\gamma_i}{2} E_i^\dagger \quad .$$

These loss terms can also be introduced in the operator equations. In that case we have to also introduce quantum operator noise terms [11] for quantum mechanical consistency — for preservation of the cannonical commutation relations.

Loss terms in the electronic system can be introduced in a variety of ways. We use the ordinary rate equation approach, which can also be obtained from a first principle description. [16] Thus we extend (III.5) and (III.7) to

$$\frac{\partial M}{\partial t} = - \left(\frac{\Gamma}{2} + i\omega_e \right) M - i \sqrt{\delta_g} D \left(\mu_s E_s E_s^\dagger + \mu_a E_a E_a \right)$$ (III.12)

$$\frac{\partial N_1}{\partial t} = R_1 + W_{12} N_2 - T_1 N_1 - B$$ (III.13)

$$\frac{\partial N_2}{\partial t} = R_2 + W_{21} N_1 - \Gamma_2 N_2 + B.$$ (III.14)

The quantity Γ is the full-width of the spontaneous Stokes line-width.[*] The other rate constants $W's$ and $\Gamma's$ have their obvious transition rate-in rate-out interpretations, as indicated in Figure 2.3. They describe the non-scattering transitions, i.e., transitions between 1 and 2 except those from the Raman and four-photon processes. The constants R_1 and R_2 can be interpreted as non-scattering transition rates into levels 1 and 2, or it can be regarded as representing the population effects of other levels in the electron system. A detailed discussion of the procedure for deriving the loss terms in both radiation and matter can be found in many places. [16]

We make a further simplifying assumption before we proceed. We consider the geometry of our problem as in Figure 2.4. The cavity length is along the z-direction. The Stokes and AS output would therefore propagate near the direction $\hat{z}$. We assume that all the waves involved are uniform in the x-y plane. This assumption depends of course on the propagation direction and distribution of the input beam, and is particularly good for the collinear case. Thus we have our equations

$$\frac{c}{n_p} \frac{\partial E_p}{\partial z} + \frac{\partial E_p}{\partial t} = -\frac{\gamma_p}{2} E_p - i\sqrt{\delta_q} \left(\mu_s E_s M + \mu_a E_a M^* \right)$$ (III.15)

$$\frac{c}{n_s} \frac{\partial E_s}{\partial z} + \frac{\partial E_s}{\partial t} = -\frac{\gamma_s}{2} E_s - i\sqrt{\delta_q} \mu_s E_p M^*$$ (III.16)

$$\frac{c}{n_a} \frac{\partial E_a}{\partial z} + \frac{\partial E_a}{\partial t} = -\frac{\gamma_a}{2} E_a - i\sqrt{\delta_q} \mu_a E_p M$$ (III.17)

---

[*] That this formulation can be used to describe an inhomogeneously broadened system under certain situations is shown in the next chapter.

$$\frac{\partial M}{\partial t} = -\left(\frac{\Gamma}{2} + i\omega_e\right)M - i\sqrt{8_q}\,D\left(\mu_s E_p E_s^* + \mu_a E_p E_a\right) \tag{III.18}$$

$$\frac{\partial D}{\partial t} = R_D + \Gamma_{DS}\,S - \Gamma_{DD}\,D - \partial B \tag{III.19}$$

$$\frac{\partial S}{\partial t} = R_S - \Gamma_{SS}\,S + \Gamma_{SD}\,D\,, \tag{III.20}$$

where we have transformed to the $D(\vec{r},t)$, $S(\vec{r},t)$ variables with

$$R_S = R_1 + R_2$$

$$R_D = R_1 - R_2 \tag{III.21}$$

$$\Gamma_{SS} = -\frac{1}{2}\left(W_{12} + W_{21} - \Gamma_1 - \Gamma_2\right)$$

$$\Gamma_{SD} = \frac{1}{2}\left(W_{21} - W_{12} + \Gamma_2 - \Gamma_1\right) \tag{III.22}$$

$$\Gamma_{DD} = \frac{1}{2}\left(W_{12} + W_{21} + \Gamma_1 + \Gamma_2\right)$$

$$\Gamma_{DS} = \frac{1}{2}\left(W_{12} - W_{21} + \Gamma_2 - \Gamma_1\right)\,. \tag{III.23}$$

These equations describe propagation of the variables inside the crystal medium. Excitation will be in the form of boundary condition from $E_p(z,t)$. No

source term is therefore needed in (III. 15). Note that equations (III. 15) - (III. 17)

can also be derived directly from a classical susceptibility. Physical interpretations

of the various terms in (III. 15) - (III. 20) are evident and satisfying.

IV. STEADY STATE SOLUTION

The mean behavior of our Raman laser is now completely described by the

s et of equations (III. 15) - (III. 20). Although these equations form a highly

complicated system of coupled nonlinear partial differential equations, their

steady state solution can be obtained relatively easily. We first discuss the

kinematics of the wave couplings.

In Figure 2.5 is shown a wave vector diagram of the scattering process.

Because of the coupling of waves, the actual Stokes and AS wavevectors $\vec{k}_s$, $\vec{k}_a$

are not given by the linear dispersion relations (IV. 2). $\vec{k}_s$, $\vec{k}_a$ and $\vec{k}_p$

satisfy the phase matching condition (IV. 8), and the Stokes and AS waves come out

in cones making angles θ_s , θ_a with $\hat{z}$. We do not know θ_s and θ_a hence the

$\hat{x}$ and $\hat{y}$ components of $\vec{k}_s$ and $\vec{k}_a$. However, the whole kinematic problem can

be solved once we know Δk , the difference between the actual and unperturbed

$\hat{z}$-components of the wavevectors as defined in (IV. 5). In section VI, Δk will

be determined through a maximization of the gain coefficient. Thus in this

section we will assume Δk to be a known constant and proceed to solve the

kinematics.

Let $\vec{k}_p$ and $\vec{k}_e$ be the wavevectors of the pump laser and the electronic polarization density, and $\vec{k}_s$, $\vec{k}_a$ be those of the uncoupled Stokes and AS fields,

$$|\vec{k}_s^{\circ}| = \frac{n_s}{c}\omega_s$$

$$|\vec{k}_a^{\circ}| = \frac{n_a}{c}\omega_a \quad . \tag{IV.2}$$

Following Shen and Bloembergen, [2] we introduce the $\hat{z}$-components of the wavevectors, k_{p_3} , $k_{s_3}^{\circ}$, $k_{a_3}^{\circ}$, and k_{e_3} ,

$$k_{s_3}^{\circ} = \left\{ |k_s^{\circ}|^2 - (k_{sx}^2 + k_{sy}^2) \right\}^{1/2}$$

$$k_{a_3}^{\circ} = \left\{ |k_a^{\circ}|^2 - (k_{ax}^2 + k_{ay}^2) \right\}^{1/2} , \tag{IV.3}$$

and the momentum mismatch Δk_s and Δk_a ,

$$k_{p_3} - k_{e_3} = k_{s_3}^{\circ} + \Delta k_s$$

$$k_{p_3} + k_{e_3} = k_{a_3}^{\circ} + \Delta k_a , \tag{IV.4}$$

so that

$$2 k_{p_3} = k_{s_3}^{\circ} + k_{a_3}^{\circ} + \Delta k . \tag{IV.5}$$

These relations are shown in Figure 2.5 for negative total mismatch

$$\Delta k = \Delta k_s + \Delta k_a \; .$$ (IV.6)

It will be shown in section VI that the gain of the coupled waves depends on the $\Delta k_i's$ only through the combination Δk , which is then determined by maximizing the gain. With a given Δk , we can find ks_δ^o and ka_δ^o from (IV.2) and (IV.4) through the angles θ_s^o and θ_a^o as in Figure 2.5. In the following we will assume that the difference

$$\Delta k' = \Delta k_s - \Delta k_a$$ (IV.7)

is small compared to other wavenumbers of interest. In this case the number ke_δ and the vector $\vec{k}_e$ is also determined together with the coupled wavevectors $\vec{k}_s$, $\vec{k}_a$ through the relation (IV.4) and the following equations

$$\vec{k}_p = \vec{k}_s + \vec{k}_a$$

$$\vec{k}_a = \vec{k}_p + \vec{k}_e \qquad .$$ (IV.8)

Geometry of these various wavevectors is depicted in Figure 2.5. Directions of the outgoing wave θ_s and θ_a for Stokes and AS wave cones are given by the following formulas in terms of Δk and θ_s^o , θ_a^o

$$\sin\theta_{s,a} = \frac{|k_{s,a}^o| \sin\theta_{s,a}^o}{\sqrt{\left(\frac{\Delta k}{2}\right)^2 + |k_{s,a}^o|^2 - |k_{s,a}^o||\Delta k|\cos\theta_{s,a}^o}}$$ (IV.9)

where $\theta_{s,a}^o$ are given by the solutions of the following equations

$$|k_{a,s}^{o}|^{2} = \left\{ |k_{s,a}^{o}| - 2|k_{p}| \frac{\sin\theta_{p}}{\sin\theta_{s,a}^{o}} \right\}^{2}$$

$$+ \left\{ 2k_{p_{3}} \left(1 - \frac{2|k_{p}|\sin\theta_{p}}{|k_{s,a}^{o}|\sin\theta_{s,a}^{o}} \right) + |\Delta k| \right\}^{2}$$

$$- 2\cos\theta_{s,a}^{o} \left\{ |k_{s,a}^{o}| - 2|k_{p}| \frac{\sin\theta_{p}}{\sin\theta_{s,a}^{o}} \right\}$$

(IV.10)

$$\times \left\{ 2k_{p_{3}} \left(1 - \frac{2|k_{p}|\sin\theta_{p}}{|k_{s,a}^{o}|\sin\theta_{s,a}^{o}} \right) + |\Delta k| \right\} .$$

For pump waves incident in the z-direction, we have $\theta_{p} = 0$ so that (IV.9) reduces to

$$\cos\theta_{s,a}^{o} = \frac{-|k_{a,s}^{o}|^{2} + |k_{s,a}^{o}|^{2} + \left(2k_{p_{3}} + |\Delta k| \right)^{2}}{2|k_{s,a}^{o}| \left(2k_{p} + |\Delta k| \right)}$$

(IV.11)

Other relations can be similarly determined from the geometry of Figure 2.5.

We now proceed to determine the sinusoidal steady state oscillation of the system. Thus we define

$$E_{s} = E_{s}' e^{i(k_{s}^{o}_{3} + \Delta k_{s})_{3} - i\omega_{s}t}$$

$$E_{a} = E_{a}' e^{i(k_{a}^{o}_{3} + \Delta k_{a})_{3} - i\omega_{a}t}$$

(IV.12)

$$E_{p} = E_{p}' e^{ik_{p_{3}3} - i\omega_{p}t}$$

(IV.13)

$$M = M' e^{ik_{e}_{3} - i\omega_{e}t}$$

(IV.14)

to remove the dominant oscillation of the variables, and rewrite (III.15) - (III.20) as

$$\frac{c}{n_p}\frac{\partial E_p'}{\partial \zeta} + \frac{\partial E_p'}{\partial t} = -\frac{\gamma_p}{2}E_p' - i\sqrt{\delta_g}\left(\mu_s E_s' M' + \mu_a E_a' M'^*\right) \tag{IV.15}$$

$$\frac{c}{n_s}\frac{\partial E_s'}{\partial \zeta} + \frac{\partial E_s'}{\partial t} = -\frac{\gamma_s}{2}E_s' - i\frac{c}{n_s}\Delta k_s E_s' - i\sqrt{\delta_g}\mu_s E_s' M'^* \tag{IV.16}$$

$$\frac{c}{n_a}\frac{\partial E_a'}{\partial \zeta} + \frac{\partial E_a'}{\partial t} = -\frac{\gamma_a}{2}E_a' - i\frac{c}{n_a}\Delta k_a E_a' - i\sqrt{\delta_g}\mu_a E_a' M' \tag{IV.17}$$

$$\frac{\partial M}{\partial t} = -\frac{\Gamma}{2}M - i\sqrt{\delta_g}D\left(\mu_s E_p' E_s'^* + \mu_a E_p'^* E_a'\right) \tag{IV.18}$$

$$\frac{\partial D}{\partial t} = R_D + \Gamma_{DS}S - \Gamma_{DD}D - 2B \tag{IV.19}$$

$$\frac{\partial S}{\partial t} = R_S - \Gamma_{SS}S + \Gamma_{SD}D \tag{IV.20}$$

$$B = i\sqrt{\delta_g}\mu_s\left(E_p'^* E_s' M' - E_p' E_s'^* M'^*\right) + i\sqrt{\delta_g}\mu_a\left(E_p' E_a'^* M' - E_p'^* E_a' M'^*\right). \tag{IV.21}$$

For the moment we will leave the E_p' equation aside and consider equations (IV.16) - (IV.20) with E_p' as a parameter. Superimposed on the individual oscillators we set

$$E_s' = E_s'' e^{k\zeta - i\omega t}$$

$$E_a' = E_a'' e^{k\zeta - i\omega t} \tag{IV.22}$$

$$H' = H'' e^{k\zeta - i\omega t}$$

for real K and ω . This accounts for the spatial growth[17] and frequency

pulling of the system. We neglect temporal growth in this paper. Substitution

of (IV.22) into (IV.16) - (IV.20) results in the algebraic equations

$$\left\{ \frac{cK}{\eta_s} + \frac{\gamma_s}{2} - i(\omega + \Delta_s) \right\} E_s'' + i\sqrt{\gamma_q}\, \mu_s E_p' M^{*''} = 0 \tag{IV.23}$$

$$\left\{ \frac{cK}{\eta_a} + \frac{\gamma_a}{2} - i(\omega - \Delta_a) \right\} E_a'' + i\sqrt{\gamma_q}\, \mu_a E_p' M'' = 0 \tag{IV.24}$$

$$\left\{ \frac{\Gamma}{2} - i\omega \right\} M' + i\sqrt{\gamma_q} D \left(\mu_s E_p' E_s''^* + \mu_a E_p'^* E_a'' \right) = 0 \tag{IV.25}$$

$$R_D + T_{DS} S - T_{DD} D - 2B = 0 \tag{IV.26}$$

$$R_S - T_{SS} S + T_{SD} = 0 \tag{IV.27}$$

In the steady state the gain and loss coefficients cancel each other with $K = 0$.
A solution for E_s , E_a and M is then possible from (IV.23) - (IV.25)
only if the following determinant vanishes.

$$\begin{pmatrix} \frac{\gamma_s}{2} - i(\bar{\omega} + \Delta_s) & 0 & -i\mu_s \bar{E}_p'^* \\ 0 & \frac{\gamma_a}{2} - i(\bar{\omega} - \Delta_a) & i\mu_a \bar{E}_p' \\ i\bar{D}\mu_s^2\sqrt{\gamma_q}\,\bar{E}_p' & i\bar{D}\mu_a^2\sqrt{\gamma_q}\,\bar{E}_p'^* & \frac{\Gamma}{2} - i\bar{\omega} \end{pmatrix} = 0 . \tag{IV.28}$$

We use a bar to denote steady state values. This equation obviously holds

regardless of whether $\bar{E}_p'$ is a function of the other variables. In the next

section $\bar{E}_p$ will be obtained as a function of the other variables to account for pump depletion.

The determinantal condition (IV.28) yields two real equations

$$\frac{1}{8}\Gamma \gamma_s \gamma_a - \frac{\Gamma}{2}(\bar{\omega}+\Delta_s)(\bar{\omega}-\Delta_a) \tag{IV.29}$$

$$-\frac{\bar{\omega}}{2}\left[\gamma_s(\bar{\omega}-\Delta_a)+\gamma_a(\bar{\omega}+\Delta_s)\right] + \bar{D}\bar{P}_p \frac{1}{2}(\gamma_s\mu_a^2 - \gamma_a\mu_s^2) = 0$$

$$\bar{\omega}\left[\frac{1}{4}\gamma_s\gamma_a - (\bar{\omega}+\Delta_s)(\bar{\omega}-\Delta_a)\right] + \frac{\Gamma}{4}\left[\gamma_s(\bar{\omega}-\Delta_a)+\gamma_a(\bar{\omega}+\Delta_s)\right]$$

$$+ \bar{D}\bar{P}_p\left[\mu_a^2(\bar{\omega}+\Delta_s)-\mu_s^2(\bar{\omega}-\Delta_a)\right] = 0 \tag{IV.30}$$

We can regard these equations as determining the steady state frequency shift $\bar{\omega}$ and population difference $\bar{D}$ in terms of $\bar{E}_p$ and other constants. We have introduced the notations

$$\bar{P}_p = \gamma_g |\bar{E}_p|^2 \tag{IV.31}$$

$$\Delta_s = \frac{c}{n_s}\Delta k_s$$

$$\Delta_a = \frac{c}{n_a}\Delta k_a \tag{IV.32}$$

for simplicity. The coupled algebraic equations (IV.29) - (IV.30) do not yield an algebraic analytic solution in general. Further approximations will be made later to obtain explicit expressions for $\bar{\omega}$ and $\bar{D}$. In the following we will therefore regard $\bar{\omega}$ and $\bar{D}$ as known constants.

The Stokes versus AS power ratio can be immediately obtained from (IV.23) and (IV.24)

$$r \triangleq \frac{\hbar \omega_a \bar{P}_a}{\hbar \omega_s \bar{P}_s} \triangleq \frac{\hbar \omega_a \gamma_a |\bar{E}_a|^2}{\hbar \omega_s \gamma_s |\bar{E}_s|^2}$$

$$= \frac{\gamma_a \omega_a \mu_a^2}{\gamma_s \omega_s \mu_s^2} \frac{(\gamma_s/2)^2 + (\bar{\omega} + \Delta_s)^2}{(\gamma_a/2)^2 + (\bar{\omega} - \Delta_a)^2} \quad . \tag{IV.33}$$

We note that $P_i \triangleq \gamma_i |E_i|^2$ is the photon dissipation rate, and is therefore also the photon generation rate in the steady state. The radiative transition rate becomes, from (IV.25)

$$\bar{B} = \bar{P}_s - \bar{P}_a \quad . \tag{IV.34}$$

From equations (IV.26) and (IV.27) we obtain

$$\bar{B} = \frac{1}{2} (b_1 - b_2 \bar{D}) \tag{IV.35}$$

$$\bar{S} = \frac{1}{T_{ss}} (R_s + T_{sp} \bar{D}) \quad , \tag{IV.36}$$

with

$$b_1 \triangleq R_D + R_s T_{Ds} / T_{ss}$$

$$b_2 \triangleq \Gamma_{DD} - T_{sD} T_{Ds} / T_{ss} . \tag{IV.37}$$

The Stokes and AS power generated are then given by

$$\hbar \omega_s P_s = \frac{\hbar \omega_s}{2\left(1 - r \gamma_s \omega_s / \gamma_a \omega_a\right)} \left(b_1 - b_2 \bar{D}\right) \qquad \text{(IV.38)}$$

$$\hbar \omega_a P_a = \frac{r \hbar \omega_a}{2\left(1 - r \gamma_s \omega_s / \gamma_a \omega_a\right)} \left(b_1 - b_2 \bar{D}\right) \ . \qquad \text{(IV.39)}$$

A detailed investigation of such steady state power behavior will be given in following sections.

The relative phases of the system variables can also be determined accordingly. Let us write

$$\bar{M} = \sqrt{\bar{P}_m} \; e^{i\bar{\varphi}_m}$$

$$\bar{E}_p = \sqrt{\bar{P}_p / \gamma_q} \; e^{i\bar{\varphi}_p}$$

$$\bar{E}_s = \sqrt{\bar{P}_s / \gamma_s} \; e^{i\bar{\varphi}_s} \qquad \text{(IV.40)}$$

$$\bar{E}_a = \sqrt{\bar{P}_a / \gamma_a} \; e^{i\bar{\varphi}_a} \ .$$

We find straightforwardly from (IV.23) - (IV.26)

$$\bar{P}_m = \frac{\bar{P}_s}{\gamma_s \mu_s^2 \bar{P}_p} \left\{ \left(\frac{\gamma_s}{2}\right)^2 + \left(\bar{\omega} + \Delta_s\right)^2 \right\} \qquad \text{(IV.41)}$$

$$\bar{\varphi}_m + \bar{\varphi}_s = \varphi_0 + \varphi_1 - \frac{\pi}{2} \qquad \text{(IV.42)}$$

$$\bar{\varphi}_m - \bar{\varphi}_a = \varphi_2 - \varphi_0 + \frac{\pi}{2} \ , \qquad \text{(IV.43)}$$

with

$$\varphi_1 \triangleq \tan^{-1}\left(-\frac{\bar{\omega}+\Delta_s}{\gamma_s/2}\right)$$

$$\varphi_2 \triangleq \tan^{-1}\left(-\frac{\bar{\omega}-\Delta_a}{\gamma_a/2}\right) \; .$$

(IV.44)

Thus only the relative phases of $\bar{\varphi}_s$, $\bar{\varphi}_a$ and $\bar{\varphi}_m$ can be determined. Equation (IV.15) also does not yield any additional condition. The arbitrariness left corresponds to the phase instability [11] of the laser.

To develop the usefulness of our equations in this section fully we have to treat the pump equation now and to solve equations (IV.29) - (IV.30) for $\bar{\omega}$ and $\bar{D}$.

V. DEPLETION OF PUMP FIELD

We wish to demonstrate here how depletion of the input laser can be properly taken into account. We first discuss the geometry and the definitions of the various power and flux terms involved. Consider the geometries of Figures 2.6 and 2.7. The input field excites the scattering volume in the form of a boundary condition, as mentioned before. The input flux (power per unit area) is denoted by $J_{in}^{\,o}$. The pump power per unit volume inside the crystal is denoted by $\hbar\omega_p \, P_{in}^{\,o}$.

We let

$$L_1 = \text{crystal length}$$

$$L_2 = \text{gain length}$$

(V.1)

$$L_3 = \text{crystal length.}$$

The transmission from outside to the crystal medium at the input interface 1 has a transmissivity T'. From the medium to outside at the output interface 2 one has reflectivity R and transmissivity T. We can usually assume $T + R = 1$, and $T = T'$. Let I_s and I_a be the Stokes and AS flux around the z direction outside the crystal. In the steady state the Stokes and AS power are uniform in the crystal so that

$$\bar{P}_{1m} = \bar{P}_{2m} = \bar{P}_{1m}\, e^{(g'L_2 - \frac{n\alpha}{2c}L_3)} R = \bar{P}_{1m}\, e^{(g - \frac{n\gamma}{2c})L_3}, \tag{V.2}$$

where g' is the actual gain coefficient, g a normalized gain, and $\bar{P}_{1m}$, $\bar{P}_{2m}$ are the power inside the medium at interfaces 1 and 2 respectively. The output power is therefore

$$\bar{P}_{outside} = \bar{P}_{2m}\, e^{(g'L_2 - \frac{\alpha n}{2c}L_3)} T$$

$$= \bar{P}_{2m}\, T/R \tag{V.3}$$

$$= \bar{P}_{inside}\, T/R.$$

We can then write

$$I_{in}^{\circ} = P_{in}^{\circ}\, \hbar\omega_p L_1\, /T' $$

$$I_s = \bar{P}_s\, \hbar\omega_s L_2\, T/R \tag{V.4}$$

$$I_a = \bar{P}_a\, \hbar\omega_a L_3\, T/R. \tag{V.5}$$

The loss coefficient γ can also be written

$$\gamma_i = \frac{2c}{n_i}\left(\alpha_i - \frac{\ell n R}{L_3}\right), \qquad i = p, s, a, \tag{V.6}$$

including bulk absorption loss α_i and transmission loss. The difference of the L's will become important in, for example, the non-collinear geometry of Figure 2.7.

We now discuss the effect of the laser pump depletion. There are two basic causes of depletion, due to absorption from γ and conversion to Stokes as well as AS radiations. The absorption can usually be neglected for small γ. For sufficiently small α_p it can be taken into account by using the following reduced P_{in} instead of $P_{in}^{\,o}$ to represent the rate of photon input into the crystal,

$$P_{in} = P_{in}^{\,o} \frac{\int_o^{L_1} e^{-\alpha \ell} d\ell}{L_1}$$

$$= P_{in}^{\,o} \frac{1 - e^{-\alpha L_1}}{\alpha L_1} \quad .$$

(V.7)

The condition on L_1 being

$$\alpha L_1 \lesssim 1 \quad .$$

(V.8)

Hereafter we will assume that (V.8) is obeyed and that substitution of the form (V.7) are to be made. Note that $I_{in}^{\,o}$ is still related to $P_{in}^{\,o}$ as in (V.4).

We consider the effect of conversion by studying equation (IV.15), where we can now neglect the loss term as discussed above. We have therefore

$$\frac{c}{n_p} \frac{\partial E_p'}{\partial z} + \frac{\partial E_p'}{\partial t} = -i \sqrt{\gamma_q} \left(\mu_s E_s' H' + \mu_a E_a' H^* \right)$$

(V.9)

Since only P_p appears in the equations of (IV.29) and therefore, we convert (V.9) to

$$\frac{c}{n_p} \frac{\partial |E_p'|^2}{\partial z} + \frac{\partial |E_p'|^2}{\partial t}$$

$$= - \left(\frac{c}{n_s} \frac{\partial}{\partial z} + \frac{\partial}{\partial t}\right) |E_s'|^2 - \left(\frac{c}{n_a} \frac{\partial}{\partial z} + \frac{\partial}{\partial t}\right) |E_a|^2 .$$

(V.10)

This equation is solved by the expression

$$|E_p'|^2 = \frac{P'}{\gamma_q} = \frac{P_{in}}{\gamma_q} - \beta \left\{ \frac{n_p P_s'}{n_s \gamma_s} + \frac{n_p P_a'}{n_a \gamma_a} \right\} ,$$

(V.11)

with $\beta = 1$. Note that $P_p = P_p'$. The constant P_{in} corresponds to the solution in the absence of Stokes conversion, and can be taken to be that of (V.7). It arises directly from the boundary condition that a constant input is present. In the absence of coupling and loss, the boundary condition clearly becomes the solution of P_p inside the medium. Our equation (V.11) therefore effectively solves the boundary value problem of boundary condition excitation. The parameter β is introduced for comparison so that in the limit of small Stokes conversion, the solution for $|E_p|^2$ can be taken from (V.11) with $\beta = 0$.

Equation (V.11) provides an exact solution to equation (V.10), although only approximate as far as the original equation (IV.15) is concerned. It can be interpreted as photon number conservation, as P/γ represent the number of photons in each mode. The generation of each Stokes or AS photon requires a pump photon, although an AS photon is always generated with an accompanying Stokes photon. Equation (V.11) thus enforces the conservation of photons in the conversion processes explicitly, apart from the absorption loss.

Strictly speaking, equation (IV. 15) applies only to the collinear geometry of Figure 2.6. Even in other geometries, the application of (V. 11) to account for pump depletion appears justified for several reasons. In the first place its simple interpretation and reasonableness lend itself to be a good "ansatz" in studying depletion effects. Although the equations of motion may involve more spatial coordinates in other geometric configurations, it seems that in the steady state equations like (V. 10) and (V. 11) would still hold. We will therefore employ (V. 11) in both geometries of Figure 2.6 and Figure 2.7 in the following analysis. Equation (V. 11) can be substituted directly into the equations of section IV for E_p' and close the system.

VI. SPECIFIC SOLUTION

We want to obtain specific results by solving equations (IV.29) - (IV.30). While they can be readily solved numerically, we like to obtain analytical results by making simplifying assumptions. Thus we neglect the dispersion of the crystal and the frequency dependence of the loss,

$$n_s \simeq n_a \simeq n_p = n \qquad (VI.1)$$

$$\gamma_s \simeq \gamma_a \simeq \gamma_p = \gamma \qquad (VI.2)$$

We also assume

$$\mu_s \sim \mu_a = \mu \qquad (VI.3)$$

Since the cross-sections $(d\sigma/d\Omega)_s$ and $(d\sigma/d\Omega)_a$ are frequently equal, (VI.3) is closely consistent with (VI.1).

With (VI.1) - (VI.3), equations (IV.29) - (IV.30) can be solved immediately with two pairs of solutions

$$\bar{\omega} = -\frac{\Delta}{2}\sqrt{\frac{\Gamma}{\Gamma+2\gamma}}\left(1+\frac{\gamma^2}{\Delta^2}\right)^{\frac{1}{2}}$$

$$\bar{D} = \frac{\gamma}{8\mu^2\bar{P}_p}\left\{(\gamma+\Gamma)^2+\Delta^2\right\}\left\{(1+\frac{\gamma^2}{\Delta^2})^2\left[\frac{\Gamma/2}{(\Gamma/2+\gamma)^3}\right]\right\}^{\frac{1}{2}}$$

(VI.4)

and

$$\bar{\omega} = \frac{\Delta}{2}\left\{\frac{\Gamma}{\Gamma+2\gamma}\left(1+\frac{\gamma^2}{\Delta^2}\right)\right\}^{\frac{1}{2}}$$

$$\bar{D} = -\frac{\gamma}{8\mu^2\bar{P}_p}\left\{(\gamma+\Gamma)^2+\Delta^2\right\}\left\{(1+\frac{\gamma^2}{\Delta^2})^2\frac{\Gamma/2}{(\Gamma/2+\gamma)^3}\right\}^{\frac{1}{2}}$$

(VI.5)

where

$$\Delta = \Delta_s + \Delta_a = \frac{c}{n}(\Delta k_s + \Delta k_a).$$ (VI.6)

The pair (VI.4) corresponds to the case with a positive population difference, and (VI.5) to the case with an initial population inversion. We will henceforth consider the case (VI.4) only. In this case $\bar{D}$ plays a similar role to the population inversion in an ordinary laser.

A. SPATIAL GAIN

Since $\tilde{P}_p$ can be related to the other variables as in (V.11) it remains only to determine Δk for obtaining explicit formulas for the powers. The mismatch Δk is determined in the following way. Under conditions (VI.1) - (VI.3), the gain eigenvalues K of (IV.22) - (IV.25) has real part [#]

$$K = -\frac{n\gamma}{2c} + g \qquad \text{(VI.7)}$$

where the normalized gain coefficient g is

$$g = \frac{n}{c}\sqrt{\frac{\Delta}{2}} \left\{ -\frac{\Delta}{4} - \frac{\bar{D}\mu^2 \bar{P}_p \bar{\omega}}{\Gamma^2/4 + \omega^2} \right.$$

$$\left. + \sqrt{\frac{\Delta^2}{16} + \frac{\bar{D}\mu^2 \bar{P}_p}{\Gamma^2/4 + \omega^2}\left(\frac{\bar{\omega}}{2}(\Delta) + \bar{D}\mu^2\bar{P}_p\right)} \right\}. \qquad \text{(VI.8)}$$

The gain coefficient should be modified by a constant if the gain length is different from the cavity length, according to (V.2).

We note that the gain coefficient g is a function of Δk. As the pump power increases, g will increase until along certain directions stimulated radiation starts to occur when the gain cancels the loss γ. The mismatch Δk will then take the value corresponding to the output direction. Physically we are asserting that the Stokes and AS radiation will occur in the direction of maximum

---

[#] The imaginary part of K is always set to zero, since the momentum mismatch has been absorbed in Δk. Together with the vanishing of (VI.7), we have obtained the values (VI.4) - (VI.5).

gain. As the direction is determined by Δk as in Figure 2.4, we choose the Δk which maximizes the gain. Therefore we have, setting

$$\frac{\partial g}{\partial(\Delta k)}\bigg|_{\overline{\Delta k}} = 0 \ ,$$

$$\overline{\Delta k} = - \frac{\eta}{c} \frac{2\bar{D}\mu^2}{\bar{\omega}} \ \bar{P}_p \ , \tag{VI.9}$$

and the resulting gain is

$$g = \frac{\eta}{c} \frac{\bar{D}\mu^2}{\sqrt{\Gamma^2/4 + \bar{\omega}^2}} \ \bar{P}_p \ . \tag{VI.10}$$

The behavior of g as function of Δk is plotted in Figure 2.8. We observe that as $\Delta k \longrightarrow \pm \infty$

$$g(\Delta k \longrightarrow \pm \infty) = \frac{\eta}{c} \frac{\Gamma}{2} \frac{\bar{D}\mu^2 \bar{P}_p}{\Gamma^2/4 + \bar{\omega}^2} \ , \tag{VI.11}$$

and

$$\partial g / \partial(\Delta k) > 0 \ , \qquad \Delta k > 0 \ . \tag{VI.12}$$

The gain coefficient (VI.7) can be strictly interpreted as a gain only if $\bar{P}_p$ is a constant. In this case it corresponds to the familiar linear spatial gain and can be compared to the usual expression, say from Shen and Bloembergen.[2] With their equation (55) we have the following correspondence

$$K \longleftrightarrow \text{Im} (\Delta k)$$

$$\Delta \longleftrightarrow \frac{c}{n} \Delta k$$

$$i \; \frac{D \mu^2 \gamma_q}{\Gamma - i\omega} \longleftrightarrow \frac{2\pi \omega_s^2}{c k_{s_3}^m} \, (\chi_s + \chi_{NR}) .$$ (VI.13)

The major difference is that we have neglected $Re(\chi_s)$ and χ_{NR} in our treatment. The contribution of χ_{NR} is usually small compared with $Im(\chi_s).$[2] In the Lorentzian model, $Re(\chi_s)$ is exactly zero at resonance and is small close to resonance.[12][13] It is therefore justified to neglect them. Shen and Bloembergen[2] were not able to produce analytic formulas in retaining these contributions. Furthermore the use of complex susceptibility gives rise to complex hamiltonians, which we are able to aviod.

B. FREQUENCY SHIFT AND POPULATION DIFFERENCE

Substituting (IV.9) into (VI.4) we obtain

$$\bar{\omega} = \frac{1}{2} \sqrt{\delta \Gamma}$$ (VI.14)

$$\bar{D} = \frac{\gamma \Gamma}{4 \mu^2 \bar{P}_p} \, (1 + \gamma/\Gamma)^{\frac{1}{2}} .$$ (VI.15)

The operating frequency is shifted from ω_s, ω_a because of the cpupling of waves. The Stokes and AS will oscillate at frequencies

$$\bar{\omega}_s = \omega_0 - (\omega_e + \bar{\omega})$$ (VI.16)

$$\bar{\omega}_a = \omega_o + (\omega_e + \bar{\omega})$$,

Equation (VI.15) shows that an increase in either the electronic or photon dissipation constant would demand a larger coupling strength μ^2 or laser pump rate $\bar{P}_p$ would reduce the $\bar{D}$ required. These behavior are certainly reasonable. The factor $(1 + \gamma/\Gamma)^2$ accounts for the detuning effect, which increases the population difference needed for lasing.

C. STOKES ANTISTOKES POWER RATIO

With (VI.1) - (VI.3) the Stokes AS power ratio Γ becomes

$$\Gamma = \frac{\omega_a}{\omega_s} \frac{\gamma^2 + (2\bar{\omega} + \Delta)^2}{\gamma^2 + (2\bar{\omega} - \Delta)^2} .$$

(VI.17)

Note that $\Delta k > 0$ when $\bar{D} < 0$, and in this case $\bar{P}_a > \bar{P}_s$ as expected. In Figure 2.9 we plot Γ as a function of $\Delta k/\Gamma$ for several values of

γ/Γ . On each curve, the cross indicates the Δk value of maximum gain. In all cases, the antistokes photon number density is almost equal to that of stokes for $\Delta k \simeq 0$. This is because the dispersion of the refractive index is neglected so that the phase matching condition which is required for antistokes generation is satisfied in the nearforward direction collinearly with the pump wave, i.e., for small Δk. As Δk increases, the AS to Stokes ratio decreases and finally, as Δk approaches infinity

$$\Gamma \longrightarrow \frac{\omega_a}{\omega_s} \left\{ \frac{\sqrt{1 + 2\gamma/\Gamma} - 1}{\sqrt{1 + 2\gamma/\Gamma} + 1} \right\}^2 , \qquad \Delta k \to \pm \infty$$

(VI.18)

This drop in AS intensity is not surprising since the phase matching requirement

cannot be satisfied for such large Δk . At the direction of maximum gain, as

obtained by putting (VI.15) and (VI.14) into (VI.9)

$$\overline{\Delta k} = -\frac{n}{c}\left[\gamma(\gamma + \Gamma)\right]^{1/2} \qquad \text{(VI.19)}$$

the antistokes to Stokes ratio is

$$r = \frac{\omega_a}{\omega_s} \frac{\sqrt{1 + \gamma/\Gamma} - 1}{\sqrt{1 + \gamma/\Gamma} + 1} \qquad . \qquad \text{(VI.20)}$$

Note that the ratio in (VI.18) and (VI.20) is independent of the pump level.

From (VI.20) we see that

$$|E_a|^2 \ll |E_s|^2 \quad , \qquad\qquad \gamma \ll \Gamma$$

$$|E_a|^2 \simeq |E_s|^2 , \qquad\qquad \gamma \gg \Gamma \quad .$$

This can be qualitatively understood as follows. In general it can be seen from

the equations of motion that when $\gamma \gg \Gamma$, the photons will relax to quasi-equilibrium

faster than the electrons.   They will follow the electrons adiabatically. The

four-photon parametric process for Stokes-AS generation described in section II

is clearly favorable in this situation of rapid electronic transitions. Hence the

number of AS photon created is comparable with the number of Stokes photon.

When the reverse is true, $\gamma \ll \Gamma$, the electronic relaxation are relatively

fast, the four-photon process will not be effective and will be weak in comparison

to the ordinary Stokes scattering process. Hence only a small proportion of the

radiation generated has AS character.

D. STOKES AND ANTISTOKES OUTPUT POWER

We now obtain the output powers from (VI.20), (VI.15) and (IV.38) - (IV.39)

$$\bar{P}_{\substack{s \\ a}} = \frac{1}{4}\left\{\left((1+\tfrac{\gamma}{\Gamma})^{\frac{1}{2}}\pm 1\right)\right\}\left\{b_1 - \frac{\gamma\Gamma}{4\mu^2}\frac{1}{\bar{P}_p}(1+\tfrac{\gamma}{\Gamma})^{\frac{1}{2}}\right\}. \qquad \text{(VI.21)}$$

The left side of the above equations will be the actual rate of photon density

generation if $\bar{P}_p$ is taken to be $\dot{P}_{in}$, neglecting pump depletion. With (V.11)

we have

$$\bar{P}_{\substack{s \\ a}} = \frac{1}{8}\left\{(1+\tfrac{\gamma}{\Gamma})^{\frac{1}{2}}\pm 1\right\} \qquad \text{(VI.22)}$$

$$\times\left\{b_1 + \frac{2}{\beta\sqrt{1+\gamma/\Gamma}}\left[P_{in} - \sqrt{[P_{in}-\tfrac{\beta}{2}b_1(1+\tfrac{\gamma}{\Gamma})^{\frac{1}{2}}]^2 + \beta b_2\tfrac{\gamma\Gamma}{2\mu^2}(1+\tfrac{\gamma}{\Gamma})]}\right]\right\}$$

which reduces to (VI.21) with $\beta = 0$. It is straightforward to show that

$\partial\bar{P}_{\substack{s \\ a}}/\partial P_{in} > 0$ for $P_{in} > 0$. The threshold and saturated powers from (VI.22) are

$$(P_{in})_{th} = \frac{b_2}{b_1}\frac{\gamma\Gamma}{4\mu^2}\sqrt{1+\gamma/\Gamma} \qquad \text{(VI.23)}$$

$$\bar{P}_{\substack{s \\ a}}^{s} = \frac{b_1}{4}\left\{\sqrt{1+\gamma/\Gamma}\pm 1\right\}, \qquad \text{(VI.24)}$$

which are also the same as those obtained in the $\beta = 0$ case. Note that the

Stokes and AS outputs always have the same threshold. It is clear from (VI.23) -

(VI.24) that we must have the consistency conditions

$$b_1 > 0, \qquad b_2 > 0. \qquad \text{(VI.25)}$$

They will be discussed in more detail in subsection F. In Figure 2.10 we plot

the power output as a function of the input for both the cases of pump depletion

included and neglected. We see that unphysical results can occur in certain

regions of the input if pump depletion is neglected.

The dependence of the threshold requirement on the system parameters is intuitively reasonable. Compared with the standard formula, we have included the effect of detuning and more exact properties of the electronic systems. Formula (II.24) should be used to bring (VI.23) in close resemblance to the ordinary threshold equation. Equations (IV.37) and (VI.25) also allows clear indication of the limitations on the output powers which arise from the transition rates of the levels, and the difference pump rate. The saturation behavior will be further discussed in the next subsection.

We note that the photon number conservation is indeed obeyed

$$\bar{P}_s + \bar{P}_a = \frac{1}{4}\sqrt{1+\frac{\gamma}{\Gamma}}\left\{ b_1 + \frac{2}{\beta\sqrt{1+\gamma/\Gamma}} \right.$$

$$\left. \times \left[P_{in} - \sqrt{\left(P_{in} - \frac{\beta b_1}{2}\sqrt{1+\gamma/\Gamma}\right)^2 + \beta b_2 \frac{\gamma\Gamma}{2\mu^2}(1+\gamma/\Gamma)} \right]\right\}$$

$$= P_{in} - \bar{P}_p < P_{in}.$$

(VI.26)

E. CLOSED ELECTRONIC MODEL

We consider the following particular electronic model of interest. We set

$$R_D = R_S = 0$$

(VI.27)

$$\bar{S} = N$$

(VI.28)

so that each electron is allowed only on levels 1 and 2. In this case

$$b_1 = (\Gamma_{DS} - \Gamma_{SS}) N$$

$$b_2 = \Gamma_{DD} - \Gamma_{SD} .$$

(VI.29)

The total rate out can be written as

$$\Gamma_1 = W_{21} + \bar{n} A$$

$$\Gamma_2 = W_{12} + (\bar{n}+1) A$$

(VI.30)

where A is the radiative absorption rate and $\bar{n}$ is the number of thermal noise photons. The equilibrium situation is expressed by

$$\Gamma_1 N_1 = \Gamma_2 N_2$$

(VI.31)

so that

$$b_1 = (W_{12} - \Gamma_1) N$$

$$b_2 = W_{12} + \Gamma_1 .$$

(VI.32)

In most situations, the A's term in (VI.30) is small compared to the other rate.

If we substitute (VI.32) into the power equations (VI.23) - (VI.24), we obtain

$$(P_{in})_{th} = \frac{W_{12} + \Gamma_1}{W_{12} - \Gamma_1} \frac{\omega_s^2 n_s^3}{4\pi^2 c^3 L_1} \frac{1}{N(d\sigma/d\Omega)_s} \frac{\gamma\Gamma}{4} \left(1 + \frac{\gamma}{\Gamma}\right)^{\frac{1}{2}}$$

(VI.33)

$$\bar{P}^s_{s_a} = \frac{W_{12} - \Gamma_1}{4} N \left\{ \sqrt{1 + \frac{\gamma}{\Gamma}} \pm 1 \right\} .$$

(VI.34)

Equation (VI.33) can be compared with the ordinary threshold formula. The saturation behavior of (VI.34) allows a simple interpretation. Consider the special case $\Gamma_1 = 0$ and $\gamma \ll \Gamma$, we have

$$\bar{P}^s_s \approx \frac{W_{12} N}{2}$$

(VI.35)

This represents what one would intuitively expect the maximum output power to be. The power is limited by the rate of removing the level 2 electrons back to the lower level for the further Stokes scattering, and of course also by the actual number of scatterers available. The factor of two arises because the effective number of scatterers is $N/2$. This is due to the fact that after $N/2$ electrons has shifted to level 2 from level 1, the system can no longer operate without a positive D . This point also sheds light on why the transition rate out of level 2 is so important in the power saturation. Such considerations are closely connected with the idea of a fluorescence cycle to be discussed at present.

F. FLUORESCENCE CYCLE

For an ordinary laser to work effectively, it is clear that the lasing atoms should be able to circulate between the various relevent levels rapidly. The route of return of an atom to the upper state after lasing transition can be called the fluorescence cycle. In our case the fluorescence cycle corresponds to the return of electrons to level 1 after the scattering. If such routes are not always available, the system will not be able to lase. Mathematically the condition for the

existence of effective fluorescence cycle is expressed by the positiveness of the

output power. They are given in our case by (VI.25). Thus we require

$$R_D + \Gamma_{DS} R_S / \Gamma_{SS} > 0 \tag{VI.36}$$

$$\Gamma_{DD} - \Gamma_{SD} \Gamma_{DS} / \Gamma_{SS} > 0 \ .$$

This equation is easily interpreted in the case when (VI.20) applies. Thus we

have

$$W_{12} > \Gamma_1 \tag{VI.37}$$

which implies that the non-scattering transition rate from level 2 to level 1 has

to be faster than that from level 1 to 2. In the other situation we will clearly

pile up level 2 gradually, and the population difference will eventually vanish.

Stimulated processes will then stop altogether. Similar interpretations can be

given to (VI.36) with a more detailed consideration.

We have given a detailed analytic as well as physical description of the

steady state electronic Raman laser in this section, with the simplifying

assumption (VI.1) - (VI.3). Numerically results are easily obtained in the more

general case, but the quantitative insights obtainable in this special case are

certainly of general interest. It turns out that our formulas in this section

already provides an excellent quantitative description of the SFR lasers.

VII. COMPARISON WITH OTHER LASERS

Our specific results in the above section are based on the assumptions (VI.1) - (VI.3), and would not therefore go to the limit of no AS radiation with $\mu_a \to o$. Nevertheless it is straightforward to go through the same analysis and we will merely present the results here. Thus we set

$$\mu_a = o \tag{VII.1}$$

in equations (III.15) - (III.18). The frequency and momentum mismatch are now given by

$$\omega_p - \omega_e = \omega_s - \Delta\omega \tag{VII.2}$$

$$\vec{k}_p - \vec{k}_e = \vec{k}_s \quad . \tag{VII.3}$$

The phase matching condition (III.3) will be automatically satisfied, as in SRS from optical phonons. Making the change of variables,

$$E_s \longrightarrow E_s' \, e^{\,i k_s \delta - i(\omega_s - \Delta\omega)t} \tag{VII.4}$$

$$E_s' \longrightarrow E_s'' \, e^{\,i k \delta - i\omega t} \tag{VII.5}$$

We obtain as before

$$\bar{\omega} = - \frac{\Gamma}{\Gamma+\gamma} \, \Delta\omega \tag{VII.6}$$

$$\bar{D} = \frac{1}{\mu^3 P_p} \, \frac{\gamma\Gamma}{4} \left(1 + d^2 \right) \tag{VII.7}$$

$$d = \frac{2\Delta\omega}{\Gamma+\gamma} \tag{VII.8}$$

The Stokes output will oscillate at the well-known pulled frequency

$$\bar{\omega}_s = \frac{\gamma(\omega_o - \omega_e) + \Gamma \omega_s}{\Gamma + \gamma} \quad . \tag{VII.9}$$

The photon density generation rate is

$$\bar{P}_s = \frac{1}{2}\left\{ P_{in} + \frac{b_1}{2} - \sqrt{(P_{in} - \frac{b_1}{2})^2 + \frac{\gamma\Gamma}{2\mu^2} b_2 (1 + d^2)} \right\} . \tag{VII.10}$$

The quantities b_1 and b_2 are still given by (IV.36). The threshold and saturation $\bar{p}_s^r$ are therefore

$$(\bar{P}_{in})_{th} = \frac{\gamma\Gamma}{4\mu^2} \frac{b_2}{b_1} (1 + d^2) \tag{VII.11}$$

$$\bar{P}_s^s = \frac{b_1}{2} \quad . \tag{VII.12}$$

Equations (VII.8) and (VII.10) appear to be closely similar to the coupled St okes-AS case. The threshold differs from (VI.23) only by a different detuning factor. The saturation also has basically the same form and interpretation as (VI.24).

In most applications, $\mu_a \neq 0$ as may be seen from (VI.2). The AS radiation is therefore always present. However, in the perpendicular geometry of Figure 2.7, it is very small under the usual circumstance $\gamma \ll \Gamma$. In this configuration the momentum matching condition (IV.5) cannot be satisfied in any way, because of the constraints on $|k_s^o|$ and $|k_a^o|$. From (IV.9) - (IV.10) it is readily observed that this situation is mathematically described by $\Delta k \rightarrow \infty$. This can also be seen graphically by extrapolation of our Figure 2.5. The AS output power will then be small from (VI.22), but it may not be entirely negligible.

In this situation we should, strictly speaking, use our Stokes-AS formulation rather than the above purely Stokes results. The practical difference is of course insignificant.

We discuss briefly the difference of our system from the Raman laser based on SRS from phonons. [1]-[3] This has been mentioned in sections II and III. Here we would like to make the following point. In the ordinary case the equations of motion involve, upon elimination of the electron variables, only the radiation and phonon modes. We would have obtained a similar set of equations if we assume D to be a constant parameter in our equations. Retaining D as a variable results in a more general set of equations than those before. In particular this allows us to compute the steady state power behavior of the system, even when pump depletion is neglected. In the other case the equations are linearized by neglecting pump depletion, and so no steady state power output can be obtained. It is interesting to point out that the boundary value problem can be solved, and the steady state output can be obtained in that case with the help of our equation (V.11), which introduces the necessary nonlinearity.

Our laser can also be compared to an ordinary laser operating with a population inversion. The primary difference lies in the different way the pump enters the system, as well as the presence of AS radiation. This different pumping mechanism produces different output power behavior as a function of the pump. Some contrast in saturation and fluorescence cycle behavior has already been mentioned in section V. Detailed discussions on the power behavior of various lasing mechanisms, including SRS from collective and single-particle excitations, will

be reported elsewhere.

VIII. COMPARISON WITH EXPERIMENTS

We will not attempt any comprehensive comparison of our theory with

experiments here. We also will not discuss the various idealizations of our

theory in contrast to the experimental situations. Effects neglected in our treatment

which may have importance in the actual observations include inhomogeneous

broadening, multimode structure, backward Raman waves, input beam behavior,

higher order Stokes components, transient effects, fluctuation phenomena, as

well as other optical nonlinearities.

A great deal of experimental results are now available on the SFR laser. [4],[5],[7]-[9]

We will primarily compare only with a small fraction of these results here due to

space limitation. Consider the geometry of the experiment in the collinear

configuration of Figure 2.6. A CO_2 laser pump is scattered by a crystal of

n-InSb in a magnetic field, with most of its electrons in the lowest Landau level.

The parameters of the problem are determined experimentally, $(d\sigma/d\Omega)_s \cong 10^{-23} cm^2$, [4]

$\Gamma \cong$ 0.5 cm^{-1}, [17] $\alpha = 0.3$cm^{-1} [4], $R = 0.36$, [4] $n = 4$, $\tau_s = 1/W_{12} \cong 2 \times 10^{-8}$sec,

magnetic field H = 50 KG. In the experiments of Aggarwal, etc, [17] we have N =

2×10^{16}cm^{-3}, L = 2 cm. Some experimental and theoretical results are given

in Table 2.1. The Stokes and AS power behavior as a function of the input is plotted

in Figure 2.11 for the system but with N = 1.3 x 10^{16}cm^{-3} and L = 0.4 cm. The

theoretical curve is compared to experimental data. [5] There is excellent

agreement between experiments and our present theory.

Several uncertainties exist in the measured values which affect our theoretical answers. In particular the value Γ can lie somewhere between 0.4 and 0.5 cm^{-1}. The observed values of $(d\sigma/d\Omega)_s$ and τ_s can also be off by a factor of 2. Given these uncertainties and the fact that no adjustable parameters have been used, our theory can be considered to be in very close agreement with experiments.

Some important qualitative properties of our predictions are also well observed. For example the constancy of r as a function of input is roughly obeyed in Aggarwal, etc's experiment. It is obeyed much more closely in Figure 2.11. Equation (VI.16) predicts an r = 0.11. The difference between this r and the other r $\cong$ 0.03 is also in agreement with our theoretical prediction that a larger γ gives rise to higher r. From (V.6) we see that the longer crystal of Aggarwal, etc., results in a lower γ , even α is the same in both cases.

It is possible that the accuracy of our theory and the power measurements may together lead to better estimates of Γ and τ_s than before. Detailed quantitative discussions of SFR laser behavior and interpretations of available experimental results will be given in a future publication.

IX. DISCUSSIONS

Some comments on the nature of our results are in order. Many realistic features of the experimental situations such as those mentioned in the above

section are neglected in our theory, in addition to the approximations made to arrive at the analytic results. This should always be kept in mind in applying our results to specific problems, although it appears from the above comparison that our assumptions are very good in the SFR laser case. In particular it is known that nonlinear effects like self-focusing is not important in n-InSb,[10] in the parameter range of interest.

Besides the detailed understanding and checking on the experimental observations, our theoretical results are also useful in the general planning of an experiment. For example, they indicate the limiting factors for obtaining large output power. In general one can draw the conclusion from (V.6) and (VI.22) that a large crystal subjected to condition (V.8) is preferred, both for getting a lower threshold and higher output power. By examining the rate constants involved one will also be able to tell whether a fluorescence cycle will perpetuate. If one is interested in maximizing the output power, in particular the AS output, one can examine (VI.22) and choose the controllabel parameter such as R accordingly. If one is interested in maximizing the efficiency

$$\eta = \frac{\bar{P}_s}{P_{in}}$$

(IX.1)

one can similarly choose the relevant constants. As a function of P_{in} , for example, the efficiency attains its maximum at

$$P_{in} = \left(2 + \frac{b_1^2}{b_2} \frac{\mu^2}{\gamma T} \right) P_{th} .$$

(IX.2)

Similar use can be made for other considerations.

Our results also suggest the following interesting possible application. As we mention before, we can use accurate power measurements to determine, via our formulas, the various parameters of the scattering system. For example the saturated power gives a good indication of the relaxation rate. Thus new information may be obtained on the various non-equilibrium transition rates of the electronic system. With further analysis of more general scatterer model or with detailed observations of the scattering output, additional information on the scatterer is also possible.

Finally we note that further experimental observations for testing the detailed predictions of our theory should be worth undertaking.

X CONCLUSIONS

We have constructed a general theory of an electronic Raman laser which is described by ten coupled equations of motion. The steady state laser behavior is treated in detail. Closed-form analytic results are obtained, which are also interpreted physically. Since the other optical nonlinearities are not important in the spin-flip Raman laser, our results are in striking confirmation with experimental observations.

In future publications we hope to extend our treatment to include effects of inhomogeneous broadening, backward Raman waves, multimode structures, as well as higher order Stokes and Anti-Stokes components. We also hope to consider the transient behavior, the stability of the steady state, and the quantum

statistics of the output radiations. Our theory is also useful in the exploration

of new mechanisms for obtaining coherent, tunable optical radiation.

EXPERIMENTAL	THEORETICAL	
$r \cong 0.03$	$r = 0.032$	(VI.16)
$I_{th} \cong 4.0 \times 10^4 \ W/cm^2$	$I_{th} = 5.0 \times 10^4 \ W/cm^2$	(VI.20) (V.4)
$I_s^s \cong 2.2 \times 10^4 \ W/cm^2$	$I_s^s = 4.0 \times 10^4 \ W/cm^2$	(VI.21) (V.5)

Table 2.1   List of values from calculations and experiments.[7] Equations from which the theoretical value is obtained are indicated to the right.
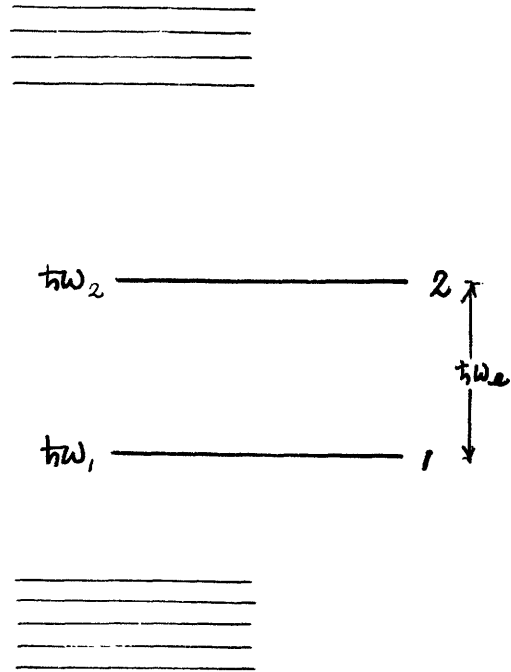
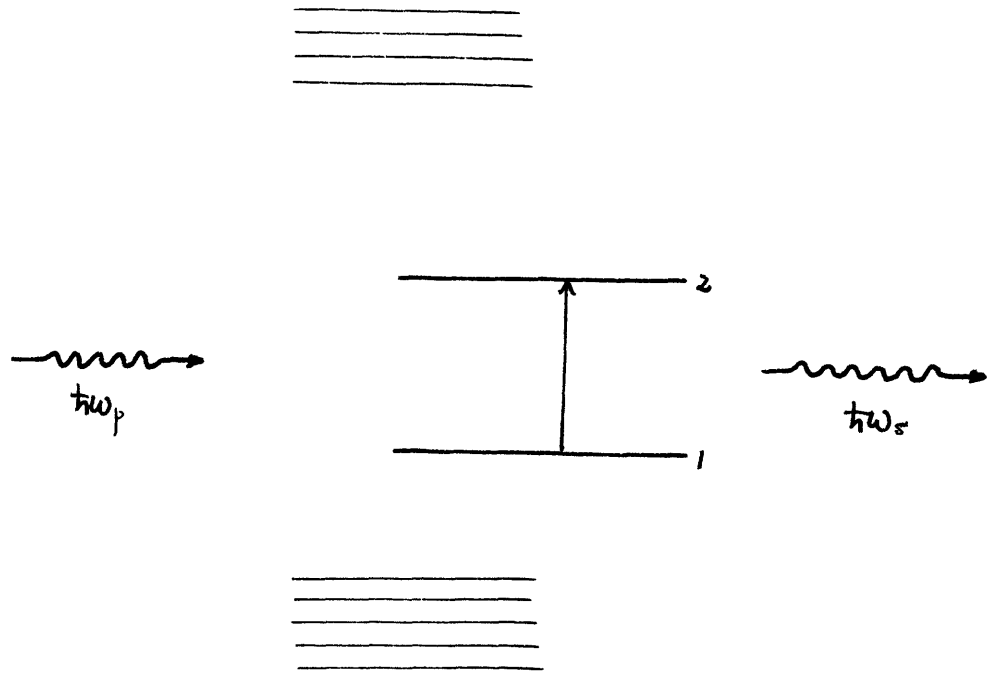Figure 2.1a   Energy level of an electron.

Figure 2.1b   Raman scattering with direct electronic
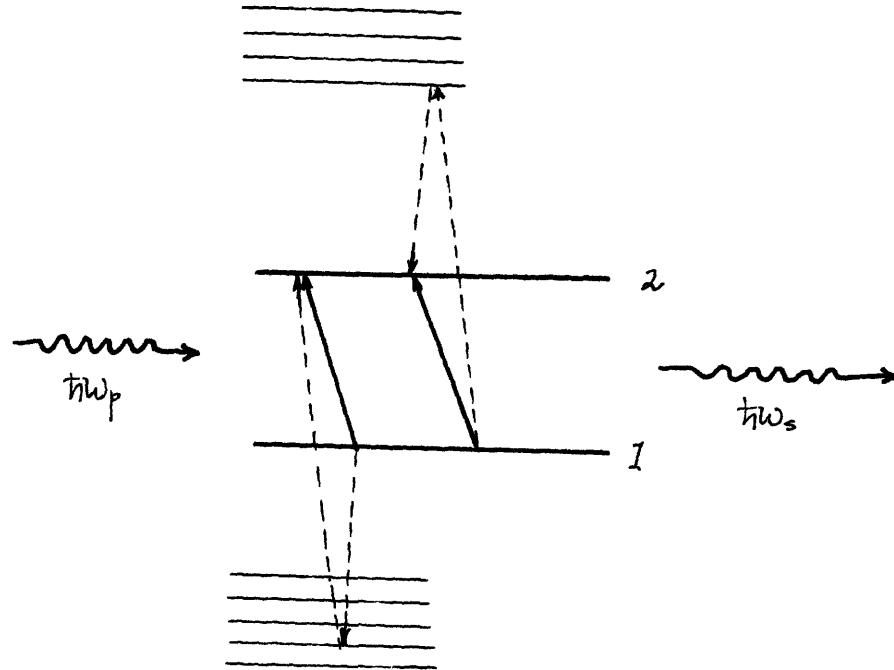excitation from level 1 to level 2.

Figure 2.1c   Raman scattering with initial electron state 1
and final state 2 through an intermediate state; virtual tran-
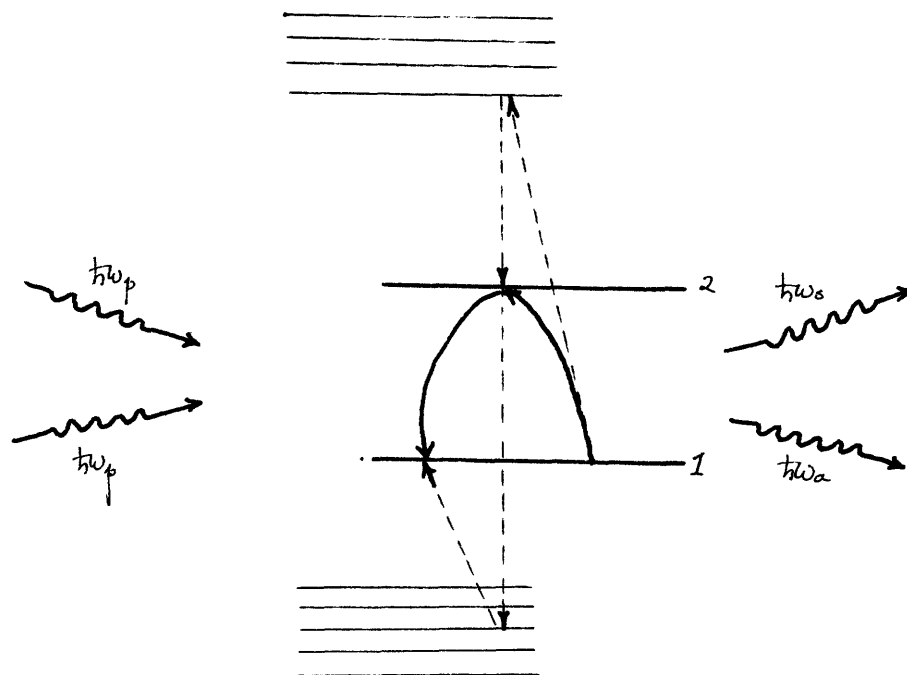sitions are denoted by dash-lines.

Figure 2.2   Coherent four-photon process with no final
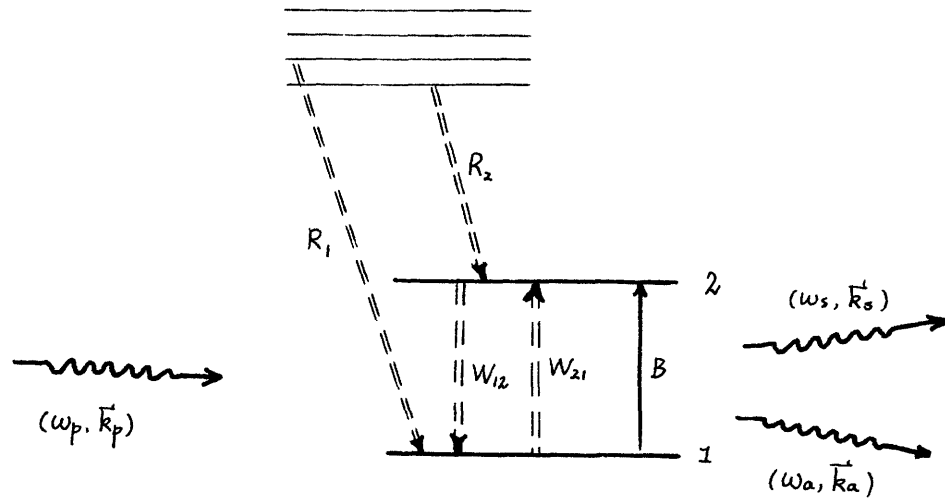electron state change.

Figure 2.3   The transition rate behavior of an electron.
The double-dash-line indicates non-scattering transitions.

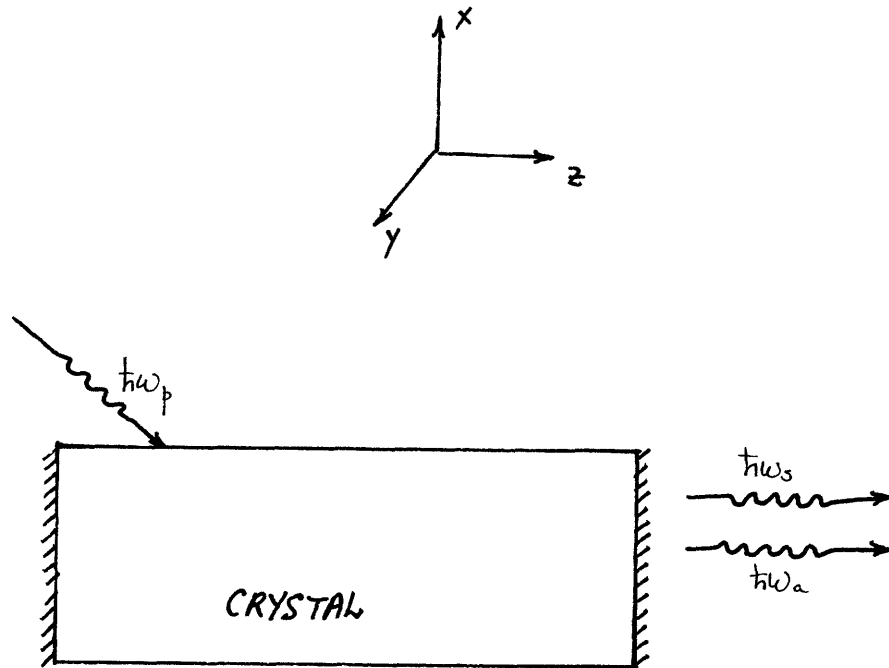Figure 2.4 Traveling wave boundary condition excitation of the Raman medium.

Figure 2.5   Phase matching between the pump, the Stokes, and the anti-Stokes radiations.
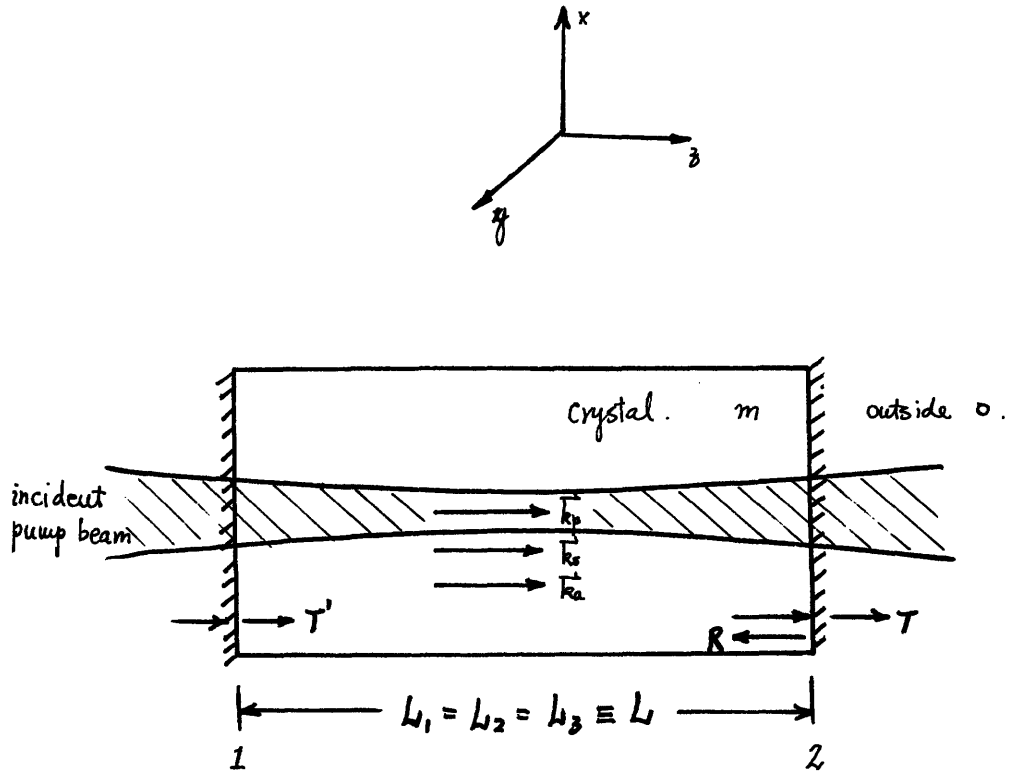
Figure 2.6   Traveling wave boundary excitation in the $\vec{q}.\vec{B} = 0$ collinear geometry.
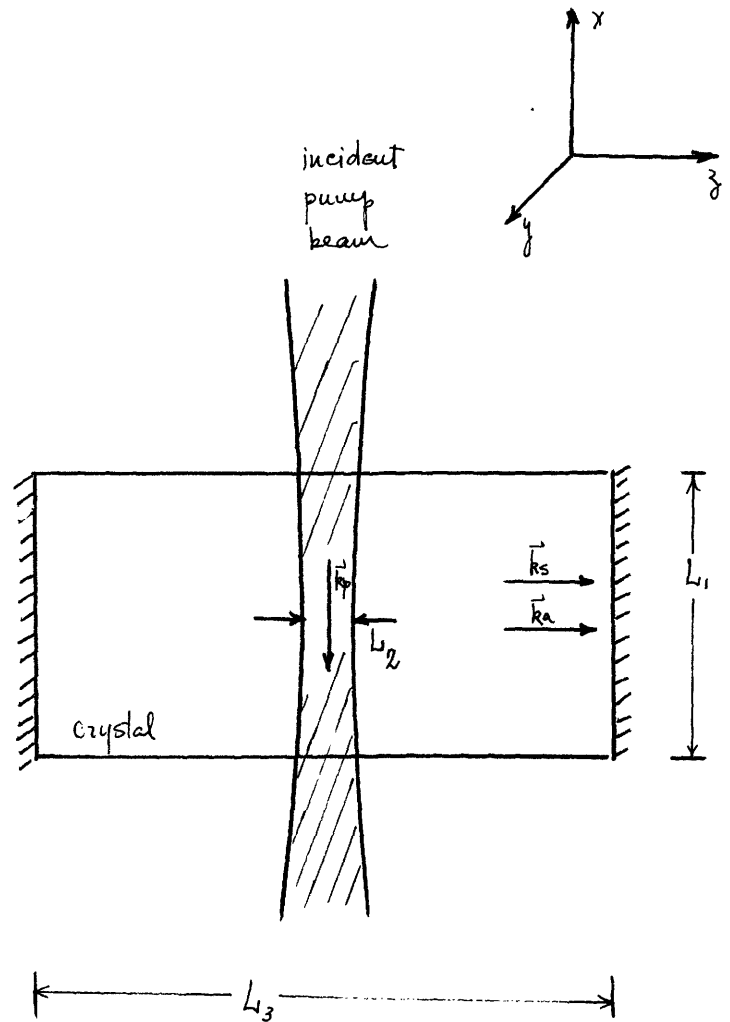
Figure 2.7 Traveling wave boundary excitation in the $\vec{q}.\vec{B} = 0$ non-collinear geometry. This gives rise to three different characteristic lengths L_1, L_2, L_3.
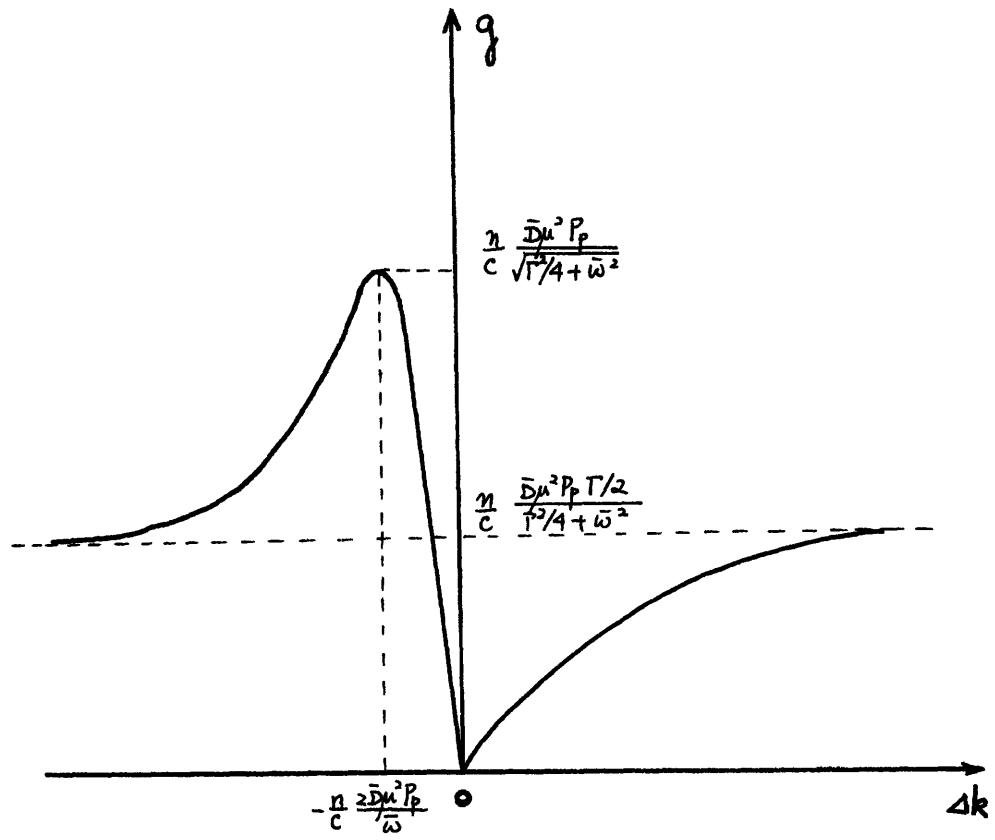
Figure 2.8   Gain coefficient as a function of momentum mismatch Δk.
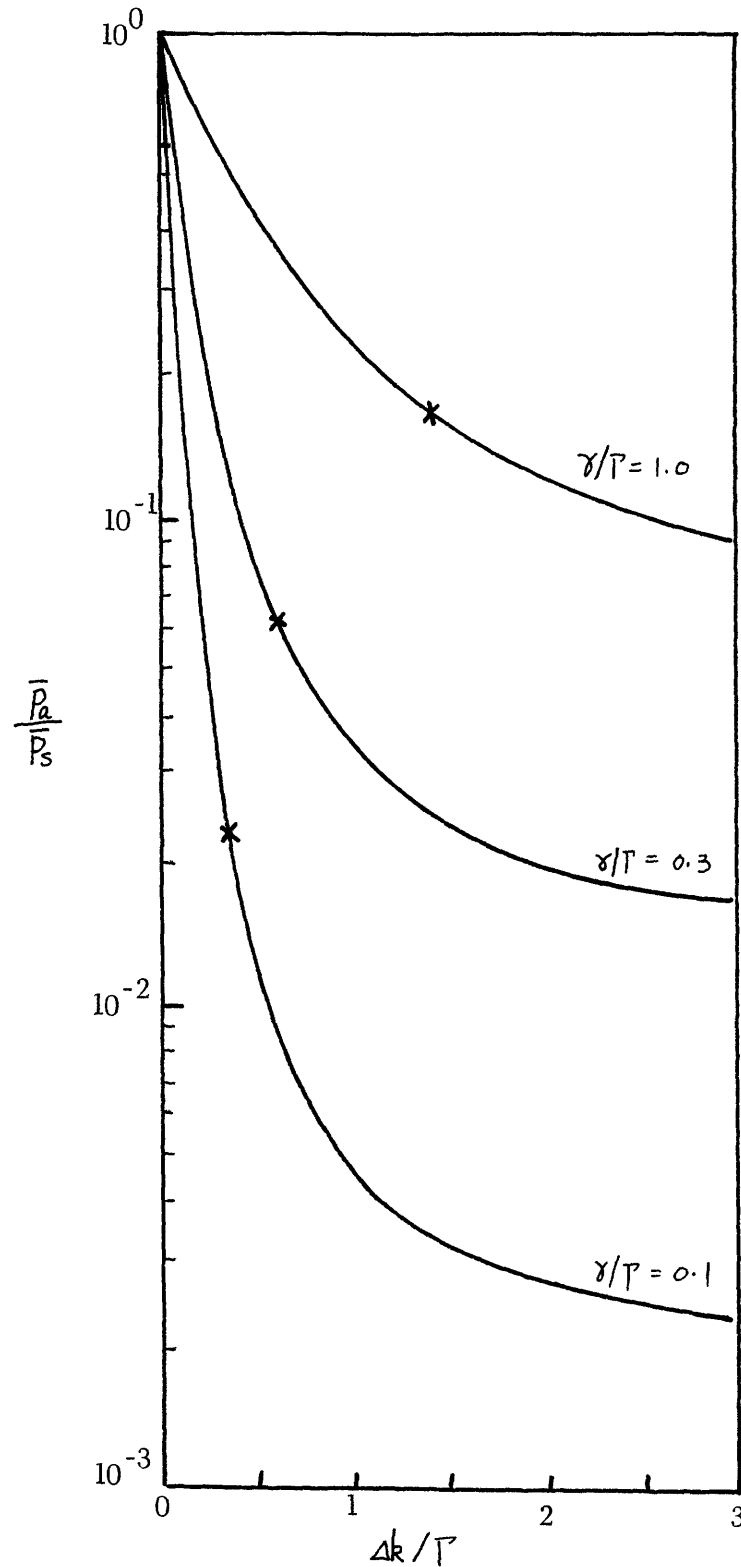
Figure 2.9   Ratio of Stokes and anti-Stokes photon generation rate in the steady state;   the x's indicate the values at maximum gain.
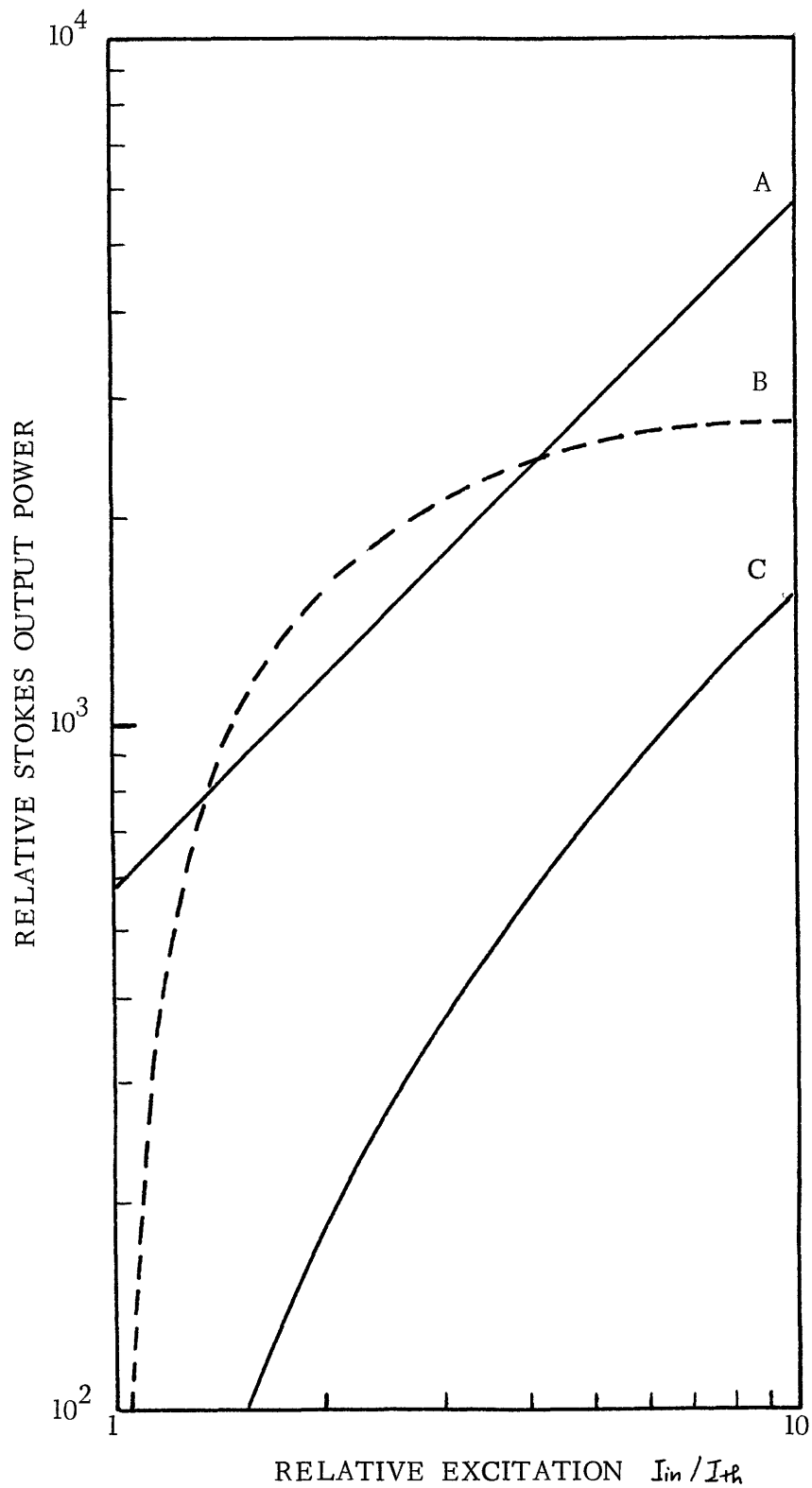
Figure 2.10   Logarithmic plot of the Stokes output power as a function of input power;   Curve A corresponds to the input power, curve B to the Stokes power neglecting pump depletion, curve C to the Stokes power with pump depletion.   Power conservation is violated in a certain range of input in case B.
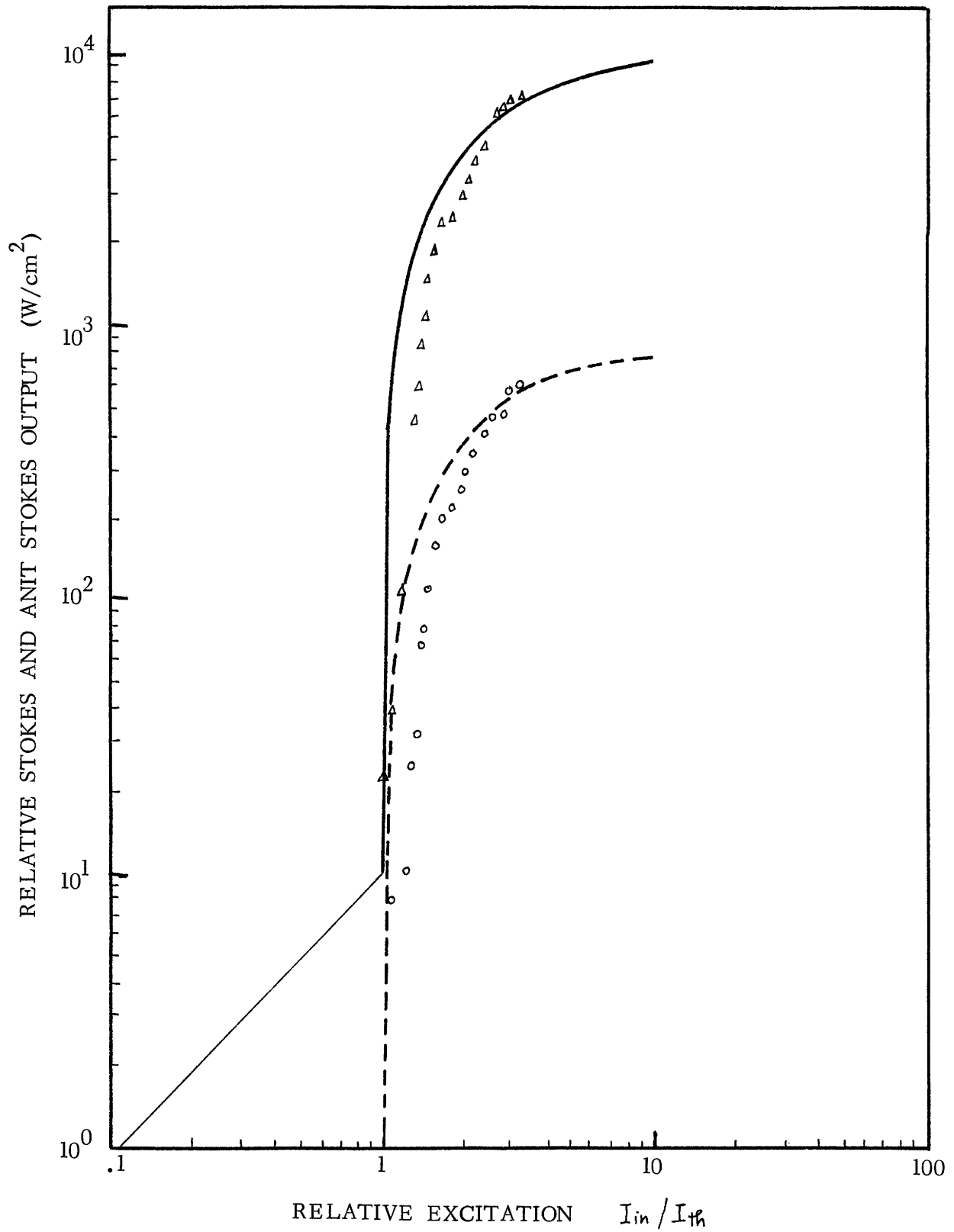
Figure 2.11 Stokes and anti-Stokes output as a function of pump input. The circles are experimental results from reference 7. The curves are obtained from equations (VI.22) and (VI.32).

REFERENCES

(1)   For a recent review with extensive references see N. Bloembergen, Amer. J. Phys., 35, 989 (1967)

(2)   Y.R. Shen and N. Bloembergen, Phys. Rev. 137, A1787 (1965)

(3)   N. Bloembergen, Nonlinear Optics, W.A. Benjamin, Inc., New York, 1965

(4)   C.K.N. Patel and E.D. Shaw, Phys. Rev. Lett. 24, 451 (1970)

        C.K.N. Patel and E.D. Shaw, Phys. Rev. B3, 1279 (1971)

(5)   E.D. Shaw and C.K.N. Patel, Appl. Phys. Lett. 18, 215 (1971)

        C.K.N. Patel, Appl. Phys. Lett. 18, 274 (1971)

        C.K.N. Patel, Appl. Phys. Lett. (to be published)

(6)   C.K.N. Patel, E.D. Shaw and R.J. Kerl, Phys. Rev. Lett. 25, 8 (1970)

        L.B. Kreuzer and C.K.N. Patel, Appl. Phys. Lett. (to be published)

(7)   R.L. Aggarwal, B. Lax, C.E. Chase, C.R. Pidgeon, D. Limbert, and F. Brown, Appl. Phys. Lett. 18, 383 (1971)

(8)   A. Mooradian, S.R.J. Brueck, and F.A. Blum, Appl. Phys. Lett. 17, 481 (1970); S.R.J. Brueck and A. Mooradian, Appl. Phys. Lett. 18, 229 (1971)

(9)   R.L. Allwood, S.D. Devine, R.G. Mellich, S.D. Smith, and R.A. Wood, J. Phys. C3 L186 (1970); R.I. Allwood, R. Dennis, S.D. Smith, B. Wherett, and R.A. Wood, J. Phys. C (to be published)

(10)   N. Tzoar and J. Gersten, Phys. Rev. Lett. 26, 1634 (1971)

(11)   We follow mostly the notations of M. Lax, Phys. Rev. 145, 110 (1966), and M. Lax and H. P. Yuen, Phys. Rev. 172, 362 (1968). Some changes have however been made. A detailed discussion of quantum descriptions

of multi-level systems can be found in M. Lax, in <u>Brandeis University</u> <u>Summer Lectures in Theorectical Physics,1966.</u> Vol. 2, Gordon and Breach, New York, 1968.

(12)   M. Maier, W. Kaiser and J.A. Giordmaine, Phys. Rev. <u>177</u>, 580 (1969).

(13)   R.J. Glauber, Phys. Rev. <u>130</u>, 2529 (1963); 131, 2766 (1963)

(14)   I.I. Rabi, N.F. Ramsey and J. Schwinger, Rev. Mod. Phys. <u>26</u>, 107 (1954)

(15)   See, e.g., L.I. Shiff, <u>Quantum Mechanics,</u> McGraw-Hill, N.Y., 1955

(16)   See, e.g., reference (11), and P.N. Argyres, in <u>Colorado Summer</u> <u>Lectures in Theoretical Physics</u>, Vol VIIIA, University of Colorado Press, Boulder, 1966; and references therein.

(17)   N.M. Kroll and P.L Kelley, Phys. Rev. A<u>4</u>, 763 (1971)

(18)   S.R.J. Brueck, PH.D. thesis submitted to the Department of Electrical Engineering, M.I.T., Cambridge, Mass., August, 1971

CHAPTER 3

MAGNETIC FIELD TUNED SPIN-FLIP RAMAN LASER

I. INTRODUCTION

In this chapter the theories developed in the previous chapters will be applied to the spin-flip Raman (SFR) laser tunable in the infrared by a magnetic field. The linewidth Γ calculated in Chapter 1 is taken as a parameter which, together with other parameters to be calculated in the subsequent sections, will be substituted into the formulas of Chapter 2 to yield the behaviors of the stimulated SFR scattering. The results will then be compared to available experimental data on the InSb SFR laser.

The main parameters that takes care of the magnetic field, carrier concentration, and temperature dependence of the Raman laser are the spontaneous linewidth Γ , which accounts for the experimental geometry and electron statistics; the total cross section $(d\sigma/d\Omega)_T$, in which is buried the polarization characteristics of the electromagnetic waves; and the loss γ , which depends on B , N as well as T . In section II, we will investigate the validity of applying the Γ calculated in Chapter 1 to describe the SFR laser by the homogeneously broadened Raman laser theory of Chapter 2. In section III, the cross section and its dependence on B , N and T are calculated, where statistics effects are also considered in particular. The

losses are discussed in section IV and the results of these three sections will be combined in section V to derive the behavior of the SFR laser, including detailed threshold conditions, power output and saturation.

II. INHOMOGENEOUS BROADENING

All the stimulated SFR scattering experiments are performed in the $\vec{q}.\vec{B} = 0$ geometry discussed in Chapter 1. In this geometry the main broadening mechanism for the spontaneous lineshape is nonparabolicity of the energy bands, where the electrons have different g-values and hence different frequency shifts. We encounter therefore the situation of an inhomogeneous broadened line. We will show that the electronic Raman laser theory of Chapter 2, which is valid for a Lorentzian spontaneous line, does apply under certain approximations to stimulated SFR scattering in InSb with inhomogeneous line-shape. We will only present here a simple arguement establishing the validity of equations (III.15) - (III.20) of Chapter 2. Development of a Raman laser theory including inhomogeneous broadening is a separate problem, and will be reserved for future works. Except for the Lamb dip [o] effect, a more complete treatment will give results similar to our present ones.

Consider N two level electronic systems, the energy separation of the jth being

$$\hbar\omega_{2j} - \hbar\omega_{1j} = \hbar\omega_j \quad . \tag{II.1}$$

The Hamiltonian for each electron is

$$H_j = \hbar\omega_{2j} a_{2j}^{+} a_{2j} + \hbar\omega_{1j} a_{1j}^{+} a_{1j} \quad . \tag{II.2}$$

We define

$$M_j = a_{1j}^{+} a_{2j} \quad , \qquad M = \sum_j M_j \tag{II.3}$$

$$N_{1j} = a_{1j}^{+} a_{1j} \quad , \qquad N_1 = \sum_j N_{1j} \tag{II.4}$$

$$N_{2j} = a_{2j}^{+} a_{2j} \quad , \qquad N_2 = \sum_j N_{2j} \quad ,$$

and

$$N_{1j} - N_{2j} = D_j \quad ; \qquad D = \sum_j D_j \quad . \tag{II.5}$$

Since the two level systems are closed, we have

$$N_{1j} + N_{2j} = 1 \quad . \tag{II.6}$$

Using (II.1) - (II.6) we have, parallel to the derivation of (2.III.18) - (2.III.20) (in Chapter 2),

$$\frac{\partial M_j}{\partial t} = - \left(\frac{\Gamma_s}{2} + i\omega_j \right) M_j - i\sqrt{\gamma_q} \, D_j \left(\mu_s E_p E_s^* + \mu_a E_p E_a \right) \tag{II.7}$$

$$\frac{\partial D_j}{\partial t} = \Gamma_{DS} - \Gamma_{DD} D_j - 2 B_j \tag{II.8}$$

where

$$B_j = i\sqrt{\gamma_q} \, \mu_s \left(E_p^* E_s M_j - E_p E_s^* M_j^* \right) + i\sqrt{\gamma_q} \, \mu_a \left(E_p^* E_a M_j^* - E_p E_a M_j \right) \quad , \tag{II.9}$$

In (II.7), Γ_s' is the spin relaxation rate $T_s' = 2/T_s$, all other constants and operators used in (II.7) - (II.9) are defined in Chapter 2.

Equation (II.8) can be summed over j to give at once equation (2.III.19) but the M_j equation presents difficulty because of the $\omega_j M_j$ term. However, from (2.III.19) we can see that the population difference D is built up mainly by the radiative transition, which in the steady state is given by (2.IV.34)

$$ \bar{B} = \bar{P}_s - \bar{P}_a . $$
(II.10)

From Chapter 2 we see that $\bar{P}_a$ is usually an order of magnitude smaller than $\bar{P}_s$, and that $\bar{P}_s$ has a saturation value given by (2.VI.35)

$$ \bar{P}_s^s \cong \tfrac{1}{2} W_{12} N . $$
(II.11)

Thus the rate of radiative transition which creates the population difference is bounded by W_{12} . From Chapter 1 we see that this rate is much slower than the orbital collision rate which brings electrons from one state to another with the same spin, as $\tau_s \lessapprox W_{12}^{-1} \cong 10^{-8}$ seconds, compared to the electron-electron collision time $\tau_p = 10^{-10}$ sec. In such long time interval τ_s , the orbital collision will essentially wash out the inhomo-geneous effect, and we may regard D_j in (II.7) as a constant independent of j. Thus, in the steady state, (II.7) can be solved to give the polarization of the j-th electron,

$$ M_j = - \frac{i\sqrt{2}\, D\, (\mu_s \xi_p E_s^* + \mu_a \xi_p E_a)}{T_s/2 + i\,(\omega_j - \omega)} $$
(II.12)

Since only the $\omega_j^{\cdot}$'s are involved in the summation of (II.14), we can replace the sum by an integral over a distribution of $\omega_j^{\cdot}$. The actual distribution of $\omega_j^{\cdot}$ can now be taken from the spontaneous lineshape calculation in Chapter 1. Here, we will further approximate the lineshape to be a Lorentzian centering at $\hbar\omega_e = \mu_B g_\circ B$ with width Γ , Γ being the width of the actual spontaneous spectrum. This is a reasonable approximation in view of the experimental observed lineshape discussed in Chapter 1. Equation (II.12) thus becomes

$$ M = -i\sqrt{\tau_g}\left\{ \mu_s E_p E_s^* + \mu_a E_p E_a \right\} $$

$$ \times \int d\omega_j \frac{\Gamma/2}{(\Gamma/2)^2 + (\omega_j - \omega_e)^2} \frac{1}{\Gamma_s/2 + i(\omega_j - \omega)} \qquad \cdot \qquad (II.13) $$

From Chapter 1 we see that $\Gamma \gg \Gamma_s$. A contour integral of (II.16) will give at once

$$ M = i\sqrt{\tau_g} D (\mu_s E_p E_s^* + \mu_a E_p E_a) \frac{1}{\Gamma/2 + i(\omega_e - \omega)} \qquad (II.14) $$

which gives exactly the same result if M is solved by using equation (2.III.18).

Thus we see that the results of Chapter 2 can be applied to our case of inhomogeneous broadening in InSb SFR scattering. We are therefore able to apply our results of Chapters 1 and 2 directly to the SFR laser without any modifications. Further extensions of our treatment to include various features left out here will be carried out in the future.

III. TOTAL CROSS SECTION

Here we will consider the total cross section $(d\sigma/d\Omega)_T$ in the $\vec{q} \cdot \vec{B} = 0$ geometry. In principle $(d\sigma/d\Omega)_T$ is given by integrating equation (1.III.20) over all frequencies ω. In this section we shall make some approximations to obtain analytic results that will show the magnetic field, carrier concentration and temperature dependence of the cross section. We will use the free magnetic density of states (1G.3), and approximate $\gamma_0^{\#}$ to be independent of the quantum numbers n and k_3. Thus we can write in general

$$\left(\frac{d\sigma}{d\Omega}\right)_T = \left(\frac{e^2}{mc^2}\right)^2 \frac{2|\gamma_0|^2}{(2\pi)^3} \frac{\omega_k}{\omega_p} \frac{eB}{\hbar c} \sum_{n=0}^{n_{max}} \int dk_3 \, f[\mathcal{E}(nk_3) - \frac{\hbar\omega_s}{2}]\{1 - f[\mathcal{E}(nk_3) + \frac{\hbar\omega_s}{2}]\} \quad (III.1)$$

with γ_0 defined in (1.II.10) and

$$\mathcal{E}(nk_3) = n\hbar\omega_c + \frac{\hbar^2 k_3^2}{2m^*} \quad .$$

_____

\# This γ_0 is the Raman matrix element, and should not be confused with the optical loss γ .

The total cross section in (III.1) is the product of two terms

$$\left(\frac{d\sigma}{d\Omega}\right)_T = N_{eff} \left(\frac{d\sigma}{d\Omega}\right)_s . \tag{III.2}$$

$(d\sigma/d\Omega)_s$ in (III.2) is the single particle cross section defined by

$$\left(\frac{d\sigma}{d\Omega}\right)_s = \left(\frac{e^2}{mc^2}\right)^2 \frac{\omega_f}{\omega_p} |\gamma_o|^2 . \tag{III.3}$$

This is the quantity calculated by many people before.[1]-[5] As expected, $(d\sigma/d\Omega)_s$ is independent of N and T , but it can and does depend on the magnetic field through γ_o . An analytic expression of γ_o for the SFR scattering is given by Yafet[2] to first order in B , while Wright,[4] etc., carried out a numerical calculation for γ_o . Their results show a cross section quite independent of B . However, in previous works, conduction band intermediate states have been neglected, these intermediate states cause a cancellation of the cross-section for InSb at around 85 KG when $\hbar\omega_p \simeq \hbar\omega_c$. This effect is observed in stimulated SFR scattering experiments. Brueck[5] has given a numerical computation for $(d\sigma/d\Omega)_s$ taken into account these effects for SFR scattering in InSb with a CO laser, which has a strong resonance enhancement hactor. Using the wavefunctions in Yafet,[2] we have calculated numerically $(d\sigma/d\Omega)_s$ for SFR scattering in InSb with a CO_2 laser, and the result is plotted in Figure 3.1 as a function of magnetic field.

Polarization selection rules are also accounted for in γ_o . It has been shown by previous workers that for the $\vec{q}.\vec{B} = 0$ geometry discussed in Chapter 1, the only allowed polarization for the SFR scattering are $(Z,-)$ and $(+,Z)$, where Z refers to the electric field polarized along the magnetic field direction, and

± refers to circularly polarized electric fields. The first term in the polarization refers to the incident wave and the second to the scattered waves. Thus we see that if either the incident or the scattered electric field is polarized along B , the other must be polarized transverse to it.

The effective number of electrons that can be scattered is

$$N_{eff} = \frac{2}{(2\pi)^2} \frac{eB}{\hbar c} \frac{1}{1-e^{-\hbar\omega/k_BT}} \sum_{n}^{n_{max}} \int dk_3 \left\{ f[\varepsilon(nk_3) - \frac{\hbar\omega_s}{2}] - f[\varepsilon(nk_3) + \frac{\hbar\omega_s}{2}] \right\} \quad (III.4)$$

N_{eff} takes into account electron statistics and only through it can the total cross section be dependent on N and T . Wherett and Harper [7] has calculated N_{eff} in the limit of zero temperature and high magnetic field. We will give here expressions for N_{eff} valid for finite temperatures as well as all B, N values. (note that this calculation for N_{eff} given here is completely general, and can be applied, for example, to the SFR scattering in CdS).

First consider the low temperature limit. For $k_BT \ll \varepsilon_F$, an expansion of the Fermi integral in (III.4) gives [7]

$$N_{eff} \cong \frac{2}{(2\pi)^2} \frac{eB}{\hbar c} \left(\frac{2m^*}{\hbar^2}\right)^{1/2} (\bar{n}_\omega + 1)$$

$$\times \sum_{n}^{n_{max}} \left\{ \sqrt{\varepsilon_F - n\hbar\omega_c + \hbar\omega_s/2} - \sqrt{\varepsilon_F - n\hbar\omega_c - \hbar\omega_s/2} \right. \quad (III.5)$$

$$\left. - \frac{1}{24}(\pi k_BT)^2 \left[(\varepsilon_F - n\hbar\omega_c + \hbar\omega_s/2)^{-3/2} - (\varepsilon_F - n\hbar\omega_c - \hbar\omega_s/2)^{-3/2} \right] \right\}$$

where ε_F is the Fermi energy. To yield the correct B , N and T

dependences of N_{eff} , the variation of $\mathcal{E}_F$ with these parameters must be taken into account. A calculation of $\mathcal{E}_F$ for finite temperature in a magnetic field is given in Appendix 3B. Equation (III.5) shows that N_{eff} is an oscillatory function of B and N , as more and more Landau levels are occupied with increase N and $1/B$.

In the quantum limit, $n_{max} = 0$, so that (III.5) at once yields an expression for N_{eff} . When several Landau levels are occupied, we can use the Euler Maclaurin summation formula [10] to give a close from expression for N_{eff} . The Euler Maclaurin formula is discussed in Appendix 3A, keeping only two terms in equation (3A.1), we get

$$N_{eff} \simeq \frac{2\sqrt{2}}{(2\pi)^2} \left(\frac{eB}{\hbar c}\right)^{3/2} (\bar{n}_\omega + 1)$$

$$\times \left\{ \frac{2}{3}\left[\left(\frac{\mathcal{E}_F + \hbar\omega_s/2}{\hbar\omega_c}\right)^{3/2} - \left(\frac{\mathcal{E}_F - \hbar\omega_s/2}{\hbar\omega_c}\right)^{3/2} + \frac{3}{4}\left(\frac{\mathcal{E}_F + \hbar\omega_s/2}{\hbar\omega_c}\right)^{1/2} - \frac{3}{4}\left(\frac{\mathcal{E}_F - \hbar\omega_s/2}{\hbar\omega_c}\right)^{1/2}\right] \right. \quad \text{(III.6)}$$

$$\left. - \frac{(\pi k_B T)^2}{12}\left[-\left(\frac{\mathcal{E}_F + \hbar\omega_s/2}{\hbar\omega_c}\right)^{-1/2} + \left(\frac{\mathcal{E}_F - \hbar\omega_s/2}{\hbar\omega_c}\right)^{-1/2} + \frac{1}{4}\left(\frac{\mathcal{E}_F + \hbar\omega_s/2}{\hbar\omega_c}\right)^{-3/2} - \frac{1}{4}\left(\frac{\mathcal{E}_F - \hbar\omega_s/2}{\hbar\omega_c}\right)^{-3/2}\right] \right\}.$$

The error ϵ at T = 0 for (III.6) is given , by using (3A.5),

$$\frac{1}{24}\sqrt{\frac{\hbar\omega_c}{\mathcal{E}_F + \hbar\omega_s/2}} \quad < \quad \epsilon \quad < \quad \frac{1}{12}\sqrt{\frac{\hbar\omega_c}{\mathcal{E}_F + \hbar\omega_s/2}} \quad \text{(III.7)}$$

which can be compared with the leading term

$$\frac{2}{3}\left(\frac{\mathcal{E}_F + \hbar\omega_s/2}{\hbar\omega_c}\right)^{3/2}.$$

With two Landau levels occupied, $\mathcal{E}_F = 2\hbar\omega_c$, the error is seen to be

within 10%. The error will be considerably smaller when more Landau levels are occupied. In Figure 3.2, the total cross section is plotted as a function of magnetic field, and the experimental data are taken from Patel.[11]

At high temperature, $k_B T \gg \mathcal{E}_F$, we may approximate $f(\mathcal{E})$ in (III.1) by the Boltzmann distribution. The integration over k_3 and summation over n can then be carried out exactly to give

$$N_{eff} = \frac{N}{2\cosh(\hbar\omega_s/2k_B T)}$$

$$\times \left\{ e^{\hbar\omega_s/2k_B T} - N\pi^2 \left(\frac{\hbar^2}{\pi m^* k_B T}\right)\frac{\hbar c}{eB} \frac{\tanh(\hbar\omega_c/2k_B T)}{\cosh^2(\hbar\omega_s/2k_B T)} \right\} .$$

(III.8)

IV. LOSSES

A third parameter we need to know in our Raman laser theory is the optical loss in the Raman cavity γ . There are two main loss mechanisms as discussed in Chapter 2. The first is the bulk free-carrier absorption loss α whose dependence on magnetic field can be obtained from the complex dielectric constant[12]

$$\mathcal{E}(\omega) = \mathcal{E}_\infty \left\{ 1 + \frac{\omega_p^2 [\omega_p^2 - \omega^2(1-i\eta)]}{\omega^2 [(\omega_p^2 - \omega^2(1-i\eta))(1-i\eta) + \omega_c^2]} \right\}$$

(IV.1)

where ϵ_∞ is the high frequency dielectric constant, $\eta = 1/\omega\tau$ and

$$\omega_p = \left(\frac{4\pi N e^2}{m^* \epsilon_\infty}\right)^{1/2} \tag{IV.2}$$

is the Plasma frequency. The variation of the free carrier absorption α in n-InSb as a function of magnetic field and carrier concentration is given by Patel and Shaw, [13] and their results are reproduced in Figure 3.3. It shows that for a carrier concentration $N \leq 3 \times 10^{16}$ cm^{-3}, the free carrier absorption is relatively field independent for $B \leq 50$KG.

A second contribution to γ comes from the reflection loss on the cavity. This loss is independent of B, N and T, but it depends on the reflectivity of the cavity mirror as well as the cavity length. The total loss is given by

$$\gamma(\omega) = \frac{2c}{\eta_\omega}\left(\alpha(\omega) - \frac{\ln R}{L}\right) \tag{IV.3}$$

where η_ω is the refractive index for frequency ω, $\alpha(\omega)$ the free carrier absorption, R the reflectivity of the mirror and L the cavity length.

V. STIMULATED EMISSION

By using the parameters of the preceeding sections in the Raman laser theory of Chapter 2, we can now examine the behavior of stimulated spin flip scattering in InSb. The main purpose of the present treatment is for compari-

son with existing experiments. There are many experimental works devoted

to the SFR laser, all using InSb. Patel, etc.,[11],[13],[14],[15] and Allwood, etc.[16]

used a CO_2 laser as a pump source in the $\vec{q}.\vec{B} = 0$ noncollinear geometry dis-

cussed in Figure 2.7 to obtain stimulated Stokes radiation tunable from $\sim 11.7\mu$

$- \sim 13\mu$. In the same geometry, Mooradian, etc.[17],[18] used a CO laser

pump to achieve lower threshold and higher conversion efficiency. Stimulated

anti-Stokes radiation was reported by Patel, etc,[19] Allwood, etc.,[20]

and Aggarwal, etc. [21] with their experiments carried out in the $\vec{q}.\vec{B} = 0$

collinear geometry of Figure 2.6. We will try to compare our theories with

these experiments. Second Stokes emissions are also observed,[21],[22] we will

however not consider this here.

First we will investigate the threshold condition. The formulas for the

input threshold power $(I_{in})_{th}$ is given by equation (2.VI.30) together with

(2.V.7) and (2.V.4). With $T_1 \simeq 0$ in (2.VI.30), $\Gamma = 0.5$ cm^{-1},

(see Chapter 1) and a reflectivity R = 36% as given by the natural reflectivity

of InSb, the threshold power for different experimental configurations are given

along with their respective characterizing parameters in Table 3.1. A very

good agreement between theoretical and experimental results are obtained.

The low thresholds obtained by using a CO laser pump source is due

to the resonance enhancement effect, [1] which enhances the single particle

cross section considerably. For experiments with a CO_2 laser pump, Aggarwal

etc. [21] obtained a comparatively lower threshold because they used a longer

crystal, which in effect reduces the reflection loss, as can be seen from (IV.3).

For $\alpha = 0.3$ cm^{-1} (see Figure 3.2), with a 2 cm long sample, we get $\gamma = .065$ cm^{-1}, as compared with $\gamma = 0.228$ cm^{-1} for a 0.4 cm crystal. Thus we see that to achieve lower thresholds it is better to use longer sample subjecting to the condition (2.V.8). Figure 3.5 plots the threshold as a function of the sample length L , and shows a minimum at $\bar{L}$

$$e^{-\alpha \bar{L}} = \alpha \bar{L} - \ln R + 1 . \qquad (V.1)$$

Figures 3.5 and 3.6 shows the power behavior in the $\vec{q}.\vec{B} = 0$ noncollinear geometry for the CO pump [17] and a CO_2 pump [13] respectively. In this geometry the anti-Stokes waves are absent. Because of its lower threshold, the CO pump experiments can achieve much higher conversion efficiency, so that depletion effects must be taken into account. A close check is obtained with experimental results.

The saturation of Stokes power is also examined. The power saturation formula is given by (2.VI.31). Here we let $1/W_{12}$ to be the spin relaxation time $\tau_s \simeq 2 \times 10^{-8}$ sec. With the experimental data of Aggarwal, etc, [21] $N = 2 \times 10^{16}$ cm^{-3}, equation (2.VI.31) yields a Stokes saturation at $(I_s)_{max} = 4 \times 10^4$ watts/cm^2, as compared to the 2.2×10^4 watts/cm^2 observed. A similar calculation with the data of Patel, etc, [13] for $N = 1.3 \times 10^{16}$ yields $(I_s)_{max} = 2.8 \times 10^4$ watts / cm^2, comparing with the observed value 3.2×10^4 watts/cm^2.

Note that by taking $1/W_{12} \simeq \tau_s$, we have neglected the effects of electrons diffusion in and out of the pump beam. That Patel, etc., [13] obtained a higher satura-

ted power than Aggarwal, etc,[21] in spite of their lower carrier concentration,

is most probably due to this diffusion effect. In Patel's experiment, [13] a beam

with radius $\sim 100\mu$ is used in comparison with the ~ 0.12 cm beam radius of

Aggarwal,[21] and because of this small radius, the electrons are easier to

diffuse through, thus increasing the maximum output power.

Let us comment on the magnetic field behavior of the Stokes power. It

has been observed[11],[13] that the stimulated emission stops once when the

system passed out of the quantum limit. This is not surprising if the threshold

condition (2.VI.30) is examined closely. From Chapter 1 we see that the spon-

taneous width Γ increases by a factor of about 3 as the spin down level sinks

below the Fermi level. Calculations of section III shows that the effective num-

ber of electrons that can be scattered decreases as spin down sublevel starts

to get populated. Together these two effects would increase the threshold by

an order of magnutude. This would make stimulated emission harder to obtain.

They are, however, not impossible. Using low carrier concentrations to obtain

a narrow line, $(N = 10^{15}$ cm$^{-3})$, Patel[23] has observed stimulated emission at

magnetic field as low as 400G.

We now turn to examine the anti-Stokes(AS) behavior. As said in Chapter

2, stimulated AS scatterings are only possible in the $\vec{q}.\vec{B} = 0$ collinear geometry.

The threshold conditions for AS emission is the same as for Stokes, and is con-

firmed by experiment. The power output behavior of the Stokes-AS emission

is given in Figure 2.11, which represents a close agreement with experiment.[19]

Several qualitative properties of our Raman laser theory is well supported by experimental observations. First of all, the AS to Stokes power ratio r, is calculated for two cases. In Patel's experiment [17], with L = 0.4 cm, giving a γ = 0.228 cm^{-1}, equation (2 .VI.16) gives r = 0.09, as compared to an observed r = 0.08. Similarly, with (2.VI.16) and a γ = of 0.065 cm^{-1} resulting from a L = 2 cm as used in Aggarwal's experiment, [21] we get r = 0.032, which can be compared with the observed value 0.03. Both cases agree well with experiment.

Also the constancy of r as a function of input power is notable. In Figure 3.7 is plotted the AS-Stokes ratio as a function of input power and is seen to check with the accompanying data.

More quantitative calculation of the SFR laser behavior will be carried out covering a wider range of carrier concentration, magnetic field and temperature in the near future. Optimal operating conditions will also be obtained.

APPENDIX 3A.   THE EULER MACLAURIN SUM FORMULA

For a derivation of the Euler Maclaurin formula, see reference 10. This technique is perhaps the most efficient way to deal with the summation of smooth functions as

$$\sum_{1}^{n} k^{1/2} \quad , \quad n \quad \text{interger} \quad .$$

Consider the summation of a smooth function $f(k)$, the formula states

$$\sum_{k=0}^{n} f(k) = \int_{0}^{n} f(x)\,dx + C + \frac{1}{2}f(n) + \frac{B_2}{2!}f'(n) + \cdots$$

$$\cdots + \frac{B_{2m}}{(2m)!}f^{(2m-1)}(n) - \int_{0}^{n} f^{(2m)}(x)\,dx\,\frac{B_{2m}(x-[x])}{(2m)!}$$

(3A.1)

where C is independent of n ,

$$C = \frac{1}{2}f(0) - \frac{B_2}{2!}f'(0) - \cdots - \frac{B_{2m}}{(2m)!}f^{(2m-1)}(0)$$

(3A.2)

and $[x]$ is the largest integer $\leq x$. The $B_m(x)$'s in (3A.1) are Bernoulli Polynomials,

$$B_m(x-[x]) = 2(2m)!\,(2\pi)^{-2m}(-1)^{m+1}\sum_{k=1}^{\infty} k^{-2m}\cos(2\pi k x)\ ,$$

(3A.3)

and the B_m 's are Bernoulli numbers, the first few are given by

$$B_1 = \frac{1}{6}\ ;\qquad B_2 = \frac{1}{30}\ ;\qquad B_3 = \frac{1}{42}\ ;$$

$$B_4 = \frac{1}{30}\ ;\qquad B_5 = \frac{5}{66}\ ;\qquad B_6 = \frac{691}{2730}\ .$$

An error estimation of neglecting the integral term in (3A.1) is given with the help of the properties of the Bernoulli Polynomial

$$\left|\,B_{2m}(x-[x])\,\right| \leq \left|\,B_{2m}\,\right| = 2(2m)\frac{1}{(2\pi)^{2m}}\sum_{k=1}^{\infty} k^{2m}\ ,$$

(3A.4)

thus it follows that

$$\left|\int_{0}^{n} f^{(2m)}(x)\,\frac{B_{2m}(x-[x])}{(2m)!}\,dx\right| \leq \frac{|B_{2m}|}{(2m)!}\int_{0}^{n} f^{(2m)}(x)\,dx$$

(3A.5)

APPENDIX 3B.   FERMI ENERGIES IN FINITE TEMPERATURE

First let us consider the case when no magnetic field is present. The zero temperature Fermi energy is well known *

$$\mathcal{E}_o \triangleq \mathcal{E}_F(o) = \frac{\hbar^2}{2m^*} (3\pi^2 N)^{2/3} . \tag{3B.1}$$

At low temperature, $\mathcal{E}_F(T)$ can be obtained through the free energy, which, for $k_B T \ll \mathcal{E}_o$, has form [9]

$$F \simeq N \left\{ \frac{3}{5} \mathcal{E}_o - \left(\frac{\pi k_B T}{2}\right)^2 \frac{1}{\mathcal{E}_o} + \frac{7}{60} \left(\frac{\pi k_B T}{2}\right)^4 \frac{1}{\mathcal{E}_o^3} \cdots \right\} . \tag{3B.2}$$

The Fermi energy is then given by

$$\mathcal{E}_F(T) = \frac{\partial F}{\partial N} \cong \mathcal{E}_o - \frac{1}{6}\left(\frac{\pi k_B T}{2}\right)^2 \frac{1}{\mathcal{E}_o} - \frac{7}{6}\left(\frac{\pi k_B T}{2}\right)^2 \frac{1}{\mathcal{E}_o^3} \cdots , \tag{3B.3}$$

$$k_B T \ll \mathcal{E}_o .$$

As temperature increases, $\mathcal{E}_F \triangleq \mathcal{E}_F(T)$ can be found by solving

$$N = \frac{1}{(2\pi)^2} \left(\frac{2m^*}{\hbar^2}\right)^{3/2} \int_o^\infty \rho(\mathcal{E}) f(\mathcal{E}) d\mathcal{E} . \tag{3B.4}$$

With $\rho(\mathcal{E})$ given by (1G.3), solving for T in (3B.4) with $\mathcal{E}_F(T) = o$, we find that

$$\mathcal{E}_F = o , \qquad k_B T = \mathcal{E}_o . \tag{3B.5}$$

Thus, for $k_B T > \mathcal{E}_o$, the Fermi energy goes negative, as can be seen from curve A for Figure 3.8, we can then use the expansion [25]

---

*   Note that all energies are measured from $\frac{1}{2}\hbar\omega_c$.

$$\frac{1}{p!} \int_{0}^{\infty} \frac{\varepsilon^{\,\ell}\, d\varepsilon}{e^{(\varepsilon-\varepsilon_F)/k_BT} + 1} \;=\; (k_BT)^{p+1} \sum_{r=1}^{\infty} (-1)^{r-1}\, \frac{e^{\,r\varepsilon_F/k_BT}}{r^{\,p+1}}$$

(3B.6)

Keeping the first two terms in (3B.6) with p = 1/2 and solving for ε_F , we get

$$\varepsilon_F = k_BT\, \log \left\{ \sqrt{2}\left[1 - \sqrt{1 - \tfrac{4}{3}\tfrac{\sqrt{2}}{\sqrt{\pi}}\left(\tfrac{\varepsilon_o}{kT}\right)^{3/2}}\,\right] \right\}$$

(3B.7)

which is an improvement of using the Boltzmann distribution in (3B.4)

Now we try to calculate the Fermi energy in a magnetic field. $\rho(\varepsilon)$ is given then by equation (1.III.3), and we have to sum over Landau levels n. First consider the zero temperature case. In the large field limit, so that only the first spin up sublevel is occupied, ε_o can be solved at once

$$\varepsilon_o = \left(\tfrac{N}{2}\right)^2 (2\pi\ell)^4 \frac{\hbar^2}{2m^*} - \tfrac{1}{2}\hbar\omega_s \;, \qquad -\tfrac{1}{2}\hbar\omega_s < \varepsilon_o < \tfrac{1}{2}\hbar\omega_s \;,$$

(3B.8)

where $\ell = (\hbar c/eB)^{1/2}$. When the first spin down sublevel is also occupied, we get

$$\varepsilon_o = \tfrac{1}{4}\left(\tfrac{N}{2}\right)^2 (2\pi\ell)^4 \frac{\hbar^2}{2m^*} + \left(\tfrac{\hbar\omega_s}{2}\right)^2 \left(\tfrac{2}{N}\right)^2 \frac{2m^*}{\hbar}\,(2\pi\ell)^{-4} \;,$$

(3B.9)

$$\tfrac{1}{2}\hbar\omega_s < \varepsilon_o < \hbar\omega_c - \tfrac{1}{2}\hbar\omega_s \;.$$

When more than one Landau levels are occupied, a solution of ε_o is not as easy, we will use the Euler Maclaurin sum formula described in the last Appendix to perform the summation over Landau levels. Keeping only two terms in the expansion (3A.1), we get

$$\mathcal{E}_o = \left(\tfrac{3}{2}\pi^2 N\right)^{\tfrac{2}{3}} \frac{\hbar^2}{2m^*} \left\{\left[1 + \sqrt{1 + \frac{32\pi^2}{9N^2}(2\pi\ell)^{-6}} \,\right]^{\tfrac{1}{3}} \right.$$

$$\left. + \left[1 - \sqrt{1 + \frac{32\pi^2}{9N^2}(2\pi\ell)^{-6}} \,\right]^{\tfrac{1}{3}} \right\} \qquad , \quad \mathcal{E}_o > \hbar\omega_c - \frac{\hbar\omega_s}{2} . \tag{3B.10}$$

The error bound for $\mathcal{E}_o$ as given in (3B.10) can be found by using (3A.5).

Now we try to find the variation of $\mathcal{E}_f$ with temperature. Only the case of extreme quantum limit, $-\hbar\omega_s/2 < \mathcal{E}_o < \hbar\omega_s/2$ will be considered. By using tabulated values of the Fermi integral, the fermi energy is plotted as a function of temperature in curve B of Figure 3.8. As can be seen, at very low temperature, the Fermi level increases with temperature, which can be expressed analytically by methods parallel to that leading to (3B.3),

$$\mathcal{E}_f = \mathcal{E}_o + \tfrac{1}{3}\left(\frac{\pi k_B T}{2}\right)^2 \frac{1}{\mathcal{E}_o} + \frac{7}{12}\left(\frac{\pi k_B T}{2}\right)^2 \frac{1}{\mathcal{E}_o^3} \qquad , \qquad k_B T \ll \mathcal{E}_o . \tag{3B.11}$$

Further increase in temperature decreases the Fermi level, we get,

$$\mathcal{E}_f = k_B T \qquad , \qquad k_B T = 1.2\,\mathcal{E}_o$$

$$\mathcal{E}_f = 0 \qquad , \qquad k_B T = 3.5\,\mathcal{E}_o \tag{3B.12}$$

At high temperature, the first two terms in the expansion (3B.6) with p = -1/2 will give

$$\mathcal{E}_f = k_B T \log \left\{\frac{1}{12} - \sqrt{\frac{1}{2} - \frac{2}{\sqrt{\pi}}\left(\frac{\mathcal{E}_o}{k_B T}\right)^{\tfrac{1}{2}}} \,\right\} \tag{3B.13}$$

quite similar to the Fermi energy when no magnetic field is present.

$\hbar\omega_p$ (ev)	$\left(\dfrac{d\sigma}{d\Omega}\right)_s$ (cm^2)	N (cm^{-3})	L (cm)	I°_{th} (watts/cm^2)	
				experiments	theory
q.B = 0 noncollinear geometry					
0.116	1.0×10^{-23}	1.3×10^{16}	0.2	6.4×10^5 [13]	4.0×10^5
0.235	1.5×10^{-20}	1.0×10^{16}	0.4	4.1×10^3 [17]	1.0×10^3
q.B = 0 collinear geometry					
0.116	1.0×10^{-23}	1.3×10^{16}	0.4		2.1×10^5
0.116	1.0×10^{-23}	2.0×10^{16}	2.0	4.0×10^4 [21]	5.0×10^4
0.235	1.5×10^{-20}	1.0×10^{16}	.48	6.8×10^2 [18]	8.7×10^2

Table 3.1   Values of threshold pump power from experiments and calculations.
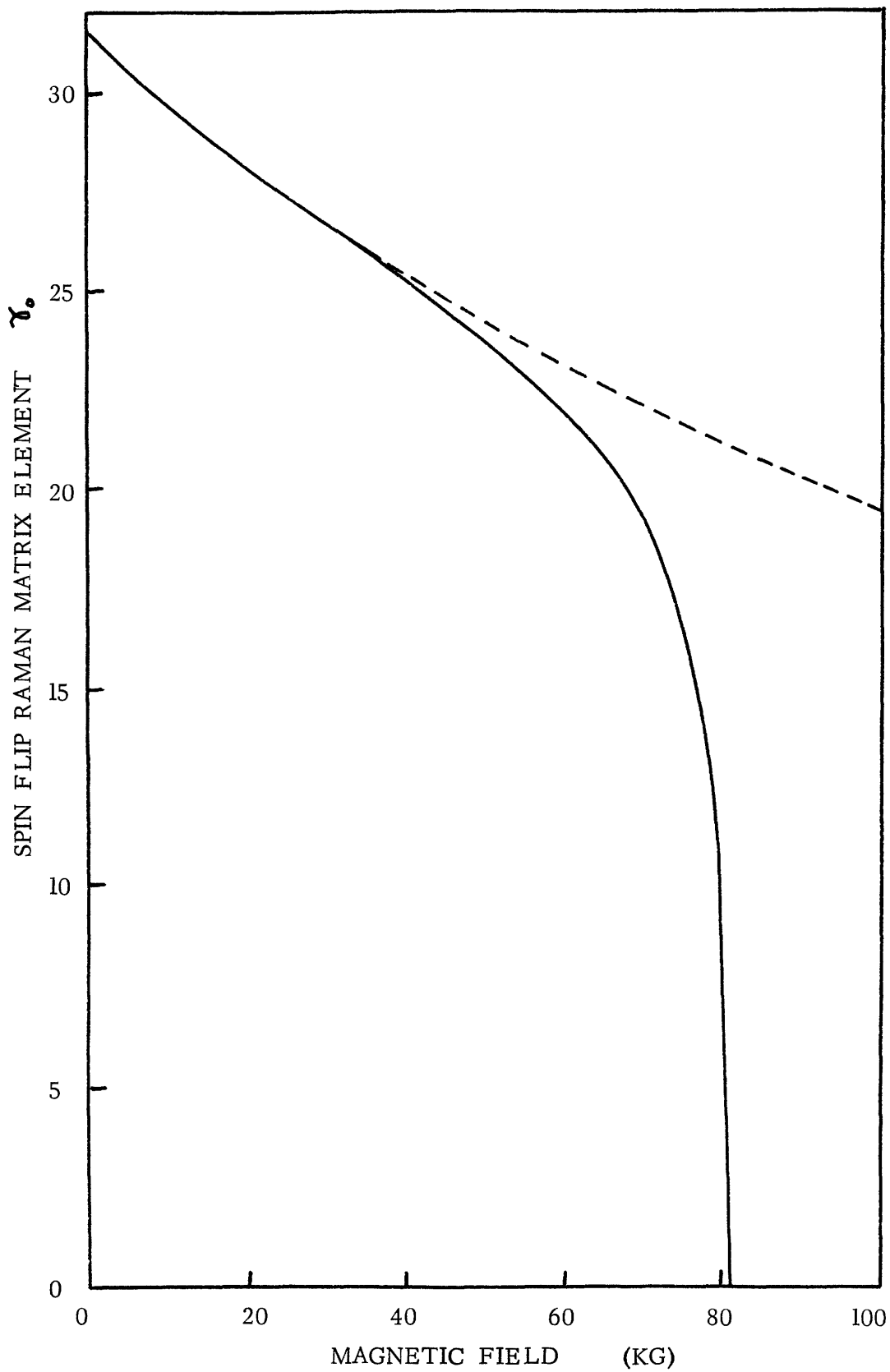$\Gamma = 0.5$ cm^{-1}, R = 36%.

Figure 3.1   Spin flip matrix element as a function of magnetic field.   The dotted line takes into account only valence band intermediate states.
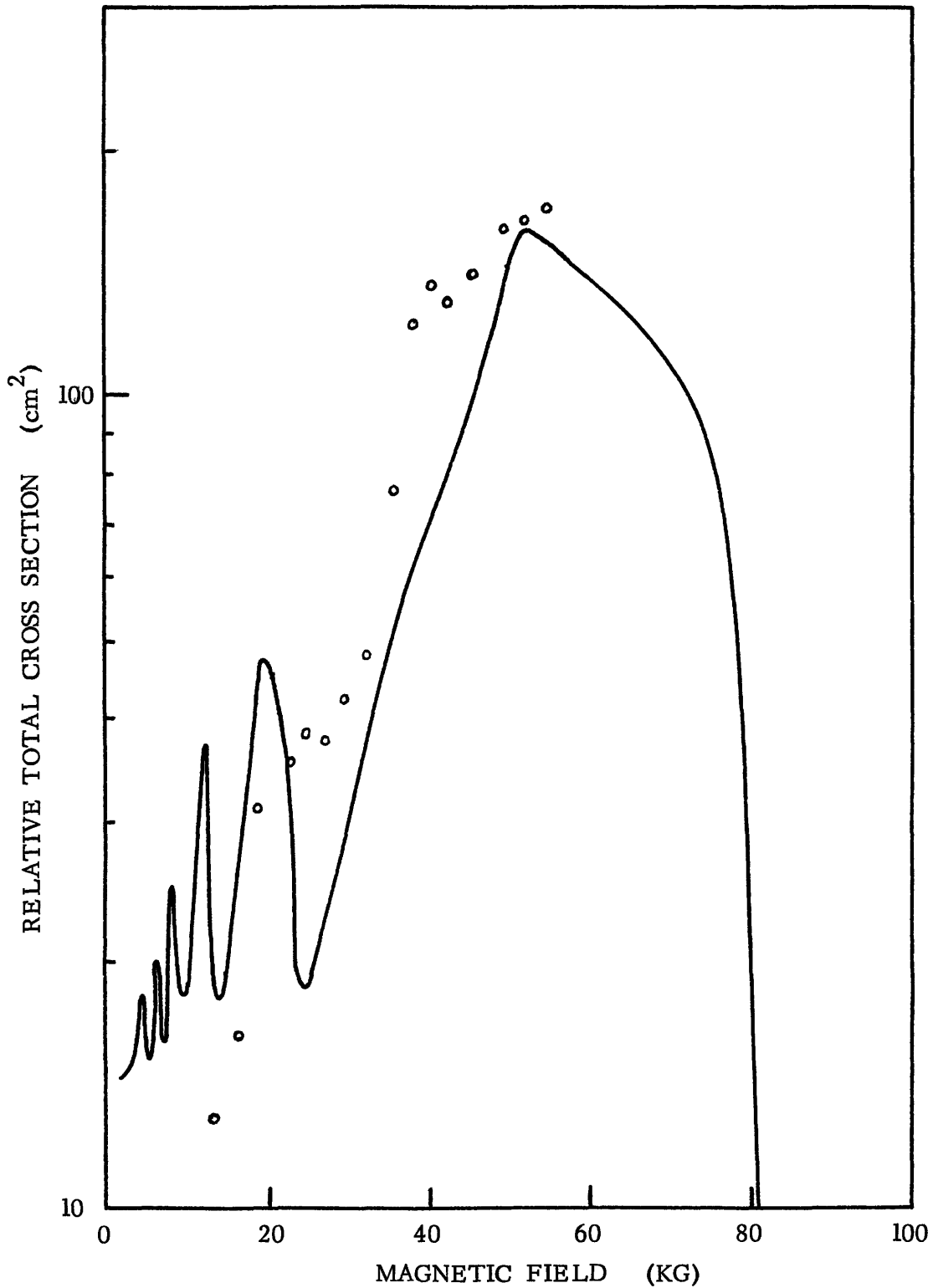
Figure 3.2   Integrated total cross section for spin flip scattering in n-InSb.
$N = 3 \times 10^{16}$ cm^{-3}. $T = 30°$ K.   The circles are experimental data taken from reference 11.
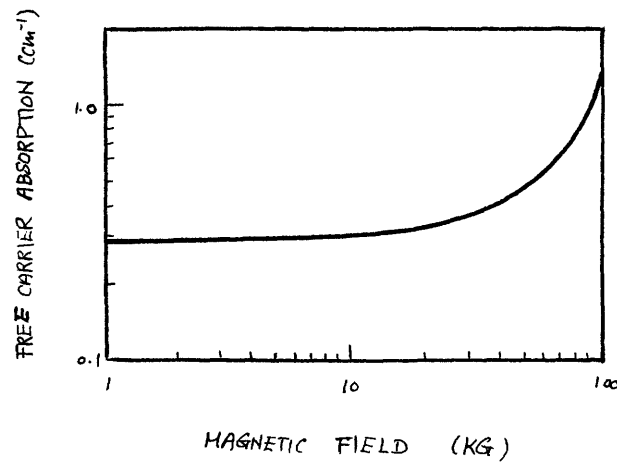
Figure 3.3a Variation of free- carrier absorption in n-InSb as a function of magnetic field at the wavelength of SFR scattering (pump at 10.6 μ) for n- InSb with n = 1.3 x 10^{16} cm^{-3}. [13]
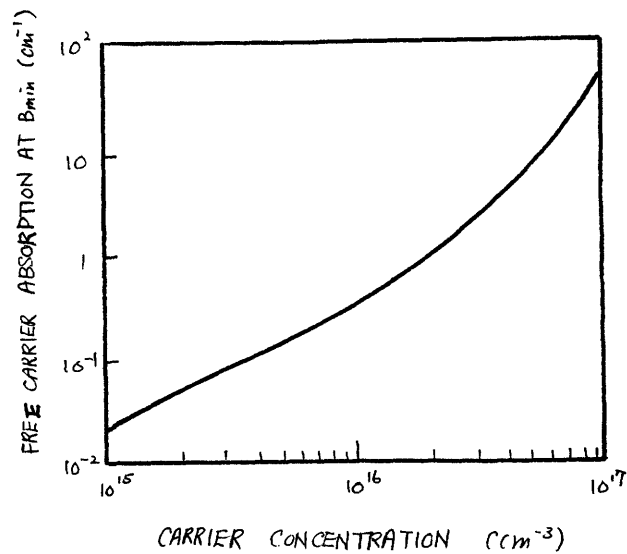

Figure 3.3b Free carrier absorption in n-InSb as a function of carrier concentration at the SFR scattering wavelength and at magnetic field required to reach the quantum limit. [13]
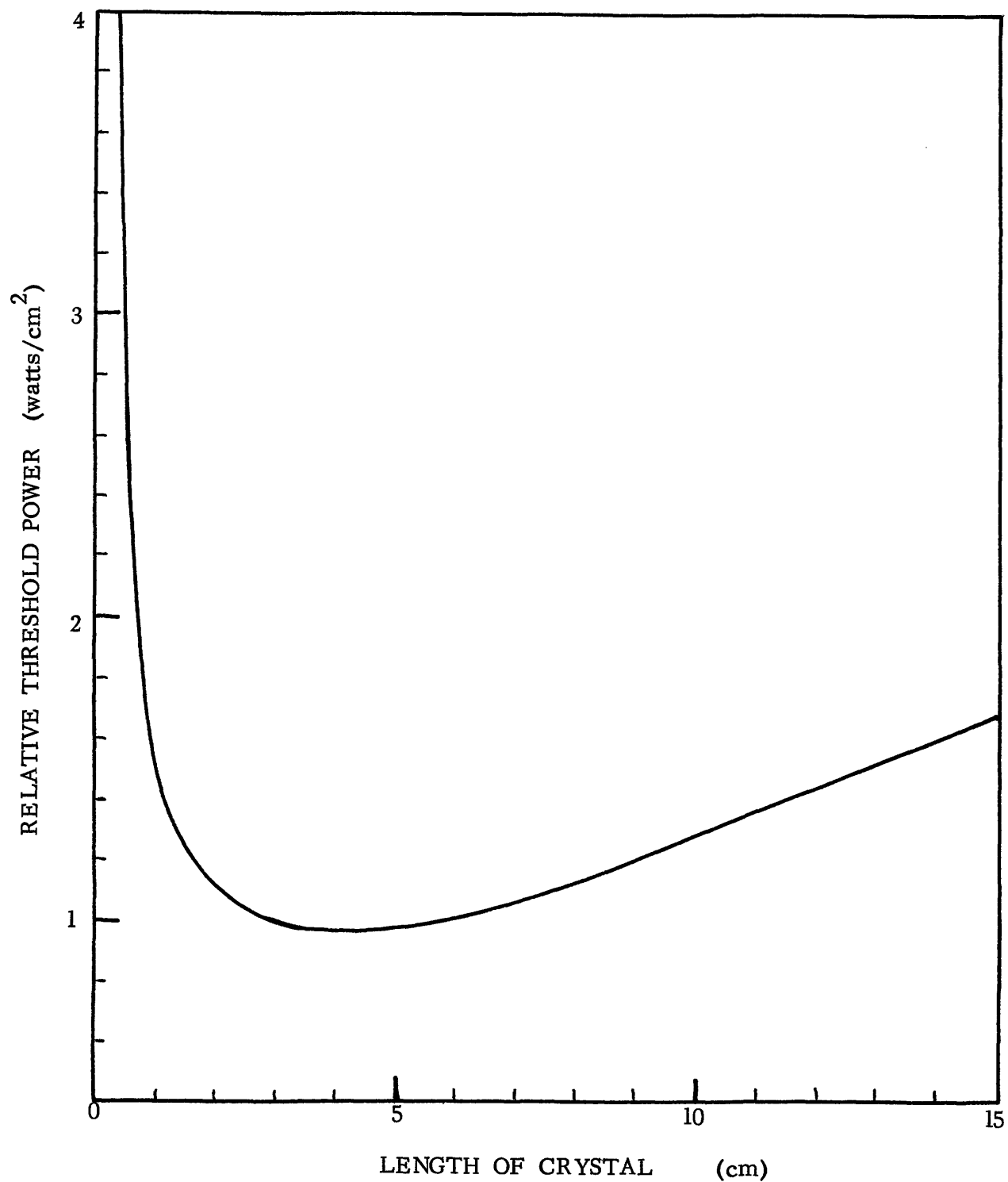
Figure 3.4   Threshold pump power as a function of the crystal length for the collinear geometry of Figure 2.6.

Figure 3.5   Stimulated Stokes output power as a function of input pump power.
ω_p = 5.32 μm .   The circles are experimental results taken from reference 17.
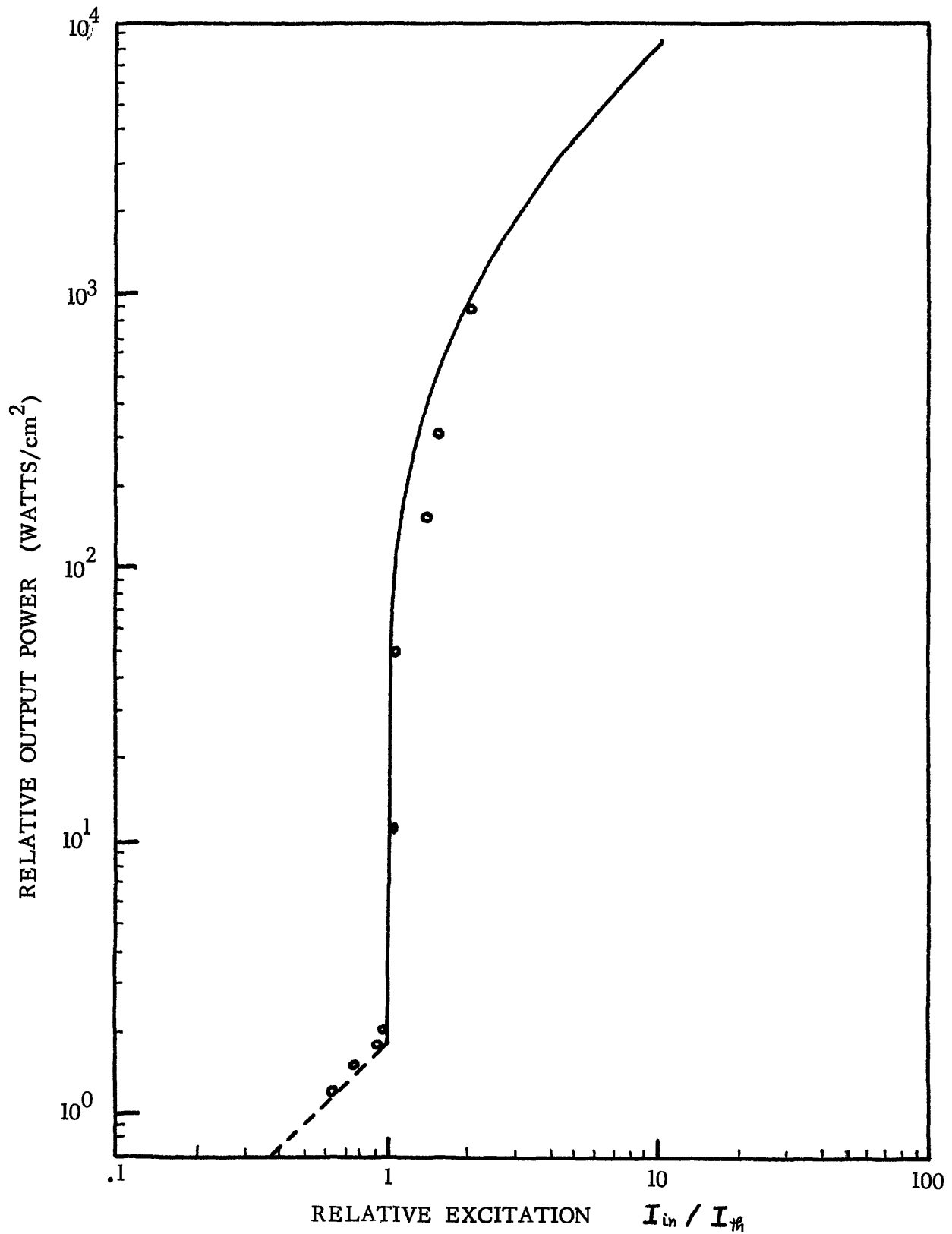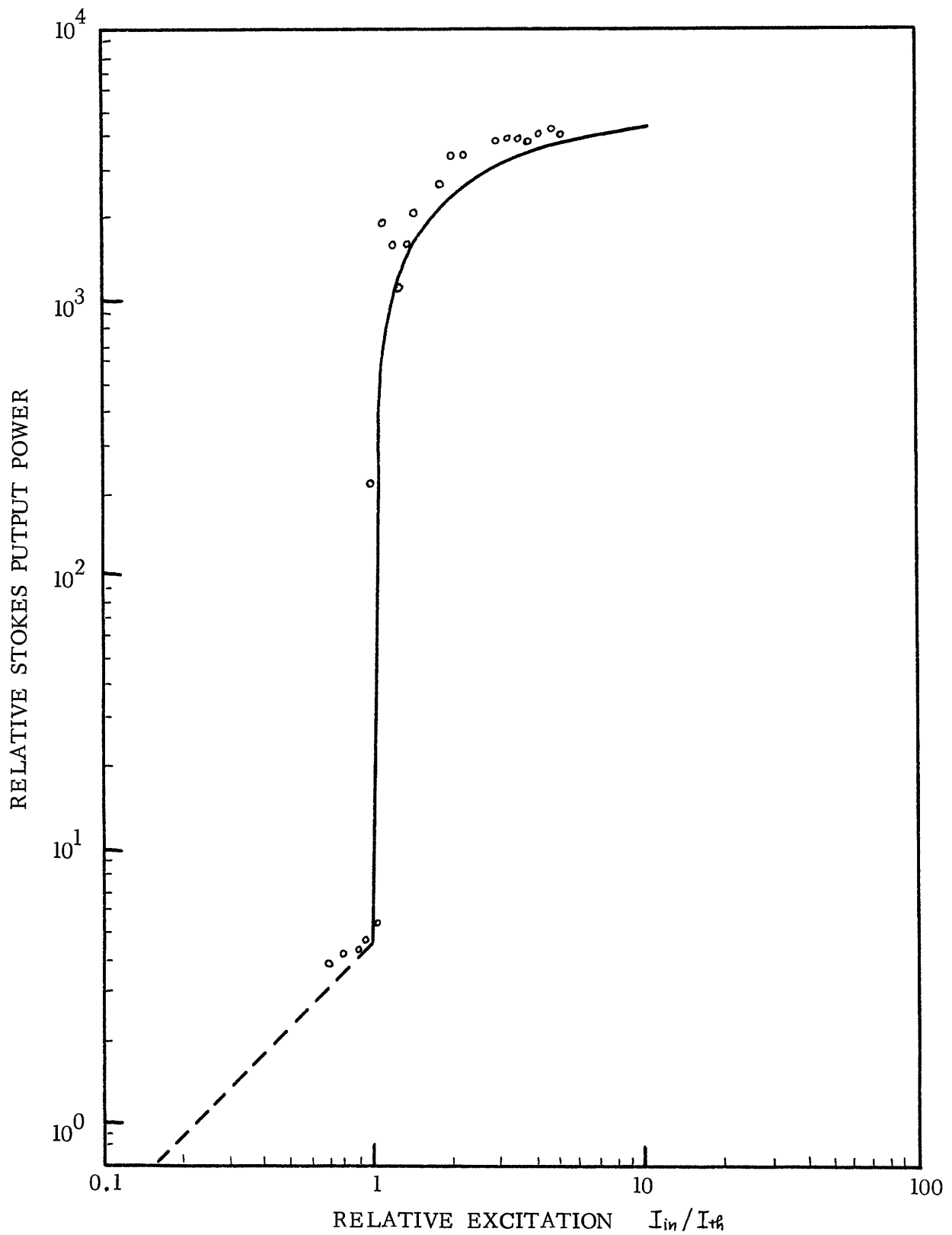
Figure 3.6   Stimulated Stokes output power as a function of pump power.

ω_p = 10.6 μ .   The circles are experimental results from reference 13.

Figure 3.7   Anti-Stokes to Stokes output power ratio as a function of input pump power.   The dots are experimental results taken from reference 19.

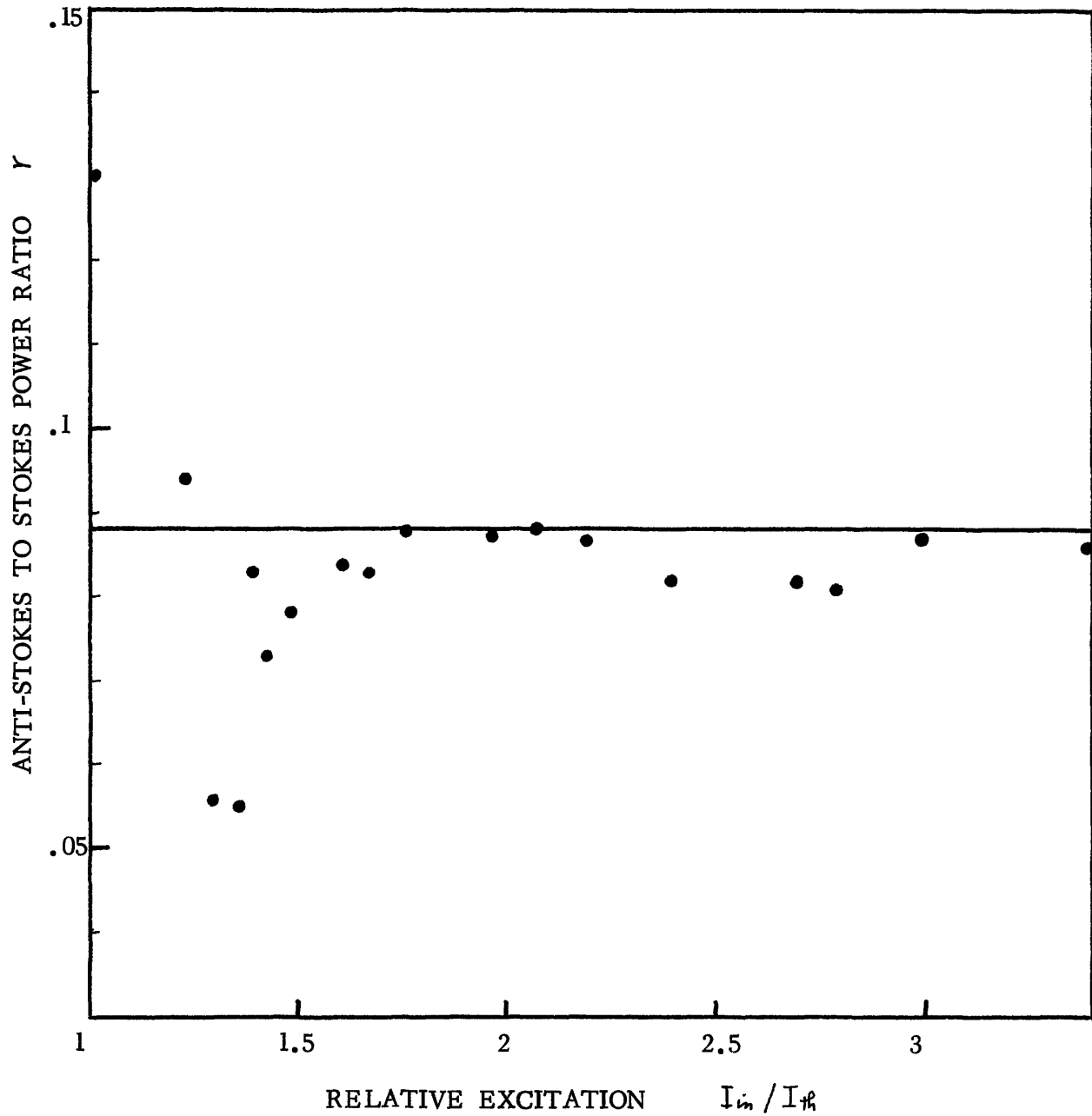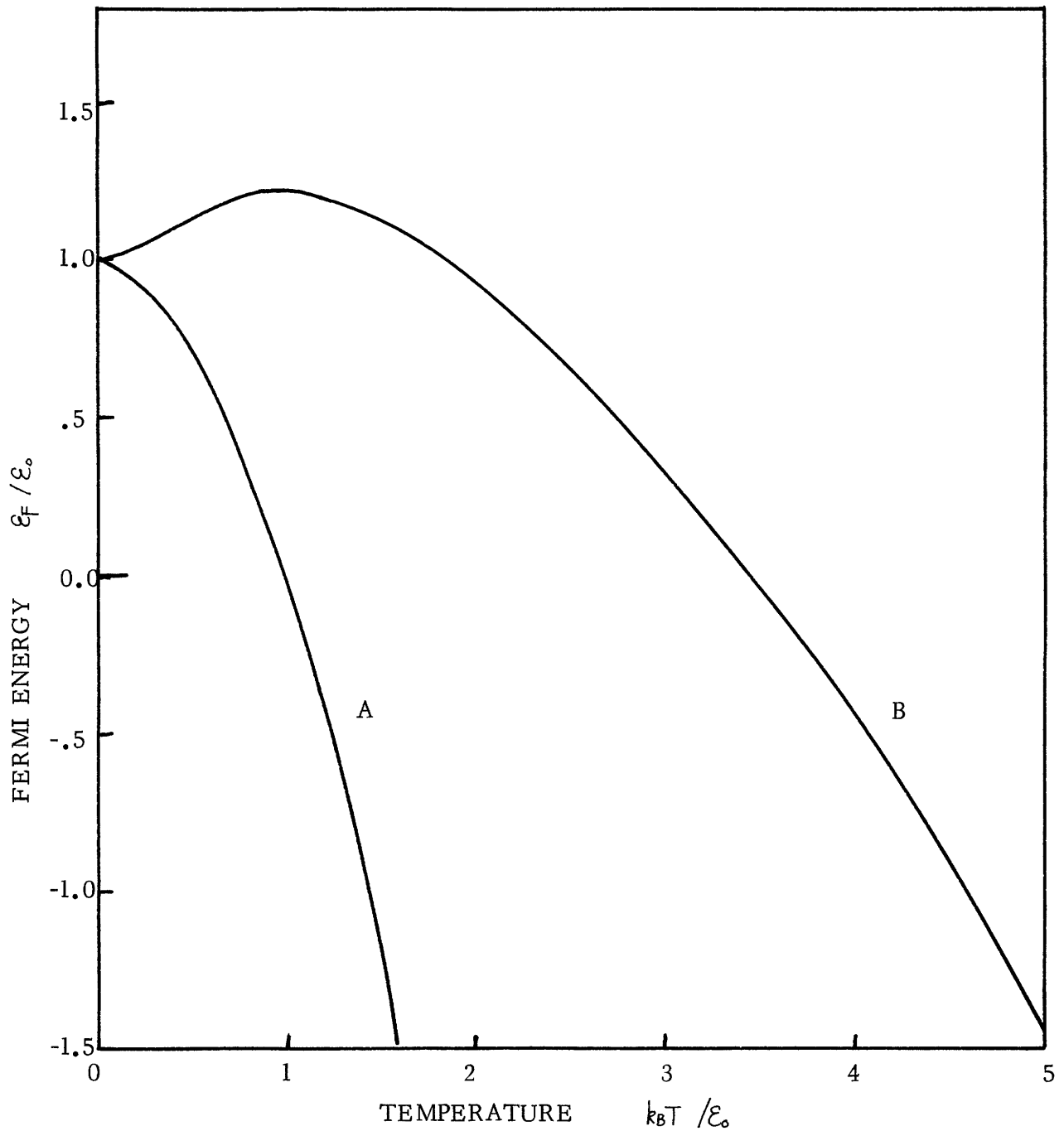Figure 3.8   Fermi energy as a function of temperature.   Both the Fermi level
and the temperature is normalized with respect to the zero-temperature Fermi
energy $\mathcal{E}_o$.   Curve A is for zero magnetic field case,   and Curve B is for
electrons in the "quantum limit".

REFERENCES

(0)   W. E. Lamb, Jr., Phys. Rev. 134 1429 (1964)

(1)   P. A. Wolff, Phys. Rev. Letters, 16, 225 (1966)

(2)   Y. Yafet, Phys. Rev. 152, 858 (1966)

(3)   V. P. Makharov, Soviet Phys. JETP 28, 336 (1969)

(4)   G. B. Wright, P. L. Kelley and S. H. Grove, in Light Scattering Spectra of Solids, Ed. by G. B. Wright, Springer-Verlag, New York 1969

(5)   S. R. J. Brueck, Ph.D. thesis, submitted to M.I.T., Cambridge, 1971

(6)   R. L. Aggarwal, B. Lax, C. R. Pidgeon and D. Limbert, Int. Conf. on Light Scattering Spectra of Solids, Paris, 1971; C. K. N. Patel, (private communication)

(7)   B. S. Wherett and P. G. Harper, Phys. Rev. 183, 692 (1969)

(8)   P. A. Fleury and J. F. Scott, Phys. Rev. B 3, 1979 (1971)

(9)   see, e.g., L. D. Landau and E. M. Lifshitz, Statistic Physics, Pergamon Press, London, 1958

(10)   see, e.g., N. G. de Bruijn, Asymtotic Methods in Analysis, North Holland Publishing Co., Amsterdam (1958)

(11)   C. K. N. Patel, in Modern Optics, Vol. XVII, Polytechnic Press, New York, 1967

(12)   E. D. Palik and G. B. Wright, in Optical Properties of III-V Compounds, Ed. by Willardson and Beer , Academic, New York, 1966

(13)   C. K. N. Patel and E. D. Shaw, Phys. Rev. B 3, 1279 (1971)

(14)   C. K. N. Patel and E. D. Shaw, Phys. Rev. Letters, 24, 451 (1970)

(15)   C. K. N. Patel, E. D. Shaw, and R. J. Kerl, Phys. Rev. Letters, 25, 8 (1970)

(16) R. L. Allwood, etc., J. Phy. C. Solid State Phys. 3, L186 (1970)

(17) A. Mooradian, S. R. J. Brueck amd F. A. Blum, Appl. Phys. Letters, 17, 481 (1970)

(18) S. R. J. Brueck, A. Mooradian, Appl. Phys. Letters, 18, 383 (1971)

(19) E. D. Shaw and C. K. N. Patel, Appl. Phys. Letters 18, 215 (1971)

(20) R. L. Allwood, etc., J. Phy. C. Solid State Physics 4, L163 (1971)

(21) R. L. Aggarwal, etc., Appl. Phys. Letters, 18, 383 (1971)

(22) C. K. N. Patel, Appl. Phys. Letters, 18, 274 (1971)

(23) C. K. N. Patel, Appl. Phys. Letters, 19, 400 (1971)

(24) W. Rogosinski, Fourier Series, Chelsea, New York

(25) R. B. Dingle, Appl. Sce. Res. B 6, 225 (1953)

(26) Beer, Chase and Choquard, Helv. Phys. Acta., 29, 529 (1955)

CHAPTER   4

STRESS TUNED STIMULATED LIGHT SCATTERING

IN p-TYPE SEMICONDUCTORS

I. INTRODUCTION

Recently, stimulated spin-flip light scattering in n-InSb [1] and its appli-cation as a tunable source of coherent infrared radiation [2] have been reported. Considerable interest persists [3] in extending and further exploring this useful laser process. However, the tunability of the spin-flip Raman (SFR) laser is, limited by the magnetic field dependence of the scattering cross section, and by the strength of available magnetic fields.

We propose in this Chapter to employ stress as the tuning mechanism of a Raman laser based on the process of stimulated inter-valence band scatt-ering (SIV) in p-type semiconductors. Specifically, we consider the Stokes scattering with associated hole transition between heavy and light hole bands of opposite spin, as indicated in Figure 4.1. An external uniaxial stress S splits the valence band by an amount linearly proportional to S, thus the Stokes frequency ω_s can be tuned through the stress. Besides offering a versatile laser source, the spontaneous and the stimulated scattering of holes could serve as a probe of the properties of p-type semiconductors. Valence band structure, relaxation mechanisms and nonlinear effects might be studied by this

method. In the following we give a careful investigation of this process, taking the complicated valence band into account.

The valence band structure in the presence of an uniaxial stress is given in section II. In section III we calculate the spontaneous scattering cross section and linewidths, which, together with the loss coefficients found in section IV, gives the threshold conditions for stimulated emission. In section V, the stimulated behaviors are investigated in details, including the threshold oump power, stimulated power output and linewidth.

II. VALENCE BAND STRUCTURE UNDER AN EXTERNAL UNIAXIAL STRESS

Consider a cubic crystal with a s-like conduction band lying above p-like valence bands, the band gap at $\vec{k} = 0$ is E_g . Spin orbit interaction further splits the six-fold degenerate valence band edge into a four fold $P_{3/2}$ multiplet and a twofold $P_{1/2}$ doublet separated by δ . Off $\vec{k} = 0$, the energy bands can be determined by using $\vec{k}.\vec{p}$ perturbation theory. The $\vec{k}.\vec{p}$ hamiltonian in terms of angular momentum operators $\vec{J}$ is given by [4]

$$H_k = A k^2 - B\left[k_x^2(J_x^2 - \tfrac{1}{3}J^2) + k_y^2(J_y^2 - \tfrac{1}{3}J^2) + k_z^2(J_z^2 - \tfrac{1}{3}J^2) \right]$$

$$- \tfrac{2N'}{3}\left[\{J_xJ_y\}\{k_xk_y\} + \{J_xJ_z\}\{k_xk_z\} + \{J_yJ_z\}\{k_yk_z\} \right]$$

(II.1)

where A , B and N' are the valence band parameters, [5] and $\{\cdots\}$ denotes the symmetrized product, $\{J_xJ_y\} = \tfrac{1}{2}(J_xJ_y + J_yJ_x)$, etc,.

An uniaxial stress applied to the crystal removes the cubic symmetry, and splits the $P_{3/2}$ bands into a pair of degenerate Kramer's doublets. Kleiner and Roth [6] have given a strain hamiltonian H_e to describe this splitting of the $P_{3/2}$ states at $\vec{k} = 0$

$$H_e = D_d^v (e_{xx} + e_{yy} + e_{33}) + \frac{2}{3} D_u \left[(J_x^2 - \frac{1}{3} J^2) e_{xx} + (J_y^2 - \frac{1}{3} J^2) e_{yy} \right.$$
$$\left. + (J_3^2 - \frac{1}{3} J^2) e_{33} \right] + \frac{2}{3} D_u' \left[\{ J_x J_y \} e_{xy} + \{ J_x J_3 \} e_{x3} + \{ J_y J_3 \} e_{y3} \right], \quad \text{(II.2)}$$

where the e 's are the strain components, and the D 's are the valence band deformation potentials.

We will only consider here a stress S applied along the $[00\bar{1}]$ direction, so that (II.2) becomes

$$H_e = \frac{\Delta}{2} \left(J_3^2 - \frac{1}{3} J^2 \right) \quad \text{(II.3)}$$

where Δ gives the splitting of the heavy hole(hh) and light hole (lh) bands at $\vec{k} = 0$ as indicated in Figure 4.1 [6]

$$\Delta = \frac{4}{3} S \frac{D_u}{C_{11} - C_{44}} \qquad S \parallel [00\bar{1}] \quad . \quad \text{(II.4)}$$

The C 's are the elastic constants. For stress applied along other principle directions, see references 7 and 8.

Under large strains, the valence band edges decouple, so that H_k can essentially be considered as a first-order perturbation. Keeping only the diagonal elements of (II.1), we get the energies of the heavy hole band $\mathcal{E}_{hh}$,

the light hole band $\mathcal{E}_{\ell h}$, and the spin orbit splitt off band $\mathcal{E}_{so}$.

$$\mathcal{E}_{hh} = (A + \tfrac{B}{2})(k_x^2 + k_y^2)^2 - (A - B)k_3^2 \tag{II.5}$$

$$\mathcal{E}_{\ell h} = A k^2 + \tfrac{1}{2}(\Delta + \delta)$$
$$- \left\{ \left(\tfrac{\Delta + \delta}{2}\right)^2 - \tfrac{2}{3}\Delta\delta + \tfrac{B}{4}(k^2 - 3k_3^2)\left[B(k^2 - 3k_3^2) + 2(\delta + \tfrac{\Delta}{3})\right] \right\}^{1/2} \tag{II.6}$$

$$\mathcal{E}_{so} = A k^2 + \tfrac{1}{2}(\Delta + \delta)$$
$$+ \left\{ \left(\tfrac{\Delta + \delta}{2}\right)^2 - \tfrac{2}{3}\Delta\delta + \tfrac{B}{4}(k^2 - 3k_3^2)\left[B(k^2 - 3k_3^2) + 2(\delta + \tfrac{\Delta}{3})\right] \right\}^{1/2} . \tag{II.7}$$

From (II.5) - (II.7) we see that while the heavy hole band is unaffected by the presence of stress, the light hole and spin-splitt-off states are mixed by the strain.[8]

For $\quad \delta \gg \Delta, \; Bk^2 \quad$, (II.6) can be expanded to give

$$\mathcal{E}_{\ell h} \simeq A k^2 + \Delta + B\left(\frac{k^2 - 3k_3^2}{\delta}\right)\left(1 + \frac{\Delta}{3\delta}\right) , \tag{II.8}$$

which is linearly dependent on Δ .

III. SPONTANEOUS SCATTERING CROSS SECTION AND LINEWIDTH

Here we will consider the scattering of a pump photon of frequency ω_p to a Stokes photon of frequency ω_s with accompanying hole transition between the heavy and light hole bands of opposite spins. The differential cross section of this process can be obtained by approximating the heavy hole and light hole bands to be parabolic with effectives masses m_1 and m_2 respectively. Calculations parallel to the developments in section 1.III gives

$$\frac{d^2\sigma}{d\omega d\Omega} = \left(\frac{e^2}{mc^2}\right)^2 \frac{\omega_s}{\omega_p} \pi\hbar |\gamma_o|^2 \int_o^\infty \rho(\varepsilon)\, d\varepsilon\, f(\varepsilon)\left[1 - f(\varepsilon+\hbar\omega)\right]\, \delta\left[\hbar\omega - \frac{\hbar^2 k^2}{2}(\frac{1}{m_2}-\frac{1}{m_1})\right] \quad \text{(III.1)} ,$$

where $\rho(\varepsilon)$ is the density of states and $f(\varepsilon)$ the Fermi function. In general $m_1 \gg m_2$, so that (III.1) can be reduced to

$$\left(\frac{d^2\sigma}{d\omega d\Omega}\right) = \left(\frac{e^2}{mc^2}\right)^2 \frac{1}{2\pi} \frac{\omega_s}{\omega_p} |\gamma_o|^2 \left(\frac{m_2}{\hbar}\right)^{3/2} \sqrt{2\hbar\omega}\, f\left(\frac{m_2}{m_1}\hbar\omega\right)\left[1 - f(\hbar\omega)\right] . \quad \text{(III.2)}$$

The matrix element γ_o , which is defined in equation (1.II.10), was first calculated for valence band spin-flip scattering processes by Yafet. [7] Using the energy band model described in section II, a calculation completely analogous to Yafet's gives the result for scattering under an uniaxial stress. To first order in Δ and k_{δ}^2 , we get

$$\gamma_0 = \frac{2P^2}{E_g} \frac{\hbar\bar{\omega}_p}{E_g} \frac{E_g^2}{E_g^2 - (\hbar\bar{\omega}_p)^2} \frac{9 + 2(Ak^2 - 2\Delta)/\delta}{\sqrt{6}\sqrt{3/2} + (Ak^2 - 2\Delta)\delta}$$

$$\times \left\{ \epsilon_{p3} \frac{\epsilon_{sx} + i\epsilon_{sy}}{\sqrt{2}} + \frac{\epsilon_{px} - i\epsilon_{py}}{\sqrt{2}} \epsilon_{s3} \right\},$$

(III.3)

where P is the interband momentum matrix element, the ϵ 's are the photon polarizations and $\bar{\omega}_p = (\omega_p + \omega_s)/2$. This matrix element is considerably larger than that of the conduction band spin-flip scattering. For InSb, for example, γ_0 is about eight times the value of conduction SFR scattering, making a factor of ~ 60 difference in the cross section. Generally the cross section is nearly independent of stress. In InSb with $\lambda_p = 10.6\,\mu$ and $dE_g/dS = 15 \times 10^{-6}$ ev/Kg-cm^{-2}, γ_0 decreases only by 8% as S increases to 10^4 Kg/cm^2. However, for scattering with $\hbar\bar{\omega}_p$ near E_g, γ_0 drops drastically with increasing S because of the decrease in the resonance enhancement.

Now we examine the spectrum (III.2) more closely. The spontaneous Stokes spectrum is expected to have a large linewidth because of the big difference between hh and lh band curvatures. The spectral shape is shown schematically in Figure 4.2. As can be seen, the spectrum is zero at $\omega = 0$, then increases with $\sqrt{\omega}$ until it reaches a peak value at $\bar{\omega}$. At the high frequency side of $\bar{\omega}$, the spectrum decreases as $\sqrt{\omega} \left[1 + \exp(m_s \hbar\omega/m_l - \epsilon_F)/k_B T \right]^{-1}$. Because of the small effective mass of the light hole band, the $\left[1 - f(\hbar\omega) \right]$ factor in (III.2) does not contribute much.

At zero temperature, the spectrum (III.2) has a peak at

$$\hbar\bar{\omega} = \Delta + m_1 \mathcal{E}_F / m_2 \quad , \qquad\qquad T = 0 \quad , \qquad \text{(III.4)}$$

which follows from the fact that the density of states increases monotonically with $\mathcal{E}$. The full width at half power point can then be solved at once by using methods that lead to (1.III.19)

$$\Gamma = \frac{3}{4} \frac{m_1}{m_2} \mathcal{E}_F \quad , \qquad\qquad T = 0 \quad . \qquad \text{(III.5)}$$

At low temperature, $k_B T \ll \mathcal{E}_F$, the abrupt cutoff at $\bar{\omega}$ is smoothed by the Fermi functions in (III.2), and the spectral peak is shifted to

$$\hbar\bar{\omega} = \Delta + \frac{m_1}{m_2}\left(\mathcal{E}_F + 0.78\, k_B T\right) \quad , \qquad k_B T \ll \mathcal{E}_F \quad , \qquad \text{(II.6)}$$

as shown in Figure 4.2b. The linewidth, however, is essentially unchanged, and can still be approximated by (III.5) .

As temperature increases, the Fermi level drops (see Appendix 3B), until it becomes negative for $\mathcal{E}_F(o) \leq k_B T$. At these high temperatures, the holes becomes non-degenerate, and we can use the Boltzmann distribution in (III.2). The lineshape now has peak at

$$\hbar\bar{\omega} = \Delta + \frac{m_1 k_B T}{2 m_2} \quad , \qquad k_B T \gtrsim \mathcal{E}_F(o) \qquad \text{(III.7)}$$

and full width

$$\Gamma = 1.8 \frac{m_1}{m_2} k_B T \quad , \qquad k_B T \gtrsim \mathcal{E}_F(o) \quad . \qquad \text{(III.8)}$$

Note that as the holes become non-degenerate, it is the temperature that dominates the linewidth, which is now independent of carrier concentration.

In general, these linewidths are very broad. For InSb with $N = 3 \times 10^{16}$ cm^{-3}, a width ~ 100 cm^{-1} is obtained for $T = 5°$K. This width is two orders of magnitude larger than the conduction SFR scattering linewidth.

IV. LOSSES

Another important quantity which determines the possibility of stimulated emission is the losses of the Raman media Υ , which is composed as usual of the bulk absorption α and the reflection losses. Absorption in p-type semiconductors is dominated by free carrier inter-valence band absorption. Kane [10] has found that the absorption coefficient α is proportional to the carrier concentration N

$$\alpha(\omega, N, T) \sim \frac{N}{\hbar\omega} \left[\frac{d(\hbar\omega)}{dk^2} \right]^{-1} \left\{ f\left(\frac{\hbar^2 k^2}{2m_1}\right) - f\left(\frac{\hbar^2 k^2}{2m_2}\right) \right\} . \qquad \text{(IV.1)}$$

Infrared absorption data are available for p-type Ge,[11] InSb,[12] GaAs,[13] InAs.[14] Equation (IV.1) is used to extrapolate these data to the desired T and N. There are, of course, a very strong lattice absorption band, this we will not consider because stimulated emission will be impossible if ω is close to one of these absorption bands. Absorptions due to two or three phonon processes will be considered later when we discuss individual cases.

In Table 4.1 the optical loss of the Raman cavity Υ is listed for several semiconductors at various frequencies. A reflection loss of 1 cm^{-1} is added to α in estimating Υ , In general, the losses are very large

compared to the conduction band. This is due to the complicated band structure of the valence bands. To achieve SIV scattering, the Raman gain must be able to overcome this tremendous loss, and in the next section we will investigate this further.

V. STIMULATED EMISSION

Now we investigate the stimulated behavior of this inter-valence band scattering process. The tuning characteristics of the stimulated line will be given in the low temperature by using (III.6)

$$\hbar\omega_s = \hbar\omega_p - \hbar\bar{\omega} = \hbar\omega_p - \Delta - \frac{m_l}{m_2}(\mathcal{E}_f + 0.78 k_B T), \qquad k_B T \ll \mathcal{E}_f(0), \quad (V.1)$$

and in high temperature by (III.7)

$$\hbar\omega_s = \hbar\omega_p - \hbar\bar{\omega} = \hbar\omega_p - \frac{m_l}{2m_2} k_B T - \Delta, \qquad k_B T \gtrsim \mathcal{E}_f(0), \quad (V.2)$$

with Δ defined in (II.4). Thus we see that the Stokes frequency ω_s can be tuned linearly by varying the stress S.

With all the relevent parameters given in the previous section, the threshold pump power for SIV can readily be found. The Raman gain g_s is given by [15]

$$g_s = \frac{16\pi^2 c^3 (d\sigma/d\Omega)_T}{\hbar\omega_s^3 \, n_p n_s (\bar{n}+1) \, \Gamma} I \qquad (V.3)$$

where n_p, n_s are the refractive indices at ω_p, ω_s; I is the pump power flux, $\bar{n}$ the Bose distribution factor and $(d\sigma/d\Omega)_T$ is the total crosssection, i. e., equation (III.2) integrated over all ω.

Because of the large α , depletion of pump due to absorption must be taken into account. Equation (2.V.7) gives an expression of the absorption reduced pump rate I in terms of the actual pump rate $I^{\bullet}$

$$I = I_{0} \frac{1 - e^{-\alpha L}}{\alpha L}$$

(V.4)

where L is the length of the Raman cavity. If $\alpha L >> 1$, the pump power will all be absorped. The condition on L is thus

$$\alpha L \lesssim 1$$

(V.5)

For $\alpha L \simeq 1$, the pump power is reduced to about 64% of its original value. Equation (V.5) imposed a condition for the length of the Raman cavity. In InSb, for example, L should be less than 0.05 cm.

With the above development we can now consider the optimal choice of parameters T and N for achieving SIV. Low temperature is needed in order to have a reasonably narrow spontaneous linewidth. We fix $5^{\bullet}$K as a readily achievable temperature, although lower T is even more desirable. To minimize the threshold for SIV, we observe that a higher N would increase the absorption and the cross-section in about the same proportion as can be seen by comparing (III.2) and (IV.1). From equation (III.4) one sees that Γ can be minimized by choosing the smallest N such that the holes remain degenerate. Table 4.1 is constructed with this approach. We have also included the n-InSb SFR laser for comparison. Γ is calculated from (III.4), which is accurate to about 10% in our present case. The value of γ listed is that corresponding to ω_{p} , and the threshold power density I_{th}° is obtained by equating q_{s} of (V.1) to the value γ , together with equations (V.2) for $\alpha L = 1$.

The most promising crystal in this list is p-InSb with a CO_2 laser pump. Henceforth we will restrict our discussions to this material. First we consider the ω dependence of the various quantities in Table 4.1. The spontaneous linewidth Γ given by (III.5) is independent of ω, to a good approximation. The cross section is nearly independent of ω as noted before, and q_s increases slightly with decreasing ω from (V.3). The free carrier absorption, as obtained from extrapolation in N of Gobeli and Fan's experimental results, [12] is independent of ω from 15μ to $\sim 35\mu$, but decreases by an factor of 1/2 from 15μ to 11μ. In InSb, the main lattice band is at 52μ, around this frequency the crystal will be opaque to the scattered light. From $30\mu - 60\mu$ there is a two pho on absorption band. [16] In InSb, this two phonon process has absorption coefficient of about 8 cm^{-1}, which is about 10% of the free carrier absorption. Thus from 30μ on to 50μ, the threshold value will be $\sim 10\%$ larger than that given in Table 4.1.

To investigate the feasibility and the detailed behavior of Raman laser output, we need further information on the transition rates of the hh and lh bands. From mobility measurements [20] we have $\Gamma_2 \cong 115$ cm^{-1} and $\Gamma_1 \cong 5$ cm^{-1} where Γ_1 and Γ_2 are the relaxation rates for the hh and lh respectively. The radiative rates [12] are small compared to these values because η is small. Thus we have $\Gamma_2 \gg \Gamma_1$, so that the "fluorescence cycle" would work very well and we are able to sustain the laser output. Because of the short lifetime $\sim 10^{-13}$ sec. corresponding to $1/\Gamma_2$, the Raman output is considerable. For an input fluc of 3×10^7 watts/cm^2 the output power is ~ 100 KW/cm^3. We have therefore a reasonably high power laser.

The stimulated linewidth is inversly proportional to the rate of photon generation [21]

$$\Gamma = \frac{\gamma\Gamma}{\gamma/2+\Gamma} \frac{\hbar\omega \bar{N}}{2\gamma|b_s|}$$ (V.6)

where

$$\bar{N} = (\bar{n}+\tfrac{1}{2}) + \tfrac{1}{2} \frac{N_1+N_2}{N_2-N_1}$$ (V.7)

$\gamma|b_s|^2$ is the rate of Stokes photon density generated, and N_1 , N_2 are the hole population densities of the lh and ll bands respectively. (see Chapter 2 for more detailed definitions). At low temperature, the lh band is scarcely populated, so that $\bar{N} \cong 1$. For InSb with S = 5000 Kg/cm^2, Δ = 0.044 ev, we get a stimulated linewidth of the order of 10^4 Hz for a Raman output of 10 watts.

Our SIV is therefore an efficient, high power, tunable coherent source of infrared radiation in 11μ to $\sim 35\mu$. Compared with the n-InSb SFR laser of similar q_s/I , our laser has the desirable characteristics of providing higher power, covering a wider range of frequencies, as well as improving ease and speed of tuning.

Inter-valence band scattering could be useful method for studying p-type semiconductors. With judicious choice of parameters, as we have shown above, it may be possible to obtain stimulated scattering and to have a easily tunable laser source from $\sim 10\mu$ to $\sim 35\mu$. Further extensions into the far infrared appears to be limited only by the optical properties of InSb and its ability to stand up to high pressure.

	laser source	$\hbar\omega_p$(ev)	Γ(cm^{-1})	$\left(\frac{d\sigma}{d\Omega}\right)_T$(cm^{-1})	$\frac{g_s}{I}$ $\frac{cm^3}{watts}$	γ(cm^{-1})*	$I_0(\frac{Watts}{cm^2})$
Ge	Ar	0.69	38.7	6.0×10^{-6}	5.1×10^{-8}	1.75	5.3×10^{7}
InSb	CO$_2$	0.116	103	1.8×10^{-5}	2.6×10^{-5}	82	4.9×10^{6}
	CO	0.216	103	9.0×10^{-5}	1.8×10^{-5}	21	1.8×10^{6}
GaAs	YAG	1.16	18.7	6.0×10^{-6}	4.7×10^{-8}	1.5	5.0×10^{7}
InAs	CO$_2$	0.116	64.0	1.8×10^{-6}	4.1×10^{-6}	13	5.0×10^{6}
n-InSb	CO$_2$	0.116	0.5	3.0×10^{-7}	2.2×10^{-5}	1.3	4.1×10^{4}

Table 4.1   All Values are computed at $T = 5\,^\circ K$, $N = 3 \times 10^{16}$ cm^{-3}.

* In Calculating γ , when two different values are available, the larger value is chosen to provide a margin.
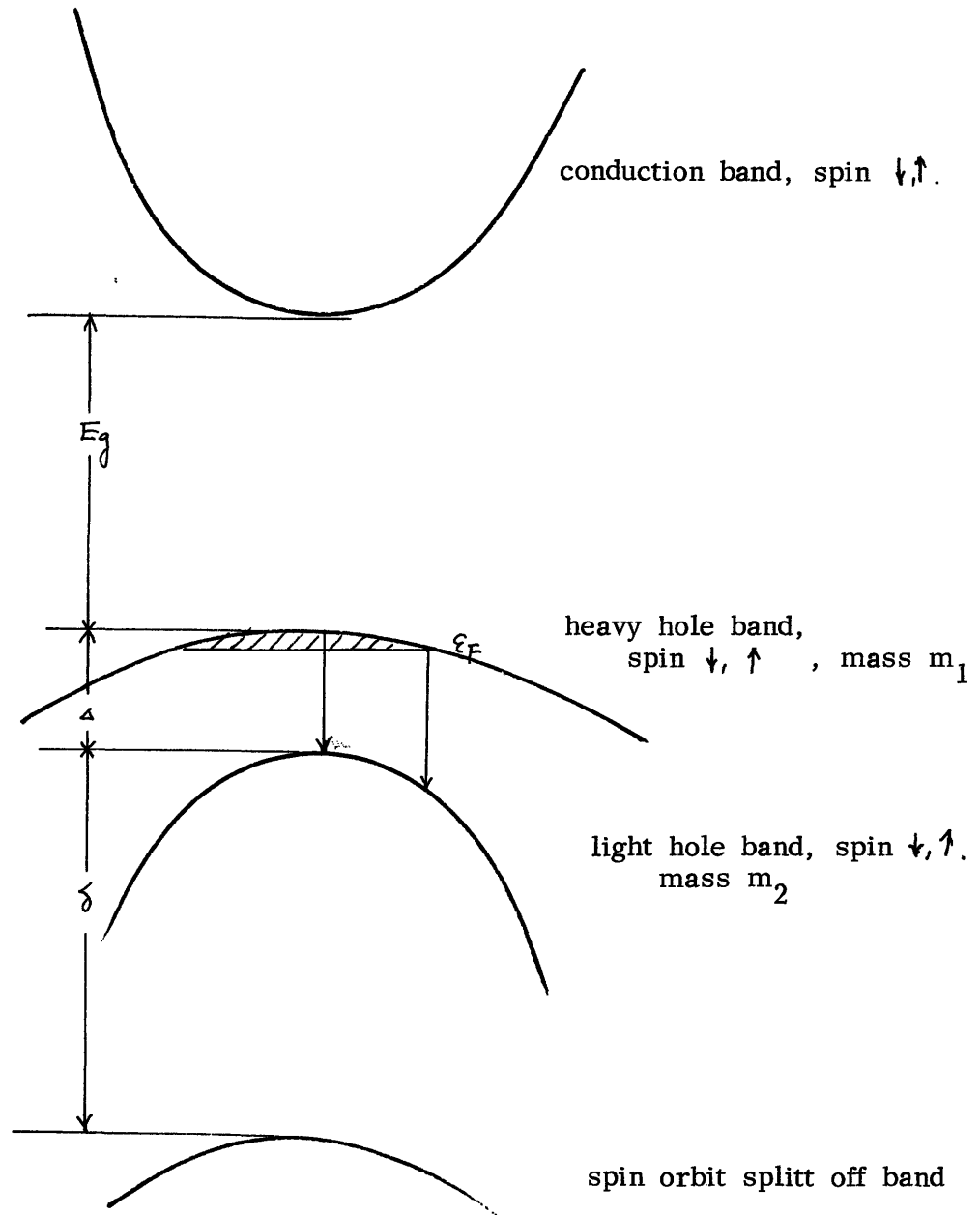
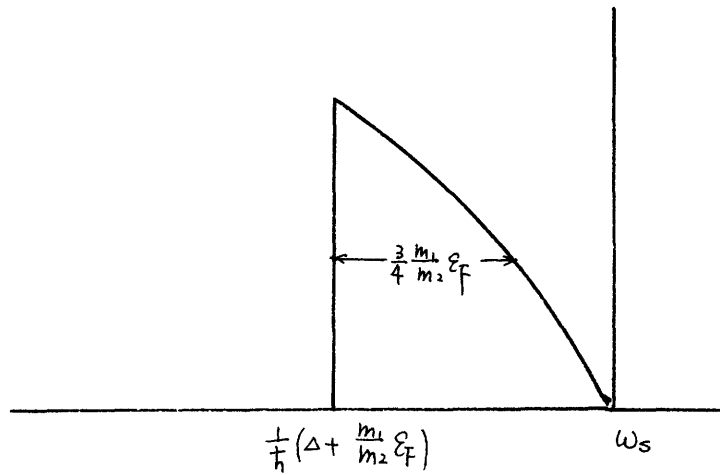Figure 4.1   Energy bands under an external uniaxial stress.
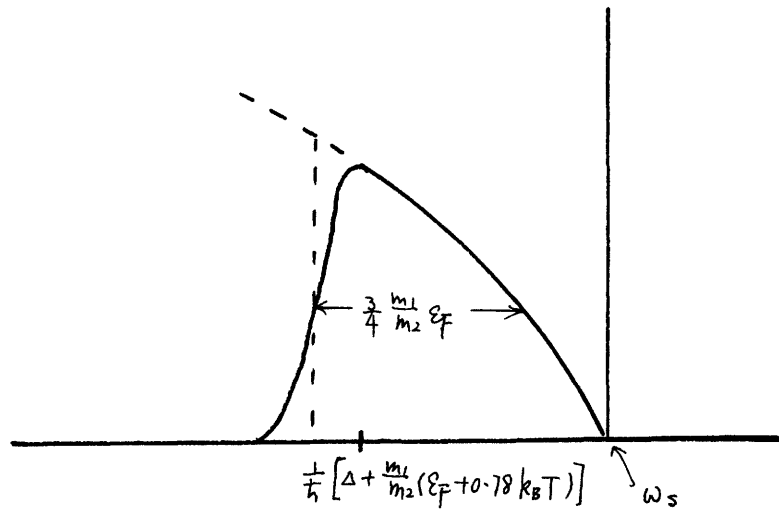
Figure 4.2a.   Spontaneous lineshape at T = 0.

Figure 4.2b.   Spontaneous lineshape at low temperatures.

REFERENCES

(1)   C.K.N. Patel and E.D. Shaw, Phys. Rev. Lett. 24, 451 (1970); Phys. Rev. B3, 1279 (1971)

(2)   C.K.N. Patel, E.D. Shaw and R.J. Kerl, Phys. Rev. Lett. 25, 8 (1970); C.K.N. Patel and Kreutzner, Appl. Phys. Lett. (to be published)

(3)   A. Mooradian, S.R.J. Breuck and F.A. Blum, Appl. Phys. Lett. 17, 481 (1970)

R.L. Allwood, etc., J. Phys. C3, 1186 (1970)

E.D. Shaw and C.K.N. Patel, Appl. Phys. Lett. 18, 215 (1971)

S.R.J. Breuck and A. Mooradian, Appl. Phys. Lett. 18, 229 (1971)

C.K.N. Patel, Appl. Phys. Lett. 18, 274 (1971)

R.L. Aggarwal, etc., Appl. Phys. Lett 18, 383 (1971)

(4)   J.M. Luttinger, Phys. Rev. 102, 1030 (1956)

(5)   G. Dresselhaus, Kip and C. Kittel, Phys. Rev. 98, 368 (1955)

(6)   W.H. Kleiner and L.M. Roth, Phys. Rev. Lett. 2, 334 (1959)

(7)   J.C. Hensel and G. Feher, Phys. Rev. 129, 1041 (1963)

(8)   H. Hasegawa, Phys. Rev. 129, 1029 (1963)

(9)   Y. Yafet, Phys. Rev. 152, 858 (1966)

(10)   E.O. Kane, J. Phys. Chem. Solids 1, 92 (1957)

(11)   R. Newman and W.W. Tyler, Phys. Rev. 105, 885 (1957)

(12)   G.W. Gobeli and H.Y. Fan, Phys. Rev. 119, 613 (1960)

S.W. Kurnick and J.M. Powell, Phys. Rev. 116, 597 (1959)

(13)   R. Braunstein, Phys. Chem. Solids 8, 280 (1959)

(14)   F. Matossi and F. Stern, Phys. Rev. 111, 472 (1958)

(15) Y.R. Shen and N. Bloembergen, Phys. Rev. <u>137</u>, A1787 (1965)

      N. Bloembergen, Amer. J. Phys. <u>35</u>, 989 (1967)

(16) F.A. Johnson, S.J. Fray and R.H. Jones, in <u>Proc. Int. Conf. on</u>

      <u>Semiconductor Physics</u>, Prague: Publishing House of the Czechoslovakia

      Academy of Science, 1961

(17) A.J. Beaulieu, Appl. Phys. Lett. <u>26</u>, 1634 (1971)

(18) N. Tzoar and J. Gernsten, Phys. Rev. Lett. <u>26</u>, 1634 (1971)

(19) S.A. Akhamanov, etc., Sov. Phys. Usp. <u>10</u>, 609 (1968)

(20) B.V. Rollin and A.D. Petfor, J. of Elec., <u>1</u>, 171 (1955)

(21) W. Lamb, in <u>Quantum Optics and Electronics</u>, 1964 Les Houches

      Lectures, ed. by DeWitt, etc., Gordon and Breach, New York, 1965.

      M. Lax, in <u>Physics of Quantum Electronics</u>, ed. by Kelley, etc.,

      McGraw-Hill, New York, 1966

CONCLUSIONS

We have developed in this thesis a comprehensive theory of light scattering from electronic levels, with specific applications to spin-flip scattering in indium antimonide. In the following we will review our major accomplishments and suggest further revenues of fruitful research.

I. CRITIQUE

We have first investigated the theory of spontaneous lineshape for spin-flip Raman scattering. Besides its application to our later theory of stimulated scattering, our first principle description of spin-flip scattering is of independent interest. We have found two important contributions to the lineshape, from electron nonparabolicity and diffusion. Each of these two mechanisms is dominant in a different geometry. Analytic formulas are provided for the lineshapes and linewidths. Our linewidth results as well as the diffusion broadened lineshape are in very good agreement with experiment.

The nonparabolicity broadened lineshape is, however, not in such good agreement with experiments. This may due partly to possible experimental errors, because there are certain features of the experimental results which appear inconsistent. It is also possible that we have neglected some important effects in our approximation. Further theoretical investigation along our line

of approach should be promising and additional careful measurements needed to clarify this issue.

In Chapter 2 we have constructed a general theory of an electronic Raman laser including anti-Stokes and pump radiations. The steady state laser behavior is treated in detail. Closed-form analytical results are obtained and interpreted. We have solved the problem of finding scattering outputs in terms of only the system parameters and the boundary condition pump excitation. Interesting qualitative results include the constancy of Stokes-anti-Stokes power ratio as a function of input, and the saturation behavior with proper pump depletion. This theory is sufficiently general to be applicable to many other Raman systems.

In Chapter 3 we made a detailed analysis of the temperature, carrier concentration, and magnetic field effects on spin-flip scattering. The scattering theories of Chapters 1 and 2 are then applied together with this treatment for the n-type indium antimonide spin-flip Raman laser. Our analytic results are compared to various experimental data with very good agreement in general. Since the other optical nonlinearities are not important in the spin-flip laser, our comparison probably constitutes the first detailed confirmation between Raman laser theory and experiments. Because of the vast amount of data available, we have not attempted a comprehensive comparison. Our results can however be readily applied to correlate, organize, and explain all the available data.

In Chapter 4 we analyzed the possible operation of a stress-tuned p-type indium antimonide inter-valence band laser using the approach we have developed. It appears promising that a new, easily tunable high power laser in the wavelength range 10μ - 35μ can be obtained with this mechanism. Further theoretical and new experimental work are certainly worthwhile.

We have therefore demonstrated the usefulness of our electronic Raman scattering theories not only in detailed analysis of experimental observations on the important spin-flip n-type laser, but also in general exploitation of useful stimulated electronic scattering mechanisms. In addition, our theory can establish the possible environment and conditions under which the laser can operate.

II. SUGGESTIONS FOR FUTURE WORK

A number of interesting theoretical work are opened through our investigations. Refinement of our approximation or inclusion of additional mechanism can be carried out along our direction of approach in the nonparabolicity dominated lineshape calculation. Much further work should be pursued based on our model of an electronic Raman laser to include effects of inhomogeneous broadening, backward Raman waves, multimode structure, as well as higher order Stokes and anti-Stokes radiations. One can also consider the stability of the steady state, the transient behavior, and the quantum statistics of the scattering outputs. Other new mechanism of stimulated scattering should be exploited with the aid of our theory.

Many interesting experimental problems are also suggested by our work. Careful measurements of spontaneous and stimulated lineshapes should be made to provide further understanding of the broadening mechanisms and additional comparison with our theory. While our laser theory already appears to provide an accurate description of the spin-flip laser, various further experiments with different configurations should be carried out to provide a detailed confirmation with our theory and understanding. The new mechanism we propose for generating tunable coherent radiation by stress convers a very wide frequency range and looks promising. Experimental efforts should be worthwhile to be undertook immediately.

Finally, we note that a very fruitful interplay of our theory with experiments would be the indication of the limiting operating conditions of stimulated scattering. Applications will be greatly facilitated if practical operations of the laser can be realized without severe environmental restrictions.

BIOGRAPHICAL NOTE

Y. C. S. Auyang was born in Shianghai, China on February 8, 1948. She came to the United States in 1965 and received her B.S. degree in Physics from the University of California at Los Angeles in June, 1967. She continued her studies at M. I. T. where she has been a research assistant for the past four years.